

Measurements and Analysis of the Internal Tide in the Monterey Bay Region

Samantha Rachel Terker

A dissertation

submitted in partial fulfillment of the

requirements for the degree of

Doctor of Philosophy

University of Washington

2012

Reading Committee:

James Girton, Chair

Eric Kunze

Matthew Alford

Program Authorized to Offer Degree:

Oceanography

University of Washington

Abstract

Measurements and Analysis of the Internal Tide in the Monterey Bay Region

Samantha Rachel Terker

Chair of the Supervisory Committee:
Affiliate Assistant Professor James Girton
Physical Oceanography

The Monterey Bay region, with bathymetric features including Monterey Submarine Canyon and Sur Platform, has been a site for examination of generation, propagation and dissipation of the internal tide. Observations of propagation of the internal tide on the California continental margin and in Monterey Submarine Canyon are presented. Additionally, the development and sea-trials of the EM-POGO, a free-falling absolute velocity profiler which can be used to study the internal tide is detailed.

EM-POGO: The EM-POGO is a low-cost and accurate velocity profiler. Electromagnetic current instrumentation has been added to Bathymetry Systems, Inc. POGO transport sondes to produce the EM-POGO. Velocity determined from measurements of motionally-induced electric fields generated by ocean currents moving through the vertical component of the Earth's magnetic field are added to the transport provided by the POGO. A refurbished EM-POGO collected 15 profiles; relative and absolute velocity uncertainty was $\sim 1 \text{ cm s}^{-1}$ and $0.5 - 5 \text{ cm s}^{-1}$, respectively, with 25-m vertical resolution.

Internal tide: North of Sur Platform but south of Monterey Submarine Canyon, a short-duration survey and a multi-week timeseries measured northward energy flux in the mean, supporting model results indicating that topographic features off Point Sur generate strong internal tides observed in the canyon. Though dom-

inated by low modes with $O(100 \text{ km})$ horizontal wavelengths, semidiurnal energy fluxes, kinetic and potential energies show lateral variability on $O(5 \text{ km})$ scales. Spatial variability results, in part, from interference patterns and the sharp delineation of beams with limited azimuthal extent. A simple two-source model of a first-mode interference pattern reproduces the most striking aspects of the observations.

In Monterey Submarine Canyon energy fluxes are steered by canyon bathymetry and are consistent with a numerical model. Vertical profiles reveal predominantly along-canyon flux intensified in the bottom 500 m. A rough one-dimensional along-canyon energy budget based on energy-flux divergence, dissipation rates and barotropic-to-baroclinic energy conversion rates is constructed. Cross-canyon-integrated along-canyon flux decreases from $13 \pm 3.4 \text{ MW}$ at the deepest section (1500 m) to $5.6 \pm 0.3 \text{ MW}$ at the shallowest (900 m). The largest drops ($\sim 7 \text{ MW}$ and $\sim 4 \text{ MW}$) are around meanders. The one-dimensional flux budget is, on average, balanced.

Table of Contents

List of Figures	iii
1 Introduction	1
1.1 The Study of the Internal Tide	2
1.1.1 Motivation: the global energy budget for mixing	2
1.1.2 Observation technology	4
1.1.3 Analysis and interpretation	6
1.1.4 Significant regional experiments	6
1.1.5 Monterey Bay	7
1.2 Internal wave review	8
1.3 Organization of Thesis	10
Bibliography	12
2 The EM-POGO: A Simple, Absolute Velocity Profiler	19
Abstract	20
2.1 Introduction	21
2.2 Materials and methods	22
2.3 Theory and calculations	29
2.4 Results	34
2.4.1 Grand Bahama Island sea trial: 1999	34
2.4.2 Monterey Bay region sea trial: 2006	35
2.5 Conclusions	39
2.6 Acknowledgments	40
2.7 Bibliography	41
3 Observations of the Internal Tide on the California Continental Margin near Monterey Bay	44
Abstract	46
3.1 Introduction	47
3.2 Methods	50
3.2.1 Field measurements	50

3.2.2	Energy flux and energy calculations	53
3.2.3	Energy flux uncertainty part 1: overview	54
3.2.4	The subsampling method	57
3.3	Results	59
3.3.1	Barotropic tide	59
3.3.2	Internal wave field	59
3.3.3	Semidiurnal energy flux - depth integrals	60
3.3.4	Semidiurnal energy flux - profiles	61
3.3.5	Horizontal kinetic and available potential energy profiles	63
3.3.6	Data/model comparisons and temporal variability	65
3.4	Discussion	67
3.5	Conclusions	70
3.6	Acknowledgments	73
3.7	Bibliography	74
4	Observations of the Internal Tide in Monterey Submarine Canyon	88
	Abstract	89
4.1	Introduction	89
4.2	Data and methods	94
4.2.1	Data	94
4.2.2	Methods: energy-flux calculations and budget	96
4.3	Results	104
4.3.1	Model-observation comparison	104
4.3.2	Energy flux profiles	107
4.3.3	Energy budget	108
4.4	Summary	111
4.5	Acknowledgments	113
4.6	Bibliography	114

List of Figures

2.1	Photograph of the EM-POGO	24
2.2	Schematic of an EM-POGO profile	25
2.3	Raw compass coil and electrode voltages from drop 107	26
2.4	Block diagram of EM-POGO electrical components	28
2.5	EM-POGO deployment locations	35
2.6	1999 EM-POGO sea trial velocity profiles	36
2.7	2006 EM-POGO sea trial velocity profiles	37
2.8	ADCP - EM-POGO velocity profile comparison	39
3.1	Overview of experiment site and station locations	78
3.2	Depth-integrated semidiurnal energy fluxes	79
3.3	Meridional and zonal transects of vertical and horizontal semidiurnal energy flux	80
3.4	Barotropic velocities and depth-integrated fluxes	82
3.5	Error analysis methods	83
3.6	Amplitude and phase of north/south semidiurnal velocity and pressure	85
3.7	Horizontal kinetic and available potential energy	86
3.8	Simple model of two- and three-source interference patterns	87
4.1	Station locations	96
4.2	Full-water-column timeseries of \mathbf{u}' and P'	98
4.3	Cross-canyon section: along- and cross-canyon profiles of energy flux	99
4.4	Along-thalweg energy-flux profiles	100
4.5	Scatterplot comparing observed and modeled energy flux	101
4.6	Cross-canyon structures of depth-integrated energy flux	105
4.7	Map of energy flux vectors	106
4.8	One-dimensional along-canyon energy budget	111

Acknowledgments

I would like to express sincere appreciation to my advisor, James Girton, for sharing his knowledge and for his patience during the graduate school process. It was a pleasure and an honor to work with him. I would also like to thank Tom Sanford for his support, encouragement, and advice. I want to thank Eric Kunze, who consistently provided invaluable scientific input and detailed and thorough feedback during the writing process. Matthew Alford, was critical in the final push towards graduating. Overall, I feel lucky to have had the opportunity to work with my entire committee as I greatly respect each of them as scientists and as people.

Of course, I would also like to acknowledge my family, particularly my husband Andy Terker, and my parents Rhonel and Mark Brody, for providing moral support throughout this long process. Last but not least, I would like to thank my fellow physical oceanography graduate students Ana Cecilia Peralta Ferriz and Sally Warner who have become two of my closest friends.

Chapter 1

Introduction

1.1 The Study of the Internal Tide

1.1.1 Motivation: the global energy budget for mixing

The semidiurnal internal (baroclinic) tide provides a route for approximately 25 - 30 % of the 1.2 TW of M_2 surface (barotropic) tidal power (*Munk and Wunsch, 1998; Wunsch, 2002*); the rest (70 - 75%) is dissipated in shallow waters by bottom friction (*Taylor, 1920; Jeffreys, 1920; Egbert and Ray, 2001*). Dissipation of the internal tide is of great interest as mixing hotspots are required to maintain an advective-diffusive balance consistent with the observed abyssal stratification (*Munk and Wunsch, 1998; Wunsch, 2002*). Furthermore, understanding where and how energy is dissipated is important for improving the predictive capabilities of ocean and climate models which are sensitive to mixing, but unable to resolve such small scales. Not only is mixing small-scale, but it is localized and intermittent and therefore difficult to measure.

Internal tide mixing is associated with four processes (*Klymak et al., 2008*): (i) direct bottom friction, (ii) internal tide dissipation through non-linear interactions with the ambient wavefield, (iii) internal tide breaking on topography after propagation and (iv) non-linear internal tide instability and breaking in generating regions. The percentage of energy that gets dissipated by each of the four processes listed above also depends on the generation site and the local internal wavefield. In the Monterey Bay region, *Kang and Fringer (2011)* find dissipation due to (i) to be 12% and (iv) to be 50%. In order to quantify mixing from breaking internal tides (iii), the processes of internal tide generation and propagation must be studied.

Generation of the baroclinic tide occurs in the deep ocean near topographic

features (*Egbert and Ray, 2003; Simmons et al., 2004*). Propagation of the internal tide transfers energy, sometimes thousands of kilometers, from source to sink (*Dushaw et al., 1995; Zhao et al., 2010*), and from large scales (barotropic tide) to intermediate scales (baroclinic tide) and eventually to small scales (dissipation) (*Alford, 2003; Garrett, 2003; St. Laurent and Garrett, 2003; Rudnick et al., 2003; Simmons et al., 2004; Klymak et al., 2008; Alford et al., 2011*). The energy that propagates far is generally low-mode; the baroclinic tide can be described by the superposition of a number of vertically-standing and horizontally-propagating modes which depend on the depth-dependent buoyancy frequency, $N(z)$. Mode structures are determined by solving a Sturm-Liouville eigenvalue problem for vertical displacement and with boundary conditions of no vertical displacement at the surface or at the bottom (*Vlasenko et al., 2005*). Tracing internal tidal energy from source to sink must account for interactions with mesoscale features and interference patterns formed from the interaction of internal tides generated a number of sources, and interaction with bathymetry [*Rainville et al. (2010); Zhao and D'Asaro (2011)*, Chapters 3 and 4].

Generation, or barotropic-to-baroclinic conversion, at a particular topographic feature depends on a number of parameters such as the strength of the barotropic tide, the slope of the bathymetry, the ratio of the bathymetry slope to the ray-slope of the wave (α/s), and the amplitude of the bathymetry compared to the vertical scale of the wave, the stratification, and other conditions (*Cox and Sandstrom, 1962; Maas, 2011; Llewellyn Smith, 2011; Kelly et al., 2012; Wang et al., 2012*). Conversion estimates have been formulated from theoretical (*Bell Jr., 1975; Baines, 1982; Nycander, 2005; Garrett and Kunze, 2007*) and numerical (*Carter et al., 2008; Kang and Fringer, 2011*) standpoints. Extensive literature can be

found examining conversion for a number of idealized bathymetric features (continental slopes, mid-ocean ridges, bank-edges, knife-edges) and using a number of conditions (e.g. linear governing equations, inviscid, weak topography approximation meaning that the amplitude of bathymetry \ll vertical scale of the waves, hydrostatic since $\omega_{M_2}/N \ll 1$). It is clear that conversion is a complicated process that is sensitive to the topographic scale (*Di Lorenzo et al.*, 2006; *Zilberman et al.*, 2009) and the ability to calculate the baroclinic perturbation pressure at the bottom (*Kelly et al.*, 2010). Conversion in Chapter 4 is defined as the rate of pressure work done by the barotropic tide on the baroclinic as described in *Zilberman et al.* (2011) and *Kelly et al.* (2012) and can be of either sign. I

In addition to the contribution to the global energy budget, internal tides are also important for local tidal forecasting as internal tides can alter pressure gradients and depth-averaged currents (*Petruncio et al.*, 1997; *Rosenfeld et al.*, 2009; *Carter*, 2010). Biological processes are also affected by internal tides as tidal mixing on continental shelves supplies nutrients to the photic zone (*Shea and Broenkow*, 1982; *Sharples et al.*, 2009). In addition to forecasting and biological process, sediment transport is also impacted by internal tides via sediment resuspension and interpretation of sedimentary records (*Puig et al.*, 2004; *Pomar et al.*, 2012).

1.1.2 Observation technology

The presence of internal tides in the ocean have been acknowledged for over a century (*Pettersson*, 1908) though methodical studies of the internal tide were not possible until the advent of the Nansen bottle and reversing thermometer (*Wunsch*,

1975). The basic theory for internal tide generation was developed in the 1970s and 1980s (*Cox and Sandstrom, 1962; Bell Jr., 1975; Baines, 1982*) and the topic received renewed interest (*Garrett and Kunze, 2007*) when it became clear that the dissipation associated with the internal tide (still much less than dissipation associated with wind-driven mixing and direct tidal dissipation) was essential for understanding ocean mixing. As technology has improved, so has our ability to observe the internal tides.

Collecting observations to measure the energy of the internal tide and the subsequent analysis, though constantly improving, can be complicated. In order to calculate energy flux, a fundamental quantity for internal wave energetics (*Nash et al., 2005*), measurements must provide full water-column profiles of velocity and density (or temperature as long as the temperature-salinity relationship is tight and known). There are a number of instruments well suited for this including expendable Current Profilers (XCPs), a Lowered Acoustic Doppler Current Profiler (LADCP), the EM-POGO, moored profilers and other moorings (as long as they cover enough of the water-column), and tow-yoed instruments (such as SWIMS). Satellite altimetry, though providing only surface information, is useful for identifying barotropic-to-baroclinic conversion sites and also for studying the long-range propagation of the low-mode (known vertical structure) internal tide. Of course, each method has advantages and disadvantages associated with spatial and vertical resolution, cost and ease of deployment and recovery. The refurbishment and sea-trials of the EM-POGO, a low-cost, easy to deploy and recover, full water-column profiling, relative velocity (or shear) profiler, is the focus of Chapter 2. Data from XCPs and an LADCP are used in analysis presented in Chapters 3 and 4, though these chapters emphasize characterizing the internal tide, rather

than instrumentation.

1.1.3 Analysis and interpretation

Analysis can be complex mainly because, as is usually the case for oceanographic measurements, temporal and spatial resolution is limited. These limitations can complicate (i) separating the tidal components of the velocity and pressure, especially in regions with small signal-to-noise ratios (Chapter 3 deals with this) and where there are higher frequency waves which can alias measurements and lower frequency (e.g. diurnal or inertial motions) which can bias measurements, and (ii) interpretation of point measurements where multiple internal tide sources create interference patterns (*Martini et al. 2007; Rainville et al. 2010*, Chapter 3). Additionally, the calculation of energy flux involves the separation of barotropic and baroclinic components which can be non-trivial (*Kelly et al., 2010*) and this can impact barotropic-to-baroclinic conversion estimates which rely on baroclinic pressure at the bottom. Conversion estimates are also highly sensitive to the bathymetry scale which is used for describing the bottom slope, so this must be done cautiously (*Zilberman et al., 2009; Di Lorenzo et al., 2006*).

1.1.4 Significant regional experiments

Comprehensive experiments at a specific location involving extensive observations and numerical models are a useful way to study internal tide generation, propagation and dissipation. Studies such as the Hawaiian Ocean Mixing Experiment (HOME) (*Rudnick et al. (2003); Alford et al. (2006); Lee et al. (2006); Klymak et al. (2006); Nash et al. (2006); Rainville and Pinkel (2006); Klymak et al. (2008)*), just

to name a few), AESOP (Assessing the effects of Submesoscale Ocean Parameterizations) which was part of the Monterey Bay 2006 Experiments and includes the experiment in Chapter 3 (*Hall and Carter, 2011; Johnston et al., 2011; Terker et al., 2012*), and the Internal Waves in Straits Experiment (IWISE) (*Alford et al., 2010, 2011; Klymak et al., 2011; Simmons et al., 2011*), combine observation and modeling efforts and have provided much insight into these processes. Coordination between modeling and observational efforts is essential for being able to map the flow of tidal energy and to identify where the mixing occurs.

1.1.5 Monterey Bay

Monterey Bay was chosen as the site of one of these comprehensive experiments as the region has (i) a number topographic features which generate internal tides, (ii) numerous submarine canyons which focus and dissipate the internal tide, (iii) previous observational and modeling studies (*Petruncio et al., 1997; Rosenfeld et al., 2009; Kunze et al., 2002; Jachec et al., 2006*), (iv) the largest (4,024 square nautical mile) United States marine sanctuary which protects and studies the rich diversity of marine life and important biological processes and (v) is located in a tectonically active geological system. In the summer of 2006 alone, the AESOP experiment was just one of four large field experiments that took place in the region (<http://www.mbari.org/mb2006>).

The internal tides are a dominant process in the area, especially in Monterey Submarine Canyon. Submarine canyons have been identified as sites of large baroclinic tidal velocities and energy fluxes (*Shepard et al., 1974; Petruncio et al., 1997; Jachec et al., 2006; Kang and Fringer, 2011*) and enhanced tidal dissipation

(*Carter and Gregg, 2002; Kunze et al., 2002*) especially where the slope is near-critical (*Gayen and Sutanu, 2010*). In addition to Monterey Submarine Canyon, there are numerous generation sites in the region, which enable the study of generation, propagation and dissipation, all of which are included in Chapters 3 and 4.

1.2 Internal wave review

This section provides a brief review of internal gravity waves since internal tides are internal gravity waves generated by density perturbations in a stratified flow. The principal lunar semidiurnal component, M_2 ($T_{M_2} = 12.421$ hours, $\omega_{M_2} = 1.4064 \times 10^{-4} \text{ rad s}^{-1}$), is the dominant tidal constituent in most places, including the Monterey Bay region. A major difference between surface waves and internal waves is that the restoring force is buoyancy which depends on reduced gravity ($g' = g \frac{\delta\rho}{\rho_0}$) which depends on density (ρ) differences between adjacent layers, rather than the full gravitation force. This results in internal waves having lower frequencies and larger amplitudes than surface waves. Buoyancy frequency, N , ($N^2 = \frac{-g}{\rho_0} \frac{\partial\rho}{\partial z}$) provides a means of quantifying the strength of density stratification. In general, only internal gravity waves with frequencies ω between the Coriolis frequency, f , and N , can propagate freely in the ocean, so $f \ll \omega \ll N$. The Coriolis frequency varies with latitude (ψ), and depends on the earth rotation rate ($\Omega = 7.2921 \times 10^{-5} \text{ s}^{-1}$) as $f = 2\Omega \sin(\psi)$.

Internal gravity waves are described by the linearized, hydrostatic, incompressible, Boussinesq governing equations. These governing equations include the conservation of momentum (1.1, 1.2, 1.3), the conservation of mass (1.4), and the

continuity equation (1.5) [Gill 1982]:

$$\frac{\partial u'}{\partial t} - f v' = -\frac{1}{\rho_0} \frac{\partial P'}{\partial x} \quad (1.1)$$

$$\frac{\partial v'}{\partial t} + f u' = -\frac{1}{\rho_0} \frac{\partial P'}{\partial y} \quad (1.2)$$

$$\frac{\partial w'}{\partial t} = -\frac{1}{\rho_0} \frac{\partial P'}{\partial z} - \frac{\rho'}{\rho_0} g \quad (1.3)$$

$$\frac{\partial u'}{\partial x} + \frac{\partial v'}{\partial y} + \frac{\partial w'}{\partial z} = 0 \quad (1.4)$$

$$\frac{\partial \rho'}{\partial t} = -w' \frac{d\rho_{bkgd}}{dz}. \quad (1.5)$$

The apostrophe " ' " denotes a perturbation from the depth average (baroclinic) and $d\rho_{bkgd}$ is the mean background density. The equations include variables for horizontal velocity (u, v), vertical velocity (w), pressure (P) and density (ρ , ρ_0 = mean background density and is not a function of depth). These equations can be manipulated and condensed into a single equation in terms of the vertical velocity perturbation w'

$$\frac{\partial}{\partial t^2} \left(\frac{\partial^2 w'}{\partial x^2} + \frac{\partial^2 w'}{\partial y^2} + \frac{\partial^2 w'}{\partial z^2} \right) + f^2 \frac{\partial^2 w'}{\partial z^2} + N^2 \left(\frac{\partial^2 w'}{\partial x^2} + \frac{\partial^2 w'}{\partial y^2} \right) = 0 \quad (1.6)$$

(Gill, 1982; Kundu and Cohen, 2004; Gerkema and Zimmerman, 2008). Vertical velocity w (different from frequency ω) describing a traveling plane wave of the form

$$w = w_0 e^{i(kx+ly+mz-\omega t)} \quad (1.7)$$

with wavenumber vector $\mathbf{k} = (k, l, m)$ or (κ, m) where $\kappa^2 = k^2 + l^2$ can be substituted into (1.6) to yield the dispersion relation which shows that for internal

waves, frequency depends only on the angle that the wave vector makes with the horizontal (φ) and not the magnitude of the wavenumber

$$\omega^2 = \frac{\kappa^2 N^2 + m^2 f^2}{m^2 + \kappa^2} = f^2 \sin^2 \varphi + N^2 \cos^2 \varphi. \quad (1.8)$$

Group velocity defines the direction and speed of energy propagation is $C_g = \left(\frac{\partial \omega}{\partial k}, \frac{\partial \omega}{\partial l}, \frac{\partial \omega}{\partial m} \right)$ and, for internal waves, is perpendicular to phase velocity, which defines how fast crests and troughs travel, $C_p = \left(\frac{\omega}{\sqrt{k^2 + l^2 + m^2}} \hat{\mathbf{k}} \right)$. Upward (downward) group velocity corresponds to downward (upward) phase velocity. The aspect ratio, $\alpha = \frac{\kappa}{m} = \sqrt{\frac{\omega^2 - f^2}{N^2 - \omega^2}}$ determines whether the bathymetry that the internal wave comes into contact with is sub-critical (bathymetric slope, $s < \alpha$), near-critical or super-critical ($s > \alpha$) for that particular frequency.

1.3 Organization of Thesis

The rest of the thesis is structured as follows: Chapter 2 is a manuscript currently under review at *Deep-Sea Research II*, "The EM-POGO: A Simple, Absolute Velocity Profiler". The development and sea-trials of the EM-POGO, and electromagnetic current meter are documented. Chapter 3, "Observations of the Internal Tide on the California Continental Margin near Monterey Bay", is a manuscript currently under review at *Continental Shelf Research*. This chapter describes and examines small-scale variability observed in a northward beam of tidal energy as well as discussing some nuances of experiment design with respect to isolating the internal tide in an area with a weak signal-to-noise ratio. Chapter 4, "Observations of the Internal Tide in the Monterey Bay Submarine Canyon",

is a presentation of the observation and analysis from a 2008 experiment. This chapter focuses on the energy flux as it travels along the canyon and attempts to close the one-dimensional along-canyon flux budget. Each chapter is formatted as a self-contained paper with its own abstract, introduction, methods, results, conclusions, references and acknowledgements sections.

Bibliography

Alford, M. (2003), Redistribution of energy available for ocean mixing by long-range propagation of internal waves, *Nature*, pp. 159–62.

Alford, M., M. Gregg, and M. Merrifield (2006), Structure, propagation, and mixing of energetic baroclinic tides in Mamala Bay, Oahu, Hawaii, *J. Phys. Oceanogr.*, pp. 997–1018.

Alford, M., R. Lien, H. Simmons, J. Klymak, Y. Yang, D. Tang, and M. Chang (2010), Speed and evolution of nonlinear internal waves transiting the South China Sea, *J. Phys. Oceanogr.*, pp. 1338–55.

Alford, M., et al. (2011), Energy flux and dissipation in Luzon Strait: Two tales of two ridges, *J. Phys. Oceanogr.*, pp. 2211–22.

Baines, P. (1982), On internal tide generation models, *Deep Sea Res.*, pp. 307–38.

Bell Jr., T. (1975), Topographically generated internal waves in the open ocean, *J. Geophys. Res.*, pp. 330–27.

Carter, G. (2010), Barotropic and baroclinic M_2 tides in the Monterey Bay region, *J. Phys. Oceanogr.*, pp. 1766–83.

- Carter, G., and M. Gregg (2002), Intense, variable mixing near the head of Monterey Submarine Canyon, *J. Phys. Oceanogr.*, pp. 3145–65.
- Carter, G., M. Merrifield, J. Becker, K. Katsumata, M. Gregg, D. Luther, M. Levine, T. Boyd, and Y. Firing (2008), Energetics of M_2 barotropic-to-baroclinic tidal conversion at the Hawaiian Islands, *J. Phys. Oceanogr.*, pp. 2205–23.
- Cox, C., and H. Sandstrom (1962), Coupling of internal and surface waves in water of variable depth , *J. Oceanogr. Soc. Jpn., 20 Anniv.*, 499–513.
- Di Lorenzo, E., W. Young, and S. Llewellyn Smith (2006), Numerical and analytical estimates of M_2 tidal conversion at steep oceanic ridges, *J. Phys. Oceanogr.*, pp. 1072–84.
- Dushaw, S., B. Cornuelle, P. Worcester, B. Howe, and D. Luther (1995), Barotropic and baroclinic tides in the Central North Pacific Ocean determined from long-range reciprocal acoustic transmissions, *J. Phys. Oceanogr.*, pp. 631–47.
- Egbert, G., and R. Ray (2001), Estimates of M_2 tidal energy dissipation from TOPEX/Poseidon altimeter data, *J. Geophys. Res.*, pp. 22,475–502.
- Egbert, G., and R. Ray (2003), Semi-diurnal and diurnal tidal dissipation from TOPEX/Poseidon altimetry, *Geophys. Res. Lett.*, p. (17) 1907.
- Garrett, C. (2003), Internal tides and ocean mixing, *Science*, pp. 1858–59.
- Garrett, C., and E. Kunze (2007), Internal tide generation in the deep ocean, *Annual Review of Fluid Mechanics*, pp. 57–87.

- Gayen, B., and S. Sutanu (2010), Turbulence during the generation of internal tide on a critical slope, *Physical Review Letters*, p. (104) 218502.
- Gerkema, T., and J. Zimmerman (2008), An introduction to internal waves, lecture notes, Royal NIOZ, Texel.
- Gill, A. (1982), *Atmosphere-Ocean Dynamics*, pp. 256–267, Academic Press.
- Hall, R., and G. Carter (2011), Internal tides in Monterey Submarine Canyon, *J. Phys. Oceanogr.*, pp. 186–204.
- Jachec, S., O. Fringer, M. Gerritsen, and R. Street (2006), Numerical simulation of internal tides and the resulting energetics within Monterey Bay and the surrounding area, *Geophys. Res. Lett.*, p. (33) L12605.
- Jeffreys, H. (1920), Tidal friction in shallow seas, *Philos. Trans. R. Soc. London, Ser. A*, pp. 239–64.
- Johnston, T., D. Rudnick, G. Carter, R. Todd, and S. Cole (2011), Internal tide beams and mixing near Monterey Bay, *J. Geophys. Res.*, p. C03017.
- Kang, D., and O. Fringer (2011), Energetics of barotropic and baroclinic tides in the Monterey Area, *J. Phys. Oceanogr.*, p. in press.
- Kelly, S., J. Nash, and E. Kunze (2010), Internal-tide energy over topography, *J. Geophys. Res.*, p. C06014.
- Kelly, S., J. Nash, K. Martini, M. Alford, and E. Kunze (2012), The cascade of tidal energy from low to high modes on a continental slope, *Unpublished Manuscript*, pp. –.

- Klymak, J., J. Moum, J. Nash, E. Kunze, J. Girton, G. Carter, C. Lee, T. Sanford, and M. Gregg (2006), An estimate of tidal energy lost to turbulence at the Hawaiian Ridge, *J. Phys. Oceanogr.*, pp. 1148–64.
- Klymak, J., R. Pinkel, and L. Rainville (2008), Direct breaking of the internal tide near topography: Kaena Ridge, Hawaii, *J. Phys. Oceanogr.*, pp. 380–99.
- Klymak, J., M. Alford, R. Pinkel, R. Lien, and Y. Yang (2011), The breaking and scattering of the internal tide on a continental slope, *J. Phys. Oceanogr.*, pp. 926–45.
- Kundu, P., and I. Cohen (2004), *Fluid Mechanics*, pp. 248–256, 3 ed., Elsevier Academic Press.
- Kunze, E., L. Rosenfeld, G. Carter, and M. Gregg (2002), Internal waves in Monterey Submarine Canyon, *J. Phys. Oceanogr.*, pp. 1890–1913.
- Lee, C., E. Kunze, T. Sanford, J. Nash, M. Merrifield, and P. Holloway (2006), Internal tides and turbulence along the 3000-m isobath of the Hawaiian ridge, *J. Phys. Oceanogr.*, pp. 1166–81.
- Llewellyn Smith, S. (2011), A conundrum in conversion, *J. Fluid Mech.*, pp. 1–4.
- Maas, L. (2011), Topographies lacking tidal conversion, *J. Fluid Mech.*, pp. 5–25.
- Martini, K., M. Alford, J. Nash, E. Kunze, and M. Merrifield (2007), Diagnosing a partly standing internal wave in Mamala Bay, Oahu, *Geophys. Res. Lett.*, p. (34) L17605.
- Munk, W., and C. Wunsch (1998), Abyssal recipes II: energetics of tidal and wind mixing, *Deep-Sea Res. I*, pp. 1977–2010.

- Nash, J., M. Alford, and E. Kunze (2005), Estimating internal wave energy fluxes in the ocean, *J. Atmos. Oceanic Technol.*, pp. 1551–70.
- Nash, J., E. Kunze, C. Lee, and T. Sanford (2006), Structure of the baroclinic tide generated at Kaena Ridge, Hawaii, *J. Phys. Oceanogr.*, pp. 1123–35.
- Nycander, J. (2005), Generation of internal waves in the deep ocean by tides, *J. Geophys. Res.*, p. (110) C10028.
- Petruncio, E., L. Rosenfeld, and J. Paduan (1997), Observations of the internal tide in Monterey Canyon, *J. Phys. Oceanogr.*, pp. 1873–1903.
- Pettersson, O. (1908), Strömstudier vid Östersjönsportar, *Sven. Hydrogr. Biol. Komm. Skr.*, pp. 13–37.
- Pinkel, R., and D. Rudnick (2006), Editorial, *J. Phys. Oceanogr.*, pp. 965–66.
- Pomar, L., M. Morsilli, P. Hallock, and B. Badenas (2012), Internal waves, an under-explored source of turbulence events in the sedimentary record, *Earth-Science Rev.*, pp. 56–81.
- Puig, P., A. Palanques, J. Gullen, and M. El Khatab (2004), Role of internal waves in the generation of nepheloid layers on the northwestern Alboran slope: Implications for continental margin shaping, *J. Geophys. Res.*, p. (109) C09011.
- Rainville, L., and R. Pinkel (2006), Baroclinic energy flux at the Hawaiian Ridge: observations from the R/p *FLIP*, *J. Phys. Oceanogr.*, pp. 1104–22.
- Rainville, L., T. Johnston, G. Carter, M. Merrifield, R. Pinkel, B. Dushaw, and P. Worcester (2010), Interference pattern and propagation of the M_2 internal tide south of the Hawaiian Ridge, *J. Phys. Oceanogr.*, pp. 311–25.

- Rosenfeld, L., I. Shulman, M. Cook, J. Paduan, and L. Shulman (2009), Methodology for a regional tidal model evaluation, with application to central california, *Deep-Sea Res. II*, pp. 199–218.
- Rudnick, D., et al. (2003), From tides to mixing along the Hawaiian Ridge, *Science*, pp. 355–57.
- Sharples, J., C. Moore, A. Hickman, J. Holligan, J. Tweddle, M. Palmer, and J. Simpson (2009), Internal tidal mixing as a control on continental margin ecosystems, *Geophys. Res. Lett.*, p. L23603.
- Shea, R. ., and W. Broenkow (1982), The role of internal tides in the nutrient enrichment of Monterey Bay, California, *Cont. Shelf Res.*, pp. 395–422.
- Shepard, F., N. Marshall, and P. McLoughlin (1974), "Internal waves" advancing along submarine canyons, *Science*, pp. 195–98.
- Simmons, H., R. Hallberg, and B. Arbic (2004), Internal wave generation in a global baroclinic model, *Deep-Sea Res. II*, pp. 3043–68.
- Simmons, H., M.-H. Chang, Y.-T. Chang, S.-Y. Chao, O. Fringer, C. Jackson, and D. Ko (2011), Modelng and prediction of internal waves in the South China Sea, *Oceanogr*, pp. 88–99.
- St. Laurent, L., and C. Garrett (2003), The role of internal tides in mixing the deep ocean, *J. Phys. Oceanogr.*, pp. 2882–99.
- Taylor, G. (1920), Tidal friction in the Irish Sea, *Philos. Trans. R. Soc. London, Ser. A*, pp. 1–33.

- Terker, S., J. Girton, E. Kunze, J. Klymak, and R. Pinkel (2012), Observations of the internal tide on the California Continental Margin near Monterey Bay, *Submitted to Cont. Shelf Res.*
- Vlasenko, V., N. Stashchuk, and K. Hutter (2005), *Baroclinic Tides. Theoretical Modeling and Observational Evidence*, pp. 30–40, Cambridge University Press.
- Wang, T., X. Chen, and W. Jiang (2012), Laboratory experiments on the generation of internal waves on two kinds of continental margin, *Geophys. Res. Lett.*, p. (39) L04602.
- Wunsch, C. (1975), Internal tides in the ocean, *Rev. Geophys. Space Phys.*, pp. 167–82.
- Wunsch, C. (2002), What is thermohaline circulation?, *Science*, pp. 1179–81.
- Zhao, Z., and E. D’Asaro (2011), A perfect focus of the internal tide from the Mariana Arc, *Geophys. Res. Lett.*, p. (38) L14609.
- Zhao, Z., M. Alford, J. MacKinnon, and R. Pinkel (2010), Long-range propagation of the semidiurnal internal tide from the Hawaiian Ridge, *J. Phys. Oceanogr.*, pp. 713–36.
- Zilberman, N., J. Becker, M. Merrifield, and G. Carter (2009), Model estimates of M_2 internal tide generation over Mid-Atlantic Ridge topography, *J. Phys. Oceanogr.*, pp. 2635–51.
- Zilberman, N., M. Merrifield, G. Carter, and D. Luther (2011), Incoherent nature of the M_2 internal tides at the Hawaiian Ridge, *J. Phys. Oceanogr.*, pp. 2021–36.

Chapter 2

The EM-POGO: A Simple, Absolute Velocity Profiler

S.R. Terker^{a,b,*}, T.B. Sanford^{a,b}, J.H. Dunlap^a, J.B. Girton^{a,b}

^a*Applied Physics Laboratory
University of Washington
1013 NE 40th Street
Box 355640
Seattle, WA 98105-6698
USA*

^b*School of Oceanography, Box 357940
University of Washington
Seattle, WA 98195-7940
USA*

Abstract

Electromagnetic current instrumentation has been added to the Bathymetry Systems, Inc. POGO transport sondes to produce a free-falling absolute velocity profiler called EM-POGO. The POGO is a free-fall profiler that measures a depth-averaged velocity using GPS fixes at the beginning and end of a round trip to the ocean floor (or a pre-set depth). The EM-POGO adds a velocity profile determined from measurements of motionally-induced electric fields generated by the ocean current moving through the vertical component of the Earth's magnetic field. In addition to providing information about the vertical structure of the velocity, the depth-dependent measurements improve transport measurements by correcting for the non-constant fall-rate. Neglecting the variable fall rate results in errors $O(1 \text{ cm s}^{-1})$. The transition from POGO to EM-POGO included electrically isolating the POGO and electric-field-measuring circuits, installing a functional GPS receiver, finding a pressure case

*Corresponding author

Email addresses: sbrody@apl.washington.edu (S.R. Terker),
sanford@apl.washington.edu (T.B. Sanford), dunlap@apl.washington.edu (J.H. Dunlap),
girton@apl.washington.edu (J.B. Girton)

that provided an optimal balance among crush-depth, price and size, and incorporating the electrodes, electrode collar, and the circuitry required for the electric field measurement. The first EM-POGO sea-trial was in July 1999. In August 2006 a refurbished EM-POGO collected 15 absolute velocity profiles; relative and absolute velocity uncertainty was $\sim 1 \text{ cm s}^{-1}$ and $0.5 - 5 \text{ cm s}^{-1}$, respectively, at a vertical resolution of 25 m. Absolute velocity from the EM-POGO compared to shipboard ADCP measurements differed by $\sim 1-2 \text{ cm s}^{-1}$, comparable to the uncertainty in absolute velocity from the ADCP. The EM-POGO is thus a low-cost, easy to deploy and recover, and accurate velocity profiler.

Keywords: ocean instrumentation, electric field measurements, motional induction, ocean current measurements, velocity profiles

2.1. Introduction

Vertical profiles of ocean currents are essential to studies of depth-dependent physical processes in the ocean such as internal waves (including near-inertial waves, internal tides, and the broadband spectrum), bottom boundary layers, western boundary currents, mid-depth jets, mesoscale eddies, high-latitude overflows, and the energy cascade from internal waves to shear and mixing. Since initial attempts to measure velocity profiles with mechanical current meters proved largely unsatisfactory, a variety of alternative techniques have been used, including acoustically-tracked dropsondes (Pegasus, TOPS)(Spain et al., 1981; Luyten et al., 1982; Hayes et al., 1984), acoustic travel-time (MMP) (Doherty et al., 1999) and Doppler shift (Lowered ADCP) sensors, and motional induction (XCP, AVP, EM-APEX) (Sanford et al., 1985, 2005). Each technique and instrument has different strengths and weaknesses, including water column coverage, ease of use, vertical resolution, sensor suites, and cost. Here we report on an instrument development at the “shoestring” end of the

spectrum, highlighting the potential for a self-contained device, able to be deployed by only 2 people from a small ship, requiring little design cost and using inexpensive components (approximately \$5,000 in total). The result was the EM-POGO, a cost-effective, easy to deploy and recover, free-falling absolute velocity profiler with < 25 m vertical resolution.

The concept for the EM-POGO grew from persistent enthusiasm by Tom Rossby about the inclusion of motional induction sensors (Sanford, 1971; Sanford et al., 1978) in his POGO transport floats (Rossby et al., 1991). This would add value by measuring of the distribution of ocean velocity along the trajectory of the POGO. Furthermore, the combination of the transport meter and the electric field (EF) measurements allows for absolute velocity profiles. Ultimately, Rossby obtained NSF funding to do this and engaged our (Sanford's) group at APL-UW to implement this capability.

The development process, theory, and scientific results to date are described in the following sections: Section 2.2 describes the design and implementation process. The theory of how the EF measurements, obtained as electrode voltages, are interpreted as velocity is briefly discussed in section 2.3. Sea-trials presented in Section 2.4 confirm that the EM-POGO is able to provide accurate absolute velocity profiles data with at least 25 m vertical resolution, relative velocity with standard errors of $< 1 \text{ cm s}^{-1}$ and absolute velocities with a standard deviation of 0.5 - 5 cm s^{-1} .

2.2. Materials and methods

In order to preserve electrical isolation (to minimize noise sources) and conserve design costs, it was decided to add the EF measurement by simply inserting the electronics from the EFF (a RAFOS float with EF measurement capabilities) (Rossby et al., 1986; Sanford et al., 1995) into the POGO tube as a completely separate

system. The POGO technique, based on the primitive free-falling transport float developed and used by Richardson & Schmitz Jr. (1965), has been updated over the years, including the additions of an acoustic pinger for tracking capabilities, a VHF beacon and a xenon flasher to aid recovery, and a new instrument housing. The POGO was designed to free-fall at a constant rate to a pre-determined depth, release drop-weights, and return to the surface at a constant rate providing a straightforward measure of horizontal distance, based on shipboard Loran C readings at the release and recovery times, traveled over time. A temperature profile was also recorded along the trajectory. This method assumes a constant fall/rise rate, which is discussed in Section 2.3. The POGO was used successfully as a transport meter in numerous experiments (Rossby et al., 1991; Pickart & Lindstrom, 1994; Meinen et al., 2000) with an uncertainty of $\pm 0.02 \text{ m s}^{-1}$. GPS was a later addition to the POGO to improve the instrument's ability to determine the start and end positions of the profile. More details of the POGO design and components including tracking and recovery devices and the original POGO circuitry board are discussed in Rossby et al. (1991). Similarly, a more in-depth review of the EFF can be found in Sanford et al. (1995), Szuts (2004) and Szuts & Sanford (2011).

Features and components of the EM-POGO that are new or modified from the POGO or EFF are described below. Mid-way through the development, it became apparent that a new tube had to be selected to fit the wide EFF circuit board. A two-meter long cylindrical glass tube with an aluminum endplate (Fig.1) was constructed (Schott Tubing) with an outer diameter of 11 cm, a wall thickness of 7 mm, a weight of 23.2 lb in air, a buoyancy of 12.3 lb in seawater, and a crush depth of 3324 m, and the hemispherical end was hand-shaped by a glass blower. The temperature sensor, electrode connectors, and the acoustic pinger connectors run through the endplate. The addition of these connectors limits the profiling depth by decreasing the endplate

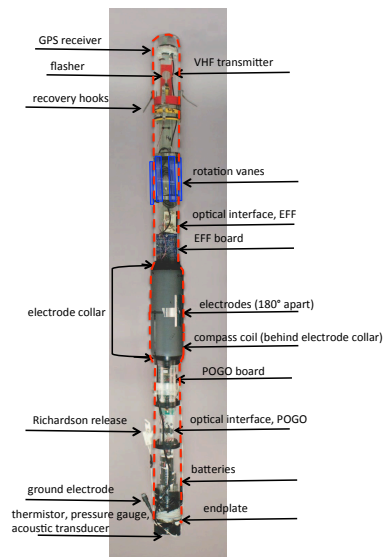


Figure 1: A photograph of the EM-POGO with the major components labeled. The drop weights, optional pressure release, and corrosion links are not shown. The electrodes are covered by silver tape to prevent desiccation. The glass hull is outline by a dashed red line.

pressure rating to less than 2000 m.

The instrument profiles (Fig.2) by changing its buoyancy from negative to positive upon approaching the bottom or a preset pressure level (when operating with a mid-depth pressure release) by dropping weights hung 5 m below the glass tube. A 12-hr back-up corrosion link is also attached between the bottom-release and drop-weight in case the release mechanism fails. The amount of drop-weight is chosen to facilitate an equal fall and rise rate and good vertical resolution. The 5 m of line allows the instrument to decelerate without hitting the bottom. In the 2006 sea trial (Section 2.4.2), the rise and fall rates were $\sim 1.5 \text{ m s}^{-1}$ and the vertical resolution was 25 m. The instrument rotates as it falls and rises to prevent kiting and to modulate the electrode voltage signal. This modulation is necessary because the ocean induced

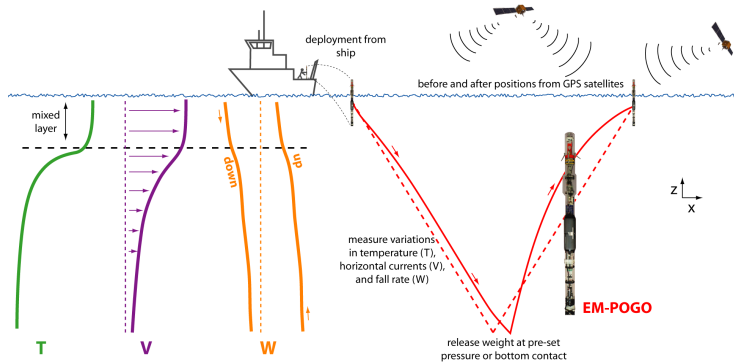


Figure 2: A schematic of the deployment and surfacing of the EM-POGO along with profiles of temperature (T, green), baroclinic velocity (V, solid purple), barotropic velocity (dashed purple), vertical velocity of the instrument (W, yellow, solid lines show the up and down profiles while the dashed line is the zero) and horizontal displacement along the trajectory (red, dashed portrays the results of a constant velocity and fall/rise rate while solid includes the effects of velocity and rise/fall rate variations).

electric field is very small, $O(1 - 10 \mu V/m)$ relative to the temperature ($350 \mu V/^\circ C$) and salinity coefficients ($500 \mu V/PSU$) of the electrodes. The electrodes are encased in agar made with seawater, to form an electrically-conductive seaweed gel, to slow heat and salt transfer to the electrode surfaces. With the EM-POGO electrode separation of 0.14 m, electrode voltages are $O(1 \mu V)$. The vertical resolution can be increased by fitting the data over fewer instrument rotations or increasing the rotation rate. Here, four rotations were used, as this time interval smoothed over much of the noise (Fig.3).

The POGO and the EF components remain completely isolated both physically and electrically on the combined instrument (Fig.4). The POGO board uses Bathy Systems, Inc. firmware and stores the pressure and temperature data. It also controls the pinger, flasher, and radio transmitter. The EF board stores the electrode and

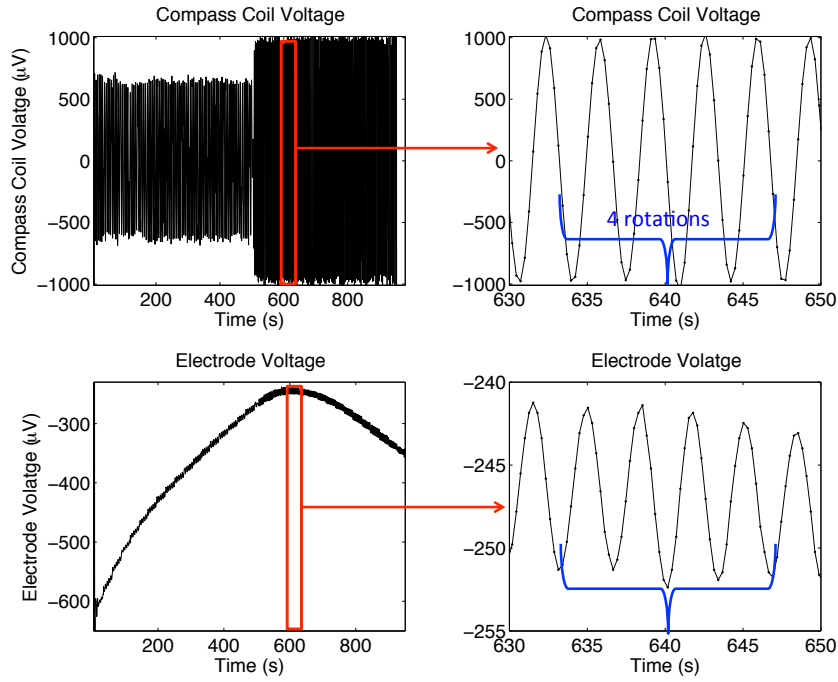


Figure 3: The raw compass coil (upper two panels) and electrode (lower two panels) voltages from EM-POGO drop #107 during the 2006 seatrials. The two left panels are the data for entire profile, while the right panels are a subsection (indicated by the red box) of the right profiles to show the data-fitting window of four rotations. The voltages are fit to four components: mean, trend, sine, and cosine terms. The phase difference between the electrode voltage and compass coil voltage is a result of the angle between the electrode arm axis and the motionally induced voltage between the electrodes. The uncertainty in the velocity resulting from the standard error in the electrode voltage fit (using all of the profiles) is 0.4 cm s^{-1} .

compass voltages and GPS data. A Garmin GPS 16 is used on the EM-POGO; it has wide area augmentation system (WAAS) differential GPS capabilities with a position error of less than 3 m 95% of the time. This small error is crucial for obtaining an accurate measure of the barotropic velocity component. The software on the EF board was amended to receive and store the necessary GPS data.

Isolating the POGO and EF electronics is more cost-effective than a redesigned, smaller circuit board for the EF measurements, or a combined EF and POGO board. Separate magnetic reed switches turn the POGO board and the EF board on and off, and separate optical links are used to offload the data through the glass hull. The POGO data offloads at 1200 baud and the EF data at 9600 baud. No onboard computation is performed. MATLAB software has been written for post-processing and is available to potential users on request.

A compass coil—an air-core solenoid with approximately 10,000 turns of copper wire—is used to determine the direction of the electrode arm and the rotation rate of the instrument. Velocity is estimated first in magnetic coordinates and is later rotated into geographic coordinates. When the compass coil passes through magnetic north and magnetic south, the compass coil signal goes through zero. A critical aspect of the construction is that the angle of the electrode arm relative to the compass coil orientation (close to 90°) must be determined to allow the velocity to be correctly separated into north and east components. In practice, the angle is first measured directly and then fine-tuned during post-processing by minimizing the difference between the down- and upward velocity profiles at the deepest part of the drop, when time differences are minimal.

Considering that the initial goal of the EM-POGO was to combine the two instruments in the most economical way, there are modifications which can improve the instrument performance and the user experience. A new housing material, such

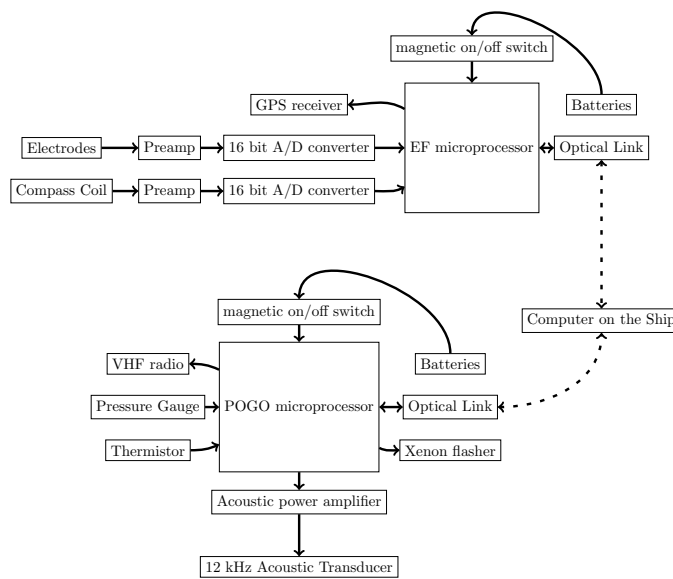


Figure 4: A block diagram of the EM-POGO electrical components. An important feature is the electrical isolation between the POGO and EF systems. To reduce any unwanted common mode response by the EF preamp, its circuit common potential is held close to the seawater potential using an additional Ag/AgCl "ground" electrode (not explicitly shown)

as a graphite, instead of the glass tube would offer a better depth rating and be less fragile. Benefits offered by the glass tube included the ability to see and transmit through the tube allowing for the optical and radio communication while also protecting the flasher. However, the optical offload is quite slow (and operationally awkward) and could now easily be replaced with a wireless communication such as Bluetooth. The radio and flasher would likely need to be moved outside the main instrument housing if the new housing is not transparent to radio and or light. Another improvement would be to increase the rotation rate by redesigning the vanes to increase the vertical resolution. The fall and rise rate could also be slowed to increase the vertical resolution, though this may or may not be desirable depending of the deployment circumstance. A GPS with an external antennae would decrease the time between surfacing and acquiring adequate satellite fixes, but would be costly. Finally, combining the circuit boards, especially since now circuit components are much smaller, would streamline the electronics and make the post processing easier since the two profiles have to be matched and dealt with separately for now.

2.3. Theory and calculations

The horizontal velocity structure is interpreted from electrode voltages collected as the EM-POGO falls through the conductive seawater and the Earth's geomagnetic field. The conversion from electrode voltages to velocity profiles is described in Sanford et al. (1978) and Szuts (2008, 2010a,b). A brief review of the theory of motional induction and its application to a free-falling instrument is presented here. Essential assumptions to ensure that the first order theory can be applied are that the instrument is in equilibrium at all depths with the horizontal motion of the seawater, that the horizontal scale (L) of the flow is much greater than the ocean depth (H) such that ($H/L \ll 1$), depth variations (h) are small such that ($h/H \ll 1$), the

vertical speed of the water is negligible, phase speeds of water motion are less than 10 m s^{-1} , and measurements are above a seabed of uniform conductivity.

The motion of conductive seawater through the earth's magnetic field creates a potential gradient ($\nabla\phi$) in the quasi-static electric field (\mathbf{E}), which in a geomagnetic stationary frame of reference is:

$$-\mathbf{E} = \nabla\phi = \mathbf{v} \times \mathbf{F} - \mathbf{J}/\sigma, \quad (1)$$

where $\mathbf{v} =$ velocity field of the ocean (u, v, w) , $\mathbf{F} =$ geomagnetic field $(0, F_y, F_z)$, $\mathbf{J} =$ electric current density, and $\sigma =$ electrical conductivity of seawater. Under the above assumptions, the electric field is constant, independent of depth (Sanford, 1971; Chave & Luther, 1990) and denoted as

$$\mathbf{E} = -\bar{\mathbf{v}}^* \times \mathbf{F} \quad (2)$$

where $\bar{\mathbf{v}}^*$ is a conductivity-weighted average velocity

$$\bar{\mathbf{v}}^* = \frac{\int_{-H}^0 \mathbf{v}(z) \sigma(z) dz}{\int_{-H_s}^0 \sigma(z) dz}. \quad (3)$$

and H_s is the depth including a layer of bottom conducting sediment. The ratio of sediment conductance to water column conductance is $\sim 0 - 0.2$ (Sanford et al., 1985; Sanford, 1986; Chave & Luther, 1990). A more complete description of the intermediate steps of the application of the theory of motional induction to a free falling platform can be found in Sanford et al. (1978), but in short, the depth layers of the ocean (with $H/L \ll 1$) can be represented as an equivalent electric circuit, where the potential gradient between two points is depth-independent and proportional to

$(\bar{\mathbf{v}}^*)$.

The instrument does not operate in a stationary frame of reference but moves horizontally with water, producing a potential gradient in the electrode arm that cancels that in the ocean caused by the horizontal motion of the water. This leaves an electric field signal equal to \mathbf{J}/σ with an additional contribution from the fall rate (W) of the electrode arm through the horizontal component of the earth's magnetic field.

The EF-derived velocity (based on observed electrode voltages later described in (8) and (9)), noted as \mathbf{v}_{EF} , has to be adjusted by this conductivity-weighted velocity $\bar{\mathbf{v}}^*$ to determine the absolute velocity of the ocean, \mathbf{v} as

$$\mathbf{v}_{EF}(z) = \mathbf{v}(z) - \bar{\mathbf{v}}^*. \quad (4)$$

The GPS system provides an estimate of $\langle \mathbf{v} \rangle$ as the distance (X) traveled over time (T) is

$$\langle \mathbf{v}_{GPS} \rangle = \frac{\Delta X}{T} \quad (5)$$

where $\langle \rangle$ denotes the vertical average over the time, including both down and up profiles, such that

$$\langle \rangle = \frac{1}{2} \left(\frac{-1}{z} \int_0^{-z} () dz + \frac{1}{z} \int_{-z}^0 () dz \right). \quad (6)$$

If the instrument goes to the bottom, then $z = H$.

Both $\langle \mathbf{v}_{GPS} \rangle$ and $\langle \mathbf{v}_{EF} \rangle$ can be calculated from measurements; thus $\bar{\mathbf{v}}^*$ is solved by rearranging and taking the depth-average of (4)

$$\bar{\mathbf{v}}^* = \langle \mathbf{v}_{GPS} \rangle - \langle \mathbf{v}_{EF} \rangle. \quad (7)$$

Now (4) is solved for $\mathbf{v}(z)$. We observe a linear relationship between $\langle \mathbf{v}_{GPS} \rangle$ and $\bar{\mathbf{v}}^*$ which ensures that we are in a region where the first order linear theory (presented above) applies. Higher order terms may need to be considered in regions with considerable horizontal velocity gradients and steep topographic gradients (Szuts, 2008).

Equations (1) through (7) summarize the one dimensional theory of motional induction and allow us to solve for velocity, $\mathbf{v}(z)$, given that $\mathbf{v}_{EF}(z)$ is obtained by the EM-POGO. Velocity $\mathbf{v}_{EF}(z)$ results from the interpretation of the measured electric field (Fig. 3) observed by electrodes (on the outside of the electrode collar mounted on the glass pressure vessel, Fig. 1). This interpretation requires knowledge about the instruments impact on the ocean electric currents (which are distorted by the electrode collar) and the effect arising from the instruments velocity through the horizontal component of the Earth's magnetic field. Due to the electrode collar, the horizontal electric current (J_y) path is longer, and the electric current density is increased. If the collar were a long insulating cylinder the combination of longer path and higher current electric current density produces an observed voltage that is twice \mathbf{J}_y/σ times the collar diameter (l). This effect is incorporated into the interpretation of the observations by adjusting for the effect with a term $1 + C_1$, where C_1 is 0.97. The profiler velocity through the horizontal component of the Earth's magnetic field creates a voltage which amounts to $F_y l W (1 + C_2)$ and is oriented in the E-W direction. The coefficient C_2 has value of -0.02. Blocks of 4 revolutions of electrode and coil voltages (Fig. 3) are least-squares fit to a mean, trend and sine and cosine functions. The process produces a time series of electrode voltage amplitude (A) and phase difference between the electrode and compass coil voltages, denoted as θ after correction for the fixed angle between orientation of the electrode arm and coil axis. The magnetic east and north components of the

observed electrode voltage, denoted as $\Delta\phi_e$ and $\Delta\phi_n$, respectively, are:

$$\Delta\phi_e = A(z)\sin\theta(z) = -F_z l(v(z) - \bar{v}^*)(1 + C_1) + lF_y W(1 + C_2) \quad (8)$$

and

$$\Delta\phi_n = A(z)\cos\theta(z) = F_z l(u(z) - \bar{u}^*)(1 + C_1). \quad (9)$$

The second term on the right hand side of (8) is subtracted from the measured signal allowing us to solve for $v_{EF}(z)$ and since (9) is not effected by the fall rate, we can simply solve for $u_{EF}(z)$.

In addition to the vertical structure that the electrode voltages provide, the measured fall-rate and vertical velocity structure can be used to improve the transport estimate by taking account of the variable amount of time spent in each depth layer. The POGO, with no depth-dependent information, calculates $\langle \mathbf{v} \rangle$ as distance over time (T). This is a simplification of what is actually being measured, which depends on the fall rate,

$$\langle \mathbf{v} \rangle T = \int_0^T \mathbf{v}(t) dt, \text{ where } dt = dz/W(t) \quad (10)$$

and dt is the time interval over which the data are fitted (four instrument rotations are used). If Reynolds decomposition is used to define \mathbf{v} and W in terms of average ($\langle \rangle$) (both time and depth averages need to be considered) and fluctuating ($'$) components, equation (10) can expanded and written as (11). A profile needs to be separated into up and down segments (indicated by subscripts "up" and "do") because $\langle W_{do} \rangle$

differs from $\langle W_{up} \rangle$.

$$\langle \mathbf{v} \rangle T = \langle \mathbf{v}_{GPS} \rangle T + \frac{-1}{\langle W_{do} \rangle^2} \int_0^{-z} \mathbf{v}'(z) W'_{do}(z) dz + \frac{-1}{\langle W_{up} \rangle^2} \int_{-z}^0 \mathbf{v}'(z) W'_{up}(z) dz \quad (11)$$

The first term on the right side of (11) is unrelated to the the vertical velocity of the instrument, and is what would be predicted by the POGO (Fig. 2, red dashed line versus red solid line), while the second and third terms on the right side depend on the fall rate. The error resulting from neglecting these two terms based on the 2006 sea trials is on the order of 1 cm s^{-1} .

2.4. Results

2.4.1. Grand Bahama Island sea trial: 1999

In July 1999 the EM-POGO was tested from aboard the R/V *Seward Johnson* off the south coast of Grand Bahama Island (Fig.5a) (Sanford et al., 2000). Initial tethered deployments indicated that the instrument was acting strangely and numerous other tethered drops were done to isolate the problems. Eventually, and despite a smaller than expected compass signal, a few untethered EM-POGO drops were completed. It was determined that the two halves of the compass coil were wired in opposition, greatly reducing the output voltage. There was no time to open the instrument and correct the problem, because the seal on the endplate would have required 24 h to cure.

In spite of the compass problems, the velocity measurement returned data usable for comparison with the shipboard RDI 38-kHz ADCP (Fig.6) (Sanford et al., 2000). The comparison is in "along-flow" and "cross-flow" components because the weak compass signal made it difficult to determine the velocity direction independent of the velocity signal itself. The EM-POGO down profile took about 15 min and the up

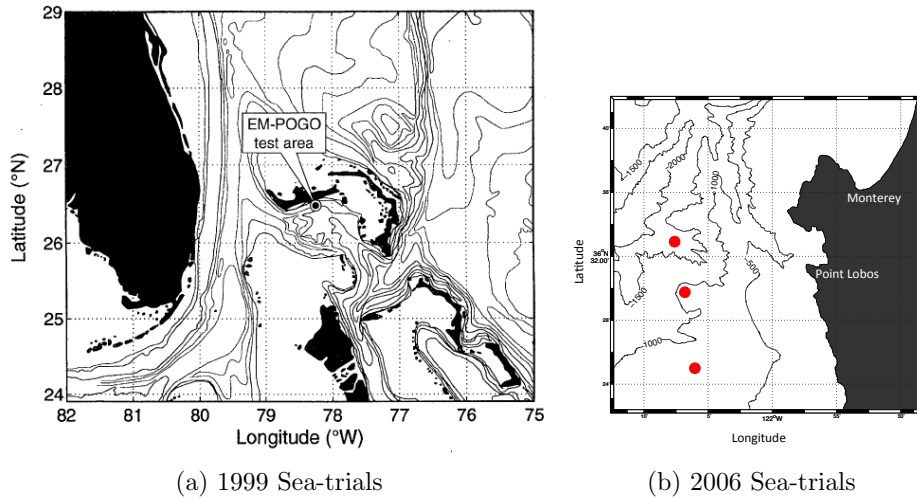


Figure 5: The EM-POGO deployment locations (a) off the southern coast of Grand Bahama Island in 1999 (Sanford et al., 2000) and (b) in the Monterey Bay region in 2006. The 2006 sea trial included deployments at several stations (red circles); bathymetry is contoured in 500-m intervals.

profile took only 4 min. Overall, the instrument agreement, especially in large scale vertical structure, is within 3 cm s^{-1} . The EM-POGO profile used here was relative and shifted to best match the ADCP data. Unfortunately, the GPS receiver did not provide reliable fixes during this trial, probably because of an unexpected sensitivity to platform motion. Nevertheless, the sea-trials did successfully demonstrate the capabilities of the instrument as a low-cost velocity profiler.

2.4.2. Monterey Bay region sea trial: 2006

After a second trial from a cruise in the Faroe Bank Channel on the RRS *Discovery* in 2000 (during which a replacement GPS unit again failed to return any usable data) a third refurbishment effort was undertaken in 2006. The sea-trials for this revitalized EM-POGO took place in August 2006 aboard the R/V *Pt. Sur* during a

Comparison of EM-POGO and ADCP Profiles

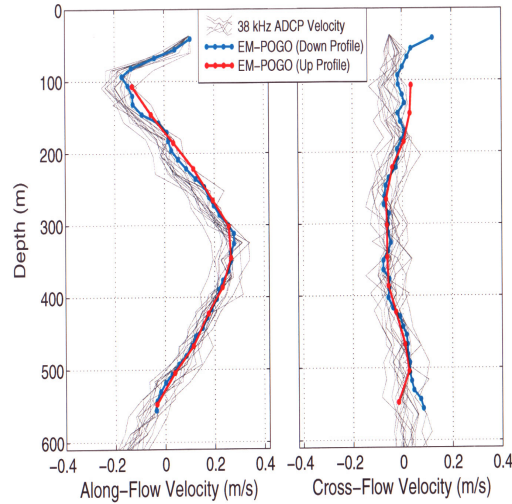


Figure 6: From Sanford et al. (2000), which documents the 1999 EM-POGO sea trial. Velocity from an EM-POGO profile (blue = down, red = up) and 15 1-min averages of concurrent ADCP (thin gray lines) profiles are compared in along-flow and cross-flow components.

cruise that was part of the Office of Naval Research Assessing the Effects of Submesoscale Ocean Parameterizations (AESOP) experiment. A main focus of the cruise was to measure the energetics of the internal tide south of Monterey Bay Submarine Canyon (Terker et al., 2011). The EM-POGO was used to provide supplementary profiles between XCP and LADCP measurements at several time-series sites. Fifteen profiles were successfully completed between August 11th and August 19th (Fig.5b) at three locations within the AESOP survey.

A full water-column velocity and temperature profile from drop #109 (The 9th drop using EM-POGO #1) in 2006 (Fig.7) shows that the down profile is missing data at the top due to contamination of the electric field measurements from the ship during the instrument launch and the up profile is slightly coarser in resolution

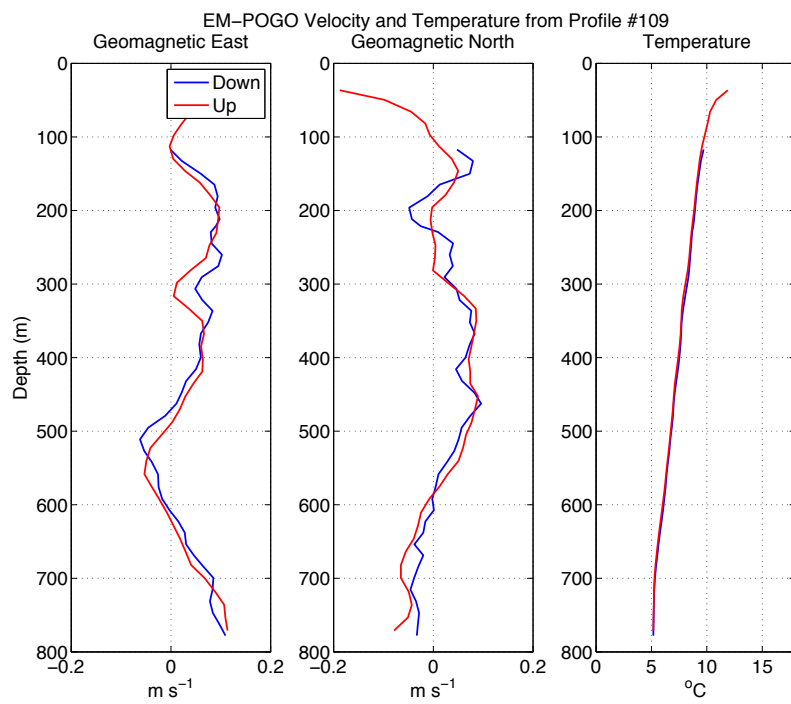


Figure 7: Down (blue) and up (red) profiles of geomagnetic east and north components of velocity and temperature from EM-POGO drop #109 during the 2006 sea trial.

due to a 0.5 m s^{-1} increase in rise rate compared to the fall rate (this change in speed is also responsible for the change in magnitude of the compass coil signal after the instrument hits the bottom in Fig. 3).

To quantify how well the instrument performed, the main sources of error have to be examined. The uncertainty in the relative velocity is $0.5\text{-}1.5 \text{ cm s}^{-1}$; it was quantified using the rms difference between the up and down profiles between 50 and 200 m above the deepest point of the profile. The depth range was chosen to minimize real-time variability. The error in the barotropic velocity, $0.5\text{-}5 \text{ cm s}^{-1}$, arises from the limitations of GPS accuracy and the uncertainty associated with the backwards extrapolation of GPS surface drift to the location where the instrument surfaced. It usually took about five minutes for the EM-POGO to acquire a GPS fix after surfacing. GPS fixes can be acquired quicker, though at a cost, by using a GPS with an external antenna which can be higher above the ocean surface. That antenna is much more expensive as it needs to survive ocean pressure, and a pricey underwater connector is needed.

The shipboard 75-kHz ADCP is compared to the EM-POGO velocity profiles for an independent measure of the EM-POGO instrument performance (Fig. 8). Overall, considering the uncertainty in both instruments, the ADCP and EM-POGO agree reasonably well. The largest errors in the ADCP resulted from heading errors, $0.5\text{-}1 \text{ cm s}^{-1}$, which are proportional to the ship's speed (Joyce, 1989). After the EM-POGO was dropped the ship steamed away to minimize the contamination of the electric field by the ship, and the ship was maneuvering during the recovery; both caused errors in the ADCP measurements. Despite these, the barotropic velocity comparison between the EM-POGO and ADCP has a rms difference of $1.5\text{-}3 \text{ cm s}^{-1}$ and a relative velocity rms difference of $2\text{-}3 \text{ cm s}^{-1}$. The apparent depth offset between shear layers in the ADCP and EM-POGO around 500 m in Fig. 8 is curious,

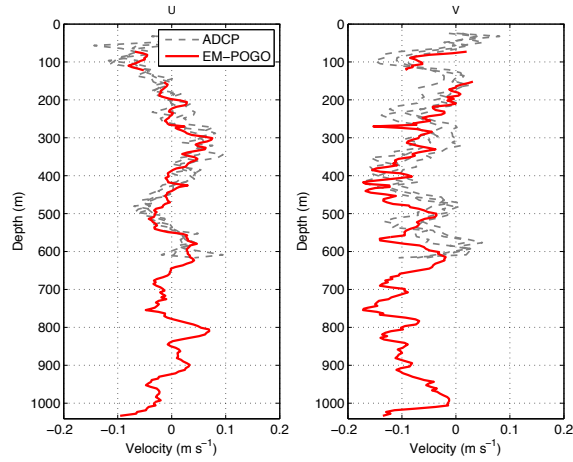


Figure 8: East and north velocity from the upward profile of EM-POGO drop #103 (red) and concurrent ADCP (gray, dashed) profiles during the 2006 sea trial. ADCP data are averaged into 5-min bins, so the three profiles shown represent 15 min of ADCP data.

and may result from a combination of EM-POGO pressure sensor errors (hysteresis and thermal sensitivity) or real spatial or temporal variability.

2.5. Conclusion

The combination of the POGO and EF measurements resulted in a reliable and accurate absolute velocity profiler. Advantages of the EM-POGO are the relatively low cost, the ease of deployment and recovery, the fast fall and rise rates, and the ability to profile up to 1500 m. In the future, the EM-POGO could be an economical choice of velocity profiler for non-research vessel use—able to be deployed from a range of boat sizes and configurations and not requiring much additional equipment, aside from a radio-direction-finder or hydrophone for recovery and computer for data acquisition.. The weaknesses are the limited vertical resolution, the limit of the accuracy of the barotropic velocity due to the time it takes for the GPS to

acquire adequate satellite fixes upon surfacing, and the time it takes to offload the data after each profile. Based on these strengths and weaknesses, the EM-POGO is appropriate for preliminary investigations of regions of rough topography and strong currents and vertical shear. In practice (for the small number of EM-POGOs built to date), the development and troubleshooting by a team of highly-skilled engineers proved to outweigh the benefits of the low cost of the components, but as with all such development efforts, invaluable experience was obtained. If the EM-POGO were to be used again, the modifications mentioned at the end of Section 2.2 would improve both the instruments performance and the practicality.

2.6. Acknowledgements

We are pleased to contribute to this DSR issue in honor of Tom Rossby. As the driving force behind the EM-POGO development and the PI of the NSF grant that supported the work, he deserves much of the credit for its successes. Additionally, he sent us a few of his EM-POGOs to use for the 2006 sea trial. Were this paper not specifically written for the special issue, he would undoubtedly have been a co-author. We thank the contributions from Vern Miller and Robert Drever in the mechanical and electronic design, respectively. The project was supported by NSF grant OCE 9617869 to University of Rhode Island, which provided a subcontract to us for the actual development. The 1999 sea-trials aboard the R/V Seward Johnson were funded under NSF grant OCE 9731543. Observations aboard the R/V Point Sur in 2006 were part of the ONR AESOP project and funded under grant N00014-05-1-0332.

2.7. Bibliography

- Chave, A., & Luther, D. (1990). Low-frequency, motionally induced electromagnetic fields in the ocean: 1. Theory . *J. Geophys. Res.*, *95*, 7185–7200.
- Doherty, K., Frye, D., Liberatore, S., & Toole, J. (1999). A moored profiling instrument. *J. Atmos. and Oceanic Technol.*, *16*, 1816–1829.
- Hayes, S., Milburn, H., & Ford, E. (1984). TOPS: A free-fall velocity and CTD profiler. *J. Atmos. and Oceanic Technol.*, *1*, 220–236.
- Joyce, T. M. (1989). On in situ “calibration” of shipboard ADCPs. *J. Atmos. and Oceanic Technol.*, *6*, 169–172.
- Luyten, J., Needell, G., & Thomson, J. (1982). An acoustic dropsonde — design, performance and evaluation. *Deep-Sea Res. Part A.*, *29*, 499–524.
- Meinen, S., D.R., W., & Clarke, R. (2000). Absolutely referenced geostrophic velocity and transport on a section across the North Atlantic Current. *Deep-Sea I*, *47*, 309–322.
- Pickart, R., & Lindstrom, S. (1994). A comparison of techniques for referencing geostrophic velocities. *J. Atmos. and Oceanic Technol.*, *11*, 814–824.
- Richardson, P., & Schmitz Jr., W. (1965). A technique for direct measurement of transport with application to the Straits of Florida. *J. Mar. Res.*, *18*, 1089–1109.
- Rosby, T., Dorson, D., & Fontaine, J. (1986). The RAFOS system. *J. Atmos. and Oceanic Technol.*, *3*, 672–679.
- Rosby, T., Fontaine, J., & Hummon, J. (1991). Measuring mean velocities with POGO. *J. Atmos. and Oceanic Technol.*, *8*, 713–717.

- Sanford, T. (1971). Motionally induced electric and magnetic fields in the sea. *J. Geophys. Res.*, *76*, 3476–3492.
- Sanford, T. (1986). Recent improvements in ocean current measurement from motional electric fields and currents. In *Proceedings of the IEEE/OES Third Working Conference on Current Measurement Technology* (pp. 65–76).
- Sanford, T., Allison, M., & Dunlap, J. (2000). *R/V Seward Johnson cruise 9908: Cruise report and preliminary results*. Technical Report 7-00 Applied Physics Lab - University of Washington.
- Sanford, T., Carlson, J., Dunlap, J., Webb, D., & Girtton, J. (2005). Autonomous velocity and density profiler: EM-APEX. In *Proceedings of the IEEE/OES Eighth Working Conference on Current Measurement Technology* (pp. 152–156).
- Sanford, T., Drever, R., & Dunlap, J. (1978). A velocity profiler based on the principles of geomagnetic induction. *Deep-Sea Res.*, *25*, 183–196.
- Sanford, T., Drever, R., & Dunlap, J. (1985). An acoustic Doppler and electromagnetic velocity profiler. *J. Atmos. and Oceanic Technol.*, *2*, 110–124.
- Sanford, T., Drever, R., & Dunlap, J. (1995). Barotropic ocean velocity observations from an electric field float, a modified rafofs float. In *Proceedings of the IEEE/OES Fifth Working Conference on Current Measurement Technology* (pp. 163–168).
- Spain, P., Dorson, D., & Rossby, H. (1981). PEGASUS: A simple, acoustically tracked, velocity profiler. *Deep-Sea Res. Part A.*, *28*, 1553–1567.
- Szuts, Z. (2008). *The interpretation of motionally induced electric fields in oceans of complex geometry*. Ph.D. thesis University of Washington Seattle, Washington.

- Szuts, Z. (2010a). Relationship between ocean velocity and motionally induced electrical signals: 1. in the presence of horizontal velocity gradients. *J. Geophys. Res.*, *115*, C06003.
- Szuts, Z. (2010b). Relationship between ocean velocity and motionally induced electrical signals: 2. in the presence of sloping topography. *J. Geophys. Res.*, *115*, C06004.
- Szuts, Z., & Sanford, T. (2011). Observations of vertically-averaged velocity in the North Atlantic Current. *Deep-Sea Res. II, This issue*.
- Szuts, Z. B. (2004). *Electric field floats in the North Atlantic Current: validation and observations*. Master's thesis University of Washington Seattle, Washington.
- Terker, S., Girton, J., Kunze, E., Klymak, J., & Pinkel, R. (2011). Observations of the internal tide in the California Continental Margin near Monterey Bay. *Submitted to Cont. Shelf Res.*, .

Chapter 3

Observations of the Internal Tide on the California Continental Margin near Monterey Bay

**Observations of the Internal Tide on the California Continental Margin near
Monterey Bay**

Samantha R. Terker^a, James B. Girton^a, Eric Kunze^a, Jody M. Klymak^b and Robert
Pinkel^c

^a *Applied Physics Laboratory and School of Oceanography, University of Washington,
Seattle, Washington*

Applied Physics Laboratory
University of Washington
1013 NE 40th Street
Seattle, WA 98105-6698
USA

^b *School of Earth and Ocean Sciences, University of Victoria, Victoria, British Columbia*

School of Earth and Ocean Sciences
University of Victoria
P.O. Box 3055 STN CSC
Victoria, BC Canada V8W 3P6

^c *Scripps Institution of Oceanography, University of California, San Diego, California*

Scripps Institution of Oceanography
University of California San Diego
9500 Gilman Drive
La Jolla, CA, 92093
Mail Code: 0213

Samantha R. Terker email: sbrody@apl.washington.edu
James B. Girton email: girton@apl.washington.edu
Eric Kunze email: kunze@apl.washington.edu
Jody M. Klymak email: jklymak@uvic.ca
Robert Pinkel email: rpinkel@ucsd.edu

Corresponding Author: Samantha R. Terker
Telephone number: 1-516-241-9927
Fax: 206-543-6785
Mailing address:
Applied Physics Laboratory
Attn: Samantha Terker
University of Washington
1013 NE 40th Street
Seattle, WA 98105-6698
USA

Abstract:

Observations of the semidiurnal internal tide on the California continental margin between Monterey Bay and Point Sur confirm the existence of northward energy flux predicted by numerical models of the region. Both a short-duration tide-resolving survey with expendable profilers and a multi-week timeseries from *FLIP* measured northward flux in the mean, supporting the hypothesis that topographic features off Point Sur are the source of the strong internal tides observed in Monterey Canyon. However, the observed depth-integrated semidiurnal flux of $500 \pm 200 \text{ W m}^{-1}$ is approximately twice as large as the most directly-comparable model and *FLIP* results. Though dominated by low modes with $O(100 \text{ km})$ horizontal wavelengths, a number of properties of the internal tide, including semidiurnal energy fluxes, kinetic and potential energies, show lateral variability on $O(5 \text{ km})$ scales, underscoring the complexity of the internal tide in areas of rough bathymetry where there are waves from multiple sources. A simple two-source model of a first- mode interference pattern reproduces some of the most striking aspects of the observations. Potential causes of this spatial variability include interference of waves from multiple sources, the sharp delineation of beams generated by abrupt topography due to limited azimuthal extent, and local generation and scattering of the internal tide into higher modes by small-scale topography.

Keywords: internal tides, spatial variability, Monterey Bay

3.1 Introduction:

Establishing and quantifying sources, pathways, and sinks of internal (baroclinic) tidal energy is imperative to closing the global tidal energy budget, yet the processes influencing the propagation and dissipation of the internal tide are less well understood than its generation. The theory of internal tide generation has been studied for over 30 years, and essential dimensionless parameters—tidal excursion compared to the horizontal scale of the topography, bottom slope compared with the angle at which the tidal rays propagate, and the height of the topography relative to the depth of the ocean—have been identified (Bell, 1975; Baines, 1982; Garrett and Kunze, 2007; Nycander, 2005).

We are not far from achieving realistic global maps of internal tide generation. Satellite altimetry and numerical models have characterized the geography of the energy lost from the barotropic (surface) tide (Egbert and Ray, 2001), and more recent work has focused on the partition of this loss between dissipation and conversion into baroclinic motions—i.e., internal tide generation (Carter et al., 2008; Simmons et al., 2004). Most of the barotropic tide loss occurs at a limited number of topographic features (~75% of at 20 sites). *In situ* measurements at sites such as the Hawaiian Ridge (Klymak et al., 2006; Lee et al., 2006; Nash et al., 2006; Rainville and Pinkel, 2006), Mendocino Escarpment (Althaus et al., 2003), Luzon Strait (Lien et al., 2005), and the Bay of Biscay (New, 1988) confirm generation of the internal tide at sites highlighted by the global maps.

Once generated, the propagation of the waves through an inhomogeneous medium, their subsequent interactions with topography and interactions among different

waves become increasingly complicated, particularly as the end results of dissipation and fluid mixing are approached. Global maps of propagation are more problematic, but initial steps have been made. The first-mode internal tide (i.e., the largest baroclinic length scale) generated by a simple topographic feature like the Hawaiian Ridge is relatively straightforward to observe, and has been traced over thousands of kilometers. Where the energy is ultimately dissipated remains largely unquantified (Alford, 2003; Ray and Mitchum, 1996; Zhao et al., 2010). At the same time, internal tides (particularly higher modes) may be refracted by mesoscale features and changing water depths (Martini et al., 2007; Park and Watts, 2006; Rainville and Pinkel, 2006), modified through wave-wave interactions (MacKinnon and Winters, 2005), and can produce multiple-source interference patterns (Nash et al., 2007; Rainville et al., 2010; Simmons, et al., 2004), complicating interpretation of maps and point measurements alike.

The end products of dissipation and mixing are still more difficult to map out, as these processes tend to be intermittent and localized, involving a cascade to smaller scales, wave breaking and turbulence. Internal tide dissipation may be gradual through internal wave/wave interactions (McComas and Müller, 1981a,b) and scattering from small-scale rough topography (St. Laurent and Garrett, 2002) or abrupt due to parametric subharmonic instability equatorward of 28° (Alford et al., 2007; Hazewinkel and Winters, 2011; MacKinnon and Winters, 2005), reflection to high wavenumbers at near-critical bottom slopes (Nash et al., 2004; Nash et al, 2007), and shoaling onto shelves (Lien et al, 2005; Moum et al., 2002). While all these processes are likely to occur, it is unknown which dominate, though observations of long-range propagation of low-mode

tides (as mentioned earlier) suggest that gradual dissipation processes are weak and the abrupt processes play a more substantial role in dissipating the internal tide.

As a potential site for unusual internal wave dynamics and strong mixing, the shelf and canyon topography of the Monterey Bay region were the focus of several observational programs and modeling efforts in the 1990s and 2000s (Carter and Gregg, 2002; Kunze et al., 2002; Petrucio et al., 1998, Rosenfeld et al., 2009). These studies found topographically steered baroclinic tidal currents of $\sim 20 \text{ cm s}^{-1}$, more than twice as large as the barotropic currents. Microstructure measurements at the head of the canyon to depths up to 400-m also showed high average dissipation rates $O(1.1 \times 10^{-6} \text{ W kg}^{-1})$, which varied spatially and temporally but peaked along the canyon axis during spring tide (Carter and Gregg, 2002). Deeper microstructure measurements in the canyon to depths up to 1200-m reveal well-stratified turbulent near-bottom layers 200-300 m thick with average dissipation rates $O(4 \times 10^{-8} \text{ W kg}^{-1})$ (Kunze et al., 2011).

The source(s) of this enhanced internal tide energy within Monterey Canyon remained largely unexplained until numerical models were run with sufficient resolution and coverage to simulate generation by features outside of Monterey Bay, including the Sur Ridge, Sur Platform, Guide Seamount and Davidson Seamount (Carter, 2010; Hall and Carter, 2011; Jachec et al., 2006; Wang et al., 2009). Though differing in detail, these models all suggest that the majority of the internal tide enters the canyon from the south in a beam originating from submarine topography west of Point Sur (including both the Sur Ridge and Sur Platform; Fig. 1). The purpose of the study described in this paper is to characterize lateral variability in internal tide properties on scales smaller than the robust and coherent internal wave beam but larger than the resolution of the finer models (Carter

2010; Jachec et al., 2006). Even for a relatively well-studied deterministic process such as internal tides, convergence between high-resolution models and observations is far from being achieved in this region (Rosenfeld et al., 1999; Rosenfeld et al., 2009; Wang et al., 2009).

This paper is organized as follows: Section 3.3.2 describes our recent measurement program on the California continental margin between Pt. Sur and Monterey Canyon (Fig. 1), including the initial results and a comprehensive evaluation of uncertainties. Section 3.3.3 documents the surprising (given the low-mode character, relatively simple geometry, and modeled smoothness of the internal tide) complexity at $O(5 \text{ km})$ spatial scales. Section 3.3.4 evaluates potential hypotheses for this complexity, including constructive and destructive interference resulting from the superposition of waves propagating from multiple sources (Rainville et al., 2010) and the abrupt shifts in energy flux that can arise at the edges of beams of limited azimuthal extent. The complexity underscores the importance of the consideration of spatial and temporal resolution in oceanographic field experiments in which observations are often limited by the high cost of instruments and ship time.

3.2. Methods

3.2.1 Field Measurements

The AESOP (Assessing the Effectiveness of Sub-mesoscale Ocean Parameterizations) experiment was conducted in the Monterey Bay region during

August-September 2006 as part of the “MB06” suite of activities. This experiment was designed to test and improve the representation of small-scale processes in coastal regional numerical models. It provided a unique opportunity to make full-water-column profiles of velocity, temperature and pressure with high spatial resolution in an area with complex bathymetry and an energetic internal wave field.

The principal observations presented in this paper are from 10 stations west of Point Sur in ~1000-m of water. The stations are comprised of a 5-km x 5-km survey box plus one station 6 km to the south, occupied by the R/V *Point Sur* during 13–15 August (Fig. 1). Full-depth profiles were collected with Lockheed-Sippican expendable current profilers (XCPs), a ship-lowered CTD/LADCP package, two shipboard RDI ADCPs (a 75-kHz Ocean Surveyor and 300-kHz BroadBand), and a Rockland Scientific Vertical Microstructure Profiler (VMP). The spatial and temporal sampling was irregular due to an unexpectedly high (approximately 30%) XCP failure rate and the requirement to retrieve the expendable surface float transmitters as a condition of the Monterey Bay National Marine Sanctuary permit. Although unable to overlap with the shipboard survey due to Navy tug scheduling changes, R/P *FLIP* collected a continuous timeseries of velocity profiles with 45 minute resolution from 20 August – 7 September near the center of the survey box (the green “F” in Fig. 1 between stations B4 and B9).

Rapid circuits of the survey box (stations B1-B9, Fig. 1a, in numerical order) were made for two consecutive daytime tidal cycles (*i. e.*, 36 hours with a 12-hour gap in the middle) on 13–14 August, using XCPs while cruising continuously at 6–8 kts. Care was taken to distribute samples over the semidiurnal tidal phase as evenly as possible. LADCP/CTD profiles were used at the end of the survey to fill in gaps at stations with

high rates of XCP failure. The net result was at least four, and usually five, occupations of each of the nine box stations. The error associated with this sampling strategy are discussed in Sections 3.2.3 and 3.2.4.

It is important to note that two additional sources of internal tide data were added to three of the stations: On 15 August, a daytime 12-hour timeseries with XCP profiles every half hour was collected at station B6, on the south side of the survey box. Also, on 13–15 August, CTD profiles from the VMP were collected at B5, B6, and B9 during nightly sampling from 2100 until 0900 the following day (one station with 5–7 profiles each night). The extra data were added to the harmonic fits for internal tide pressure (VMP, CTD and LADCP) and velocity (CTD and LADCP only) in order to achieve the best-available estimates. As a check on possible biases introduced by this extra data, semidiurnal fits and energy fluxes were also computed at B5, B6 and B9 using only the 13–14 August daytime sampling described above, yielding a more homogeneous, but less accurate, dataset (magenta arrows in Fig. 2).

Briefly, the results of the survey are as follows: The integrated energy flux vectors (Fig. 2) show generally northward flux, roughly consistent with the Jachec et al. (2006) beam from the ridges off Point Sur. Exceptions to this are found at stations B5 and B6, where fluxes are significantly smaller. The vertical profiles (Fig. 3) reveal surface and bottom-intensified fluxes, consistent with the expected low-mode structure, as well as evidence of crossing beams at several depths.

The FLIP timeseries provides a vital tool for interpreting the temporal context of the XCP survey. As found previously in Monterey Canyon (Kunze et al., 2002), semidiurnal frequencies and their harmonics dominate frequency spectra at the *FLIP*

location. However, the timeseries of semidiurnal energy flux reveals significantly more complex variability than the simple fortnightly spring–neap cycle of the barotropic tide (Fig. 4). In addition, diurnal internal wave energy and flux are present (Fig. 4) which are highly correlated with the barotropic diurnal tide. Prior to the experiment, the diurnal band was not expected to contribute significantly to internal wave energy flux, as these frequencies lie below the local inertial frequency and cannot support freely-propagating internal waves at this latitude. However, coastally-trapped wave solutions are possible (Dale et al., 2001), and the AESOP location on the continental slope lies well within the trapping region. This neglect of the diurnal band, therefore, contributes to the error in our results, as discussed in Section 3.2.4.

3.2.2 Energy Flux and Energy Calculations

Semidiurnal (SD) internal tide energy flux, $\bar{F}_E^{SD}(z)$, is calculated after removing the depth-averaged velocity and pressure perturbation from each profile (Althaus et al., 2003; Kunze et al., 2002; Nash et al., 2004; Nash et al., 2005). This surface/internal tide decomposition has recently been evaluated by Kelly et al. (2010b) who found that surface-tide pressure was best-represented by depth-averaged pressure plus an additional depth-dependent pressure profile arising from isopycnal heaving due to movement of the free surface. Since the region we were in had only small sea-surface displacements, the second term can be neglected.

The horizontal and vertical semidiurnal energy fluxes

$$\bar{F}_{E_{hor}}^{SD} = \langle \bar{u}'(z)P'(z) \rangle = \frac{1}{2} A_u^{SD}(z) A_P^{SD}(z) \left(\cos(\phi_u^{SD}(z) - \phi_P^{SD}(z)) \right) \quad (1a)$$

$$F_{E_{vert}}^{SD} = \langle w'(z)P'(z) \rangle, \quad (1b)$$

are defined as the time- or period-averaged ($\langle \rangle$) covariance of the baroclinic fluctuations (\bar{u}) in velocity \mathbf{u} (u, v, w) and pressure P . Harmonic fits,

$$\bar{u}_{SD}(z) = A_u^{SD}(z) \cos(\phi_u^{SD}(z) - \omega_{SD}t), \quad (2)$$

are found by minimizing mean-squared deviations to the demeaned velocity at each depth at each station. This yields amplitudes and phases, A_u^{SD}, A_P^{SD} and ϕ_u^{SD}, ϕ_P^{SD} . Because of short one to two day windows used for the fitting, results are not sensitive to the exact frequency used (we used $\omega_{SD} = 1.4 \times 10^{-4} \text{ rad s}^{-1} = M_2$ frequency) such that M_2, S_2 and other semidiurnal frequencies are indistinguishable.

Harmonic coefficients (2) are also used to obtain vertical profiles of horizontal kinetic energy HKE and available potential energy APE

$$HKE(z) = \frac{1}{2} \left(\left(A_u^{SD}(z) \right)^2 + \left(A_v^{SD}(z) \right)^2 \right) \quad (3)$$

$$APE(z) = \frac{1}{2} \left(A_{\xi}^{SD}(z) \right)^2 \langle N^2(z) \rangle \quad (4)$$

where ξ represents isopycnal displacements and N the buoyancy frequency.

3.2.3 Energy Flux Uncertainty Part 1: Overview

The main source of uncertainty, or why the $F_E^{SD}(z)$ expression in (1a, b) applied to our data might not yield the true energy flux of the semidiurnal internal tide, is related

to the question of whether our sampling patterns are appropriate to adequately capture the semidiurnal variability of the ocean. Nash et al. (2005) examined similar data sets with coarse temporal sampling of a semidiurnal internal tide plus a typical background internal wave spectrum (Garrett and Munk, 1979) and determined that the “minimal strategy” of four profiles within 12 hours effectively captures the semidiurnal energy flux. Our situation is somewhat less favorable due to relatively weak semidiurnal signals, sampling over multiple days (adding uncertainty due to aliasing of low-frequency variability) and the presence of unresolved diurnal variability. Nevertheless, we have attempted to assess all likely causes of error and their implications for our conclusions. In addition to cataloging the various possible error sources, two empirical methods have been employed—one using the statistics of the harmonic fits and the other using subsampling from the highly-resolved *FLIP* timeseries. The *FLIP* method gives the largest, and therefore most representative, uncertainty and will be presented in Section 3.2.4.

Potential error sources include (i) instrumental random error, (ii) aliasing of high-frequency internal wave signals into the semidiurnal fits, (iii) advection of steady horizontal density or velocity gradients by the semidiurnal barotropic tide producing spurious baroclinic semidiurnal signals, (iv) systematic differences among the instruments where data from the XCP, LADCP and the VMP are combined, (v) contributions from the non-linear terms in energy flux which are not included in (1a, b) (Moum et al., 2006), (vi) aliasing by low-frequency velocity and density variability, and (vii) actual low-frequency variability in the internal tide as evidenced in the *FLIP* timeseries (Figs. 4 and 5c), causing results from a short-term survey to differ significantly from the long-term mean,

Some of these error sources (i, ii, vi) are best considered in aggregate through the empirical evaluation of random errors below, while others (iii, iv, v, vii) may contribute biases to the station or average results. Mean gradients across the box (iii) have been estimated and were too small to give significant energy flux error (given the small speeds of the barotropic tide). Differences among instruments (iv) based on typical instrument accuracies of 1-2 cm s⁻¹ are approximately five times smaller than the signal of the internal tide and systematic effects have not been found. In general, the average flux magnitude of about 500 W m⁻¹ (Fig. 2) is relatively weak compared to the O(10,000 W m⁻¹) near major internal tide generation sites such as the Hawaiian Ridge (Lee et al., 2006; Rudnick et al., 2003) and Mendocino Escarpment (Althaus et al., 2003). One advantage of this weak signal is that the likelihood of non-linear effects (v) is reduced. However, the disadvantage is increased difficulty of separating the signal from the noise, which is likely to be comparable in magnitude to the other sites mentioned. Finally, temporal variability of the energy flux (vii) is a subject for interpretation and will be explored later.

In order to establish that the observed spatial variability (described in Sections 3.3.3–3.3.6 below) is not simply a result of random sampling errors (including factors i, ii, and vi above), we estimate uncertainty in two ways. The first, described below, is based on the harmonic fits alone. The second, described in Section 3.2.4, is based on the *FLIP* timeseries and accounts for both the goodness of fit and the neglect of the diurnal cycle.

Standard errors in the semidiurnal velocity and pressure amplitudes and phases can be estimated from the goodness of fit (percentage of explained variance) of the

harmonic regression (Eq. 2; Fig. 5a, b). These have been calculated and propagated through the energy-flux equation (Eq. 1a). Fifteen degrees of freedom were assumed in the vertical integration, based on the de-correlation length scale of the energy flux. Resulting uncertainty varies from station to station due to the unique sampling intervals at each station. Stations with more than 5 profiles (B5, B6, B9 and SB) have the smallest uncertainties (at the 95% confidence level) from the regression, with a magnitude of about $\pm 60 \text{ W m}^{-1}$, while other stations with only four profiles have a mean uncertainty of about $\pm 120 \text{ W m}^{-1}$. However, since these uncertainties are smaller, less complete (due to the neglect of the diurnal cycle), and are already accounted for in the *FLIP*-based estimates (Section 3.2.4), we treat the *FLIP*-based estimates as more representative.

3.2.4 The Subsampling Method

Although the dates of *FLIP* and the XCP box sampling did not overlap (Fig. 4), the well-resolved *FLIP* timeseries can be utilized to estimate uncertainties associated with our sampling, assuming stationary statistics of the internal wave field. “True” and “subsampled” depth-integrated energy fluxes are computed for each point in the 45-min resolution *FLIP* timeseries. The “true” flux is computed from semidiurnal (again, the M_2 period is indistinguishable from S_2) harmonic fits to velocity and pressure over a 48-hour window (at stations B5 and B6, a 72-hour window is used since data was collected over longer than 48 hours, although using a 72-hour window for all the stations yields very similar results). The “subsampled” flux is computed by sampling velocity and pressure from the *FLIP* timeseries using the temporal sampling pattern for each stations (e.g., Fig.

5a and b) and fitting semidiurnal sinusoids to these sparsely-sampled timeseries. This process is repeated at every box station using the sampling intervals unique to that station. This difference-timeseries, defined as difference between the “true” and subsampled time-series (Fig. 5c), is then treated as a statistical distribution from which 95% confidence limits are approximated by twice the standard deviation. (error ellipses) Uncertainties are similar among stations (ellipses in Fig. 2) with average uncertainties of approximately $\pm 200 \text{ W m}^{-1}$, with a mean of 121 W m^{-1} in the east/west component and 171 W m^{-1} in the north/south component. Since, as mentioned above in Section 3.2.1, stations B5, B6, and B9 have additional velocity and/or pressure measurements, alternative subsampling errors were also computed with sampling comparable to the other stations (magenta ellipses in Fig. 2).

The most obvious result of the subsampling is that there is a diurnal cycle to the difference-timeseries. Frequency spectra of the difference-timeseries show a peak at the O_1 frequency ($\omega_{O_1} = 6.76 \times 10^{-5} \text{ rad s}^{-1}$), with a phase offset of about 180° from the TPXO barotropic northward O_1 velocity. Based on this phase shift, and the phase of the barotropic O_1 velocity during the time of the survey-box measurements, the subsampling will over-estimate energy flux by up to 100 W m^{-1} . All XCP and LADCP profiles were obtained during daytime (so during the same half of the diurnal cycle), and therefore all have a similar bias. A more accurate average might be obtained by subtracting this value from the vectors in Fig. 2 based on the expected northward propagation of coastally-trapped waves. However, the predictive ability of the systematic bias is limited. Removing the diurnal cycle of the error only reduces the error variance by about 20% (Fig. 5d), because day-to-day variability exceeds repeatable diurnal contamination. As a

result, we have chosen to treat all of error estimated from subsampling of the *FLIP* timeseries (and displayed in the Fig. 2 ellipses) as random.

3.3. Results

3.3.1 Barotropic Tide

The observed semidiurnal barotropic tide (estimated from sinusoidal fits to the depth-averaged velocity at each station, after adjusting the baroclinic XCP profiles to match shipboard ADCP velocities in the upper water column) had a major-axis amplitude of 2 cm s^{-1} and an orientation to the north-northwest, agreeing to within $\pm 0.5 \text{ cm s}^{-1}$ with the sum of the four semidiurnal constituents of the TPXO global model of ocean tides at the time of our survey (Egbert et al., 1994; Egbert and Erofeeva, 2002) (Fig. 4). Isolating the M_2 component of the TPXO velocity, as opposed to using all four semidiurnal components, yields a similar north/south barotropic velocity of 2.5 cm s^{-1} . This M_2 component was used to force the SUNTANS model in the latest model runs (Kang and Fringer, 2011). The spatial and temporal behavior of the barotropic tide in the Monterey Bay region has been described by Rosenfeld et al., (2009) and Carter (2010).

3.3.2 Internal Wave Field

The internal wave field in the survey box area is dominated by the semidiurnal baroclinic tide, with the box-mean semidiurnal velocity amplitudes reaching over

10 cm s⁻¹ near the surface, and between 2 and 6 cm s⁻¹ below 100-m depth. Based on the vertical wavenumber shear spectra, the internal wave field is four times more energetic than the typical open-ocean Garrett and Munk (1979) model spectrum of the open ocean. Normal-mode decomposition revealed that pressure was mainly low mode, with over 90% of the variance explained in the first three modes. In contrast, velocity requires 15 modes to explain the same amount of variance. Because pressure is dominantly mode one, so is energy flux (Alford 2003; Hendry, 1975; Nash et al., 2005; Wunsch 1975).

3.3.3 Semidiurnal Energy Flux—Depth Integrals

The average observed depth-integrated semidiurnal energy flux over our 3-day occupation of the survey box was $500 \pm 200 \text{ W m}^{-1}$ to the NNE (Fig. 2). Average values from the SUNTANS model are $200 \pm 30 \text{ W m}^{-1}$ NNE. Measurements from *FLIP* produced an even smaller average flux of $100 \pm 50 \text{ W m}^{-1}$ over its 16-day observation period but reached a maximum of $\sim 400 \text{ W m}^{-1}$ during spring tide when semidiurnal barotropic tide amplitude and phase were comparable to the time of the survey box (Fig. 4).

Despite large uncertainty ellipses (see Section 3.2.4), both the mean flux and spatial variability within the survey box are significant (Fig. 2). Most stations have a northeast flux of $\sim 500 \pm 200 \text{ W m}^{-1}$ and are not significantly different from the mean. Prominent variations within the survey domain are the weaker fluxes at stations B5 and B6 on the south face and southeast corner of the box. The vertical structure of the semidiurnal baroclinic \bar{u} and P (Fig. 6) shows that the flux deviations at B5 and B6 are

mostly due to anomalous pressure phases. Additionally, at B5, the amplitude of the semidiurnal pressure is 50% smaller than at all other stations.

Most of the observed fluxes, except for B5 and B6, are larger in magnitude, but roughly consistent with the flux pattern in the SUNTANS model in which fluxes follow the northward path of the beam. However, the pattern in the model does not explain the weaker fluxes at B5 and B6. The explanation for these weak fluxes, must then be one which highlights the sensitivity of the modeled internal tide to under-resolved physics and /or bathymetry or details in forcing. From the large-scale energy-flux patterns (see, for example, Fig. 8 in Carter, 2010), it appears likely that the eastward energy flux at SB (Fig. 1) originates from internal tide generation at the Sur Ridge, merging with the northward beam from Sur Platform as the beam approaches Monterey Canyon. This superposition of two generation sites suggests that, not only the gross internal wave generation, but also the details of the interference pattern and beam geometry need to be accurately simulated by the model in order to compare with observations. Furthermore, observations need to have finer lateral resolution and broader lateral coverage to capture the interference patterns.

3.3.4 Semidiurnal Energy Flux—Profiles

Examination of the vertical structure of the energy flux provides additional information about the complex nature of the internal tide. Meridional and zonal transects of the northward, eastward and vertical semidiurnal energy-flux profiles indicate both lateral and vertical variability (Fig. 3). The profiles provide evidence that energy from

both local (*i.e.*, within the survey box) and remote sources is present. Local generation is manifested as increased near-bottom vertical energy flux in the profiles. Small-scale bathymetry within the box should only impact the near-bottom energy-flux within an envelope of characteristic ray paths to a height, $h = s\Delta x$, above the bottom. With $\Delta x = 5$

$$\partial z / \partial y = \pm \sqrt{(\omega^2 - f^2) / (N^2 - \omega^2)}$$

km (the survey box width) and ray path slopes $s =$

\approx

0.04 where ω, f , and N are the wave, inertial, and buoyancy frequencies, respectively,

values for h are around 200 meters above the bottom. Energy flux from remote sources

(those outside the survey box) can be identified by maxima in the mid-water column

energy-flux profiles propagating through the box along ray paths. Some example ray

paths have been drawn in Fig. 3 to aid in the identification of potential sources (whether

local or remote). The theoretical ray slope for waves of semidiurnal frequency is similar to

the slope of the large-scale bathymetry of all three transects. However, small-scale

bathymetry differences among the three transects (Figure 3c, d) can cause near-bottom

energy-flux variability. Remote sources can be further subdivided into regional (or

nearby) sources such as Sur Ridge, Sur Platform, Davidson Seamount and Guide

Seamount, or distant sources that might be up to thousands of kilometers away (Zhao et

al., 2010).

Meridional transects (Fig. 3a, c, e) reveal mainly – though not exclusively –

northward-propagating energy, consistent with depth-integrated fluxes. Similarities

among the transects include beam-like features that appear to be generated south of SB

(roughly indicated by the example rays in Fig. 3a, c, e), small fluxes throughout the water

column at stations B5 and B6 (Fig. 3c, e), and alternating bands of west- and eastward

energy flux along the west and center transects (red and black bands in Fig. 3a,c). These alternating bands suggest that remote on- and offshore sources impact our measurements. For the most part, the vertical component of flux is consistent with the expected ray slopes, indicating vertical propagation rather than standing modes.

Zonal fluxes (Fig. 3b, d, f) are less coherent, both among stations and among transects. Most stations tend to show alternating layers of east- and westward energy flux (as mentioned above) and exhibit a mid-depth and near-surface onshore flux (Fig. 3b, d). Additional noticeable features include eastward surface intensification in the northern transect (Fig. 3b), and consistently eastward fluxes at the southeast corner of the survey box (station B5). Though difficult to compare in detail, this zonal flux pattern is more-or-less consistent with the results of Johnston et al. (2011), who found evidence for both onshore (eastward) energy flux associated with the northward beam from the Sur Platform and weaker mode-two offshore flux from the continental shelf break in this region.

3.3.5 Horizontal Kinetic and Available Potential Energy Profiles

Meridional transects of HKE and APE also exhibit both lateral and vertical variability (Fig. 7). Vertical variability in HKE and APE profiles is not consistent with mode-one, affirming the presence of higher modes in velocity; a purely mode-one structure would have surface and bottom maxima for HKE and a mid-depth maximum for APE. Almost all stations show HKE near the surface in excess of that expected purely from the elevated stratification through WKB scaling.

For linear internal waves with frequencies ω much lower than the buoyancy frequency N , the energy ratio $\text{HKE}/\text{APE} = (\omega^2 + f^2) / (\omega^2 - f^2)$. For the M_2 constituent at 36.5°N ($f = 8.7 \times 10^{-5} \text{ rad s}^{-1}$), the theoretical value of HKE/APE is 2.2. Observed ratios computed at each station from vertically integrated HKE and APE range from 0.7 to 2.7. In contrast to the findings of Kunze et al. (2002), subtracting a linear fit (with the only constraint being zero displacement at the surface) to remove the barotropic contribution in the form of excess potential energy from isopycnal displacements, does not bring the observed values closer to the theoretical value. However, if an estimated barotropic displacement, $A_{\xi_{BT}}^{SD} = A_{\bar{u}_{BT}}^{SD} (\bar{\nabla}h)z / \omega h$ (using semidiurnal amplitudes, A of isopycnal displacements, ξ , and barotropic velocity, and the 250-m bathymetry gradient $\bar{\nabla}h$, frequency ω , depth z , and bottom depth h) is removed (Baines, 1982; Nash et al., 2006), the observed energy ratios do a better job of matching the theoretical ratio (Fig. 7). But removing excess APE is not always helpful; some ratios, even after removing ξ_{BT} , fall short of theoretical ratios, while other ratios have no excess APE to begin with. The energy ratio, which is usually – though not always – improved by removing barotropic effects, supports the notion that the survey box is affected by the locally generated internal tides, which heave isopycnals up over bathymetry. Again, there is also evidence for remotely generated internal tides, which propagate through the survey box as beam-like features in the mid-water column (Fig. 3).

The energy ratios in an area dominated by multiple waves rather than a single propagating wave are expected to vary at every location. For a two-wave pattern, ratios range from 0 to ∞ over $1/4$ wavelength (Nash et al., 2006). With additional waves, the length scales of variability could be even shorter.

3.3.6 Data/Model Comparisons and Temporal Variability

SUNTANS and other models cited above were designed to (i) provide insight about the origin and fate of the internal tide and (ii) complement field observations by supplying more complete spatial coverage. The models nevertheless represent simplifications of the natural world and can be expected to deviate in some ways. The overall amplitude difference between modeled and measured fluxes is a puzzle. The Kang and Fringer (2011) SUNTANS model amplitudes used in this comparison are weaker than previously published SUNTANS model runs (Jachec et al., 2006), mainly due to a smaller and more realistic barotropic forcing (Fig. 4). Other improvements in the more recent model runs include a larger domain (the more recent domain extends approximately 200 km offshore to include both Davidson Seamount and Guide Seamount), an initial stratification based on our observations, improved boundary conditions to reduce the reflection of barotropic energy, and longer simulation times. Ironically, the improved model agrees less well with most of our observations. The amplitude of the observed and modeled barotropic tide was comparable, even though the model only uses the M_2 constituent.

The barotropic and locally-forced baroclinic tide should, to certain extent, co-vary with the barotropic tide with a time delay between barotropic forcing and baroclinic response due to propagation time. In addition to forcing by the local barotropic tide, part of the baroclinic tide is forced by remotely generated shoaling internal tides as described in Kelly and Nash (2010a). Differences in remotely generated tides resulting from model domain limitations could be responsible for model / data discrepancies. The *FLIP*

timeseries can be used to examine the extent to which local semidiurnal barotropic forcing influences semidiurnal energy flux. While the maximum in energy flux does correspond to a maximum forcing, the energy flux timeseries exhibits substantially more variability than the barotropic tide implying that shoaling tides are important for internal tide generation here (Fig. 4).

In order for the data and model to agree, the model domain must be large enough to encompass all sources, both remote and local, which is not necessarily the case. Low-mode internal tides can travel thousands of kilometers from their generation sites (Dushaw, 2002; Ray and Cartwright, 2001; Zhao et al., 2010). The SUNTANS model run-time was long enough (12 days) that mode-one tidal energy (with a group speed of $\sim 1.6 \text{ m s}^{-1}$) from regional remote sources will reach the survey box, but modes higher than five, as were evident in the observations, will not. The domain size and remote sources are important in terms of preconditioning the generation environment, as illustrated in a numerical model study by Hall and Carter (2011) in which reducing the model domain to exclude remote sources with high rates of barotropic-to-baroclinic conversion (Davidson Seamount, Guide Seamount and the shelf slope north of Monterey Bay Submarine Canyon) reduced the depth-integrated energy flux in the canyon by 20%. This decrease was due, not only to the loss of incoming energy, but also to changes in local generation (Hall and Carter 2011; Kelly and Nash 2010a).

In addition to the limitations of the finite model domain and duration of the model run other potential sources of discrepancies are (i) differences in tidal forcing (model M_2 only versus all constituents in the ocean), (ii) differences in ocean and model bathymetry, (iii) modulation of semidiurnal tide by differences in our observations since

measurements were collected over the same phase of the O_1 cycle as discussed in Section 3.2.4) and or initial stratification, and (iv) lateral stratification variations and sub-inertial shear modifying the generation and propagation of internal tides in the real ocean.

The model appears to resolve local and regional topographic features (Fig. 3c, d, cyan dotted line). Tidal forcing and initial stratification are similarly reasonable. It is not known, however, how sensitive the models are to errors in these quantities. For example, the barotropic tidal flow at the Sur Ridge is nearly parallel to the topography, so a small error in tidal current direction could potentially produce a large shift in the generated internal tides. The influence of very small-scale topography and lateral variations in the sub-tidal fields are also potentially important, but seem less likely to produce the major model/observation discrepancies described here as their influence will principally be on high modes that contribute little to the energy-flux magnitude.

3.4. Discussion

The underlying source of lateral variability in the depth-integrated semidiurnal energy flux—observed primarily at the southeast stations B5 and B6—is a change in semidiurnal pressure phase (section 3.3.3, Fig. 6). While this accounts for the term in (1a, b) where the anomalous energy fluxes originate, this mathematical explanation lacks insight into the dynamical cause of variability. A possible explanation is that the survey box area is situated in a complex internal wave field affected by both locally and remotely generated internal tides. Constructive and destructive interference patterns due to the superposition of waves from a number of sources can make in situ point

measurements difficult to interpret, significantly modifying the direction and magnitude of the fluxes (Martini et al, 2007). The numerical model study at the Hawaiian Ridge (Rainville et al., 2010) was able to re-create significant features in the horizontal structure of the M_2 depth-integrated energy flux using idealized radially-spreading waves of limited azimuthal extent from the four main generation sites. This suggests that, at least in some cases, complex patterns are reproducible by interference.

We construct a similar interference pattern model consisting of mode-one semidiurnal internal waves beams of limited azimuthal extent to recreate small-scale variability of energy flux on the central California continental margin (Fig. 8). As shown by Carter (2010), the area surrounding our survey box has multiple sites with comparable rates ($> 0.1 \text{ W m}^{-2}$) of barotropic-to-baroclinic conversion including Sur Platform, Sur Ridge, Davidson Seamount and Guide Seamount (Fig. 1b). Our survey box is likely to be affected by at least the first two of these. Two example interference patterns have been constructed to attempt to explain our observations—one with two sources, Sur Ridge ($\sim 150\text{-km}$ southwest of the survey box) and Sur Platform ($\sim 50\text{-km}$ south of the survey box) (Fig. 8a) and another adding a third source of offshore flux from the shelf break (Fig. 8b). Adding the third source is justified by offshore flux in our observations (Fig. 3b), as well as the mode-2 results of Johnston et al (2011). This produces an even more complicated field, with energy-flux variations on $O(5 \text{ km})$ spatial scales.

General properties of the depth-integrated energy flux patterns formed by two line sources are:

1. Bands of maximum and minimum energy are separated by $\sim 1/4$ the wavelength of the original waves (assuming they have the same wavelength) along the axis connecting the two sources.
2. Off-axis, the energy bands become wider and bend toward the nearer source.
3. At some locations in the interference pattern, the flux may be in the opposite direction as the sum of the two individual sources.
4. A spatial average over this interference pattern is needed to derive a flux that equals the sum of the individual sources but, since the length-scales increase with distance, this becomes increasingly difficult to accomplish.

At least three-waves are required to create an interference pattern which reduces the spatial scale of variability enough to account for the abrupt change in magnitudes seen at the southeast stations B5 and B6, unless B5 and B6. A two-wave interference pattern can result in abrupt changes in flux at beam edges where some stations are affected by waves generated at both Sur Ridge and Sur Platform and the rest of the stations are affected only by the beam from Sur Platform. An example of this is shown by the gray box in Fig. 8a.

Both multi-wave interference patterns and beam edges can cause variability though not divergence, which is implied by the observed fluxes (Fig. 2). While the observed divergence may simply be a result of aliased sampling of a complicated non-divergent field, the prevalent near-critical ($2-4^\circ$ slope) bathymetry around the box, as well as sharper features such as the thin ridge just north of B5 and B6, may radiate

internal tides or reflect and scatter incident waves. As mentioned previously (Sec.3.4), these local bathymetric effects should be restricted to the lower part of the water column ($h = z - H < 200$ mab). Although near-bottom fluxes do contribute significantly to the depth-integral at many of the stations, the generally downward vertical flux (Fig. 3) suggests that local generation or scattering within the box is not the dominant process. A superposition of two or more analytic waves is divergence-free in the limit of infinitesimal resolution so the observed divergence is likely caused by finite-resolution central differencing associated with the 2.5-km spacing of the survey-box. Limited spatial resolution may also cause spurious divergences at beam edges. Baroclinic to barotropic energy conversion may account for some (though not all) of the observed flux divergence.

3.5. Conclusions

It is important to note that even with uncertainties of $\sim 40\%$, differences between stations are still significant. Although we cannot entirely separate the influences of locally- and remotely-generated waves, or capture the full structure of the internal tide interference pattern, our measurements do underscore some important points about observations of the internal tide on the California continental margin south of Monterey Bay region:

- Lateral variability can be found on scales smaller than expected, $O(5$ km).

Spatial scales normally assumed adequate to resolve mode-one internal tide may not be sufficient to capture variability in areas near rough topography or with

complicated internal wave fields where interference patterns from multiple sources need to be considered (Rainville et al., 2010; Martini et al., 2007). If only one or two of the nine stations focused on here were used to quantify the semidiurnal energy flux for the entire sampling area, incorrect or incomplete conclusions would be inferred.

- Measurements aimed at isolating the semidiurnal tide in a region influenced by diurnal coastally-trapped baroclinic waves tide should be taken over a period of at least 24 consecutive hours to eliminate aliasing.
- Based on a simple interference-pattern model, there are two ways in which the spatial scale of variability can be reduced to $O(5 \text{ km})$, the scale on which we observed significant variability: (i) adding a third source of internal tide or (ii) measuring at the edge of a beam with finite azimuthal extent. More complicated models, such as the one run in Carter (2010), have found beams, likely caused by interference patterns, to have widths between 2 and 10 km.
- Internal tide generation models containing a reasonably accurate depiction of complex bathymetry may still underestimate the spatial complexity of the internal tide. Possible reasons include (i) spatial variations in stratification and sub-inertial current which can influence both internal tide generation and propagation, (ii) not being run long enough for high modes to fill the domain, and (iii) finite domain size and omission of distant generation sites. In addition, temporal variations in stratification due to the spring–neap tidal cycle, wind forcing or other low-frequency processes can, through fairly minor changes in internal tide generation and propagation characteristics (particularly phase), lead to vastly different details

in the pressure, velocity and energy flux interference patterns from distant sources
(Hall and Carter, 2010; Kelly and Nash, 2010a).

3.6 Acknowledgments

We thank Dajuan Kang and Oliver Fringer for providing the SUNTANS model output. The Office of Naval Research funded this project under grant numbers N00014-05-1-0332 and N00014-08-1-0983. The captain and crew of the *R/V Pt. Sur* were essential for gathering the data. Helpful comments and insights were provided by Tom Sanford, Matthew Alford and Luc Rainville and anonymous reviewer 1.

3.7 Bibliography

- Alford, M.H., 2003. Redistribution of the energy available for ocean mixing by long-range propagation of internal waves. *Nature* 423, 159-162.
- Alford, M.H., MacKinnon, J.A., Zhao, Z., Pinkel, R., Klymak, J., Peacock, T., 2007. Internal waves across the Pacific. *Geophys. Res. Lett.* 34, L24601.
- Althaus, A.M., Kunze, E., Sanford, T. B., 2003. Internal tide radiation from the Mendocino Escarpment. *J. Phys. Oceanogr.* 33, 1510-1527.
- Baines, P.G., 1982. On internal tide generation models. *Deep Sea Res.* 29, 307-338.
- Bell, T.H., 1975. Topographically generated internal waves in the open ocean. *J. Geophys. Res.* 80, 320-327.
- Carter, G.S., Gregg, M.C., 2002. Intense, variable mixing near the head on Monterey Submarine Canyon. *J. Phys. Oceanogr.* 32, 3145-3165.
- Carter, G.S., Merrifield, M.A., Becker, J.M., Katsumata, K., Gregg, M.C., Luther, D.S., Levine, M.D., Boyd, T.J., Firing, Y.L., 2008: Energetics of M_2 barotropic to baroclinic tidal conversion at the Hawaiian Islands. *J. Phys. Oceanogr.* 38, 2205-2223.
- Carter, G.S., 2010. Barotropic and Baroclinic M_2 Tides in the Monterey Bay Region. *J. Phys. Oceanogr.* 2010, 1766-1783.
- Dushaw, B.D., 2002. Mapping low-mode internal tides near Hawaii using TOPEX/POSEIDON altimeter data. *Geophys. Res. Lett.* 29, 1250, doi:10.1029/2001GL013944
- Egbert, G.D., Bennett, A.F, Foreman, M.G.G., 1994. TOPEX/POSEIDON tides estimated using a global inverse model, *J. Geophys. Res.* 99, 24,821–24,852.
- Egbert G.D., Ray, R.D., 2001. Estimates of M_2 tidal energy dissipation from TOPEX/Poseidon altimeter data. *J. Geophys. Res.* 106, 22,475-22,502.
- Egbert G.D., Erofeeva S.Y., 2002. Efficient inverse modeling of barotropic ocean tides. *J. Atmos. Ocean. Technol.* 19, 183-204.
- Garrett, C., Munk, W., 1979. Internal waves in the ocean. *Annu. Rev. Fluid Mech.* 11, 339-369.
- Garrett, C., Kunze, E., 2007. Internal tide generation in the deep ocean. *Annu. Rev. Fluid Mech.* 39, 57-87.

- Hall, R.A., Carter, G.S., 2011. Internal tides in Monterey Submarine Canyon. *J. Phys. Oceanogr.* 41, 186-204.
- Hazewinkel, J., Winters, K.B., 2011. PSI of the internal tide on a β plane: Flux divergence and near-inertial wave propagation. *J. Phys. Oceanogr.* 41, 1673–1682.
- Hendry, R.M., 1975. The generation, energetics and propagation of internal tides in the western North Atlantic Ocean. Doctoral Thesis. Woods Hole Oceanographic Institution, Woods Hole, MA.
- Jachec, S.M., Fringer, O.B., Gerritsen, M.G., Street, R.L., 2006. Numerical simulation of internal tides and the resulting energetics within Monterey Bay and the surrounding area. *Geophys. Res. Lett.* L12605.
- Johnston, T.M.S., Rudnick, D.L., Carter, G.S., Todd, R.E., Cole, S.T., 2011. Internal tidal beams and mixing near Monterey Bay. *J. Geophys. Res.* 116, C03017.
- Kang, D., and Fringer, O., 2011. Energetics of barotropic and baroclinic tides in the Monterey Bay area. *J. Phys. Oceanogr.*, in press.
- Kelly, S.M. and Nash, J.D., 2010a. Internal-tide generation and destruction by shoaling internal tides. *Geophys. Res. Lett.* 37, L23611.
- Kelly, S.M., Nash, J.D., Kunze, E. 2010b. Internal-tide energy over topography. *J. Geophys. Res.* 115, C06014.
- Klymak, J.M., Moum, J.N., Nash, J.D., Kunze, E., Girton, J.B., Carter, G.S., Lee, C.M., Sanford, T.B., Gregg, M.C., 2006. An Estimate of Tidal Energy Lost to Turbulence at the Hawaiian Ridge. *J. Phys. Oceanogr.*, 36, 1148–1164.
- Kunze, E., Rosenfeld, L.K., Carter, G.S., Gregg, M.C., 2002. Internal waves in Monterey Submarine Canyon. *J. Phys. Oceanogr.* 32, 1890–1913.
- Kunze, E., MacKay, C., McPhee-Shaw, E.E., Morrice, K., Girton, J.B., Terker, S.R. 2011. Turbulent mixing and exchange with interior waters on sloping boundaries. Submitted to *J. Phys. Oceanogr.*
- Lee, C.M., Kunze, E., Sanford, T.B., Nash, J.D., Merrifield, M.A., Holloway, P.E., 2006. Internal tides and turbulence along the 3000-m isobath of the Hawaiian Ridge. *J. Phys. Oceanogr.* 36, 1165-1183.
- Lien, R.-C., Tang, T.Y., Chang, M.H., D'Asaro, E.A., 2005. Energy of nonlinear internal waves in the South China Sea. *Geophys. Res. Lett.* 32, L05615.

- MacKinnon, J.A., Winters, K.B., 2005. Subtropical catastrophe: significant loss of low-mode tidal energy at 28.9 degrees, *Geophys. Res. Lett.* 32, L15605.
- Martini, K.I., Alford, M.H., Nash, J.D., Kunze, E., Merrifield, M.A., 2007. Diagnosing a partly standing internal wave in Mamala Bay, Oahu, *Geophys. Res. Lett.* 34, L17604.
- McComas, C.H., Müller, P., 1981a. The dynamic balance of internal waves. *J. Phys. Oceanogr.* 11, 970–986.
- McComas, C.H., Müller, P., 1981b. Time scales of resonant interactions among oceanic internal waves. *J. Phys. Oceanogr.* 11, 139–147.
- Moum, J.N., Caldwell, D.R., Nash, J.D., Gundersen, G.D., 2002. Observations of boundary mixing over the continental slope, *J. Phys. Oceanogr.*, 32, 2113-2130.
- Moum, J.N., Klymak, J.M., Nash, J.D., Perlin, A., Smyth, W.D., 2006. Energy transport by nonlinear waves. *J. Phys. Oceanogr.* 37, 1968-1988.
- Nash, J.D., Kunze, E., Toole, J.M., Schmitt, R.W., 2004. Internal tide reflection and turbulent mixing on the continental slope. *J. Phys. Oceanogr.* 34, 1117-1134.
- Nash, J.D., Alford, M.H., Kunze, E., 2005. Estimating internal wave energy fluxes in the ocean. *J. Atmos. Oceanic Technol.* 22, 1551-1570.
- Nash, J.D., Kunze, E., Lee, C.B., Sanford, T.B., 2006. Structure of the baroclinic tide generated at Kaena Ridge, Hawaii. *J. Phys. Oceanogr.* 36, 1123-1135.
- Nash, J.D., Alford, M.H., Kunze, E., Martini, K., Kelly, S., 2007. Hotspots of deep ocean mixing on the Oregon continental slope. *Geophys. Res. Lett.* 34, L01605.
- New, A.L., 1988. Internal tidal mixing in the Bay of Biscay. *Deep Sea Res.* 35, 691-709.
- Nycander, J., 2005. Generation of internal waves in the deep ocean by tides. *J. Geophys. Res.* 110, C10028, doi:10.1029/2004JC002487
- Park, J., Watts, D.R., 2006. Internal tides in the Japan Sea. *J. Phys. Oceanogr.* 36, 22–34.
- Petruncio, E.T., Rosenfeld, L.K., Paduan, J.D., 1998. Observations of the internal tide in Monterey Canyon. *J. Phys. Oceanogr.* 28, 1873-1903.
- Rainville, L., Pinkel, R., 2006. Propagation of Low-Mode Internal Waves Through the Ocean. *J. Phys. Oceanogr.* 36, 1220-1237.

- Rainville, L., Johnston, S.T.M., Carter, G.S., Merrifield, M.A., Pinkel, R., Worcester, P.F., Dushaw, B.D., 2010. Interference pattern and propagation of the M_2 internal tide south of the Hawaiian Ridge. *J. Phys. Oceanogr.*, 40, 311–325.
- Ray, R.D., Mitchum, G.T., 1996. Surface manifestation of internal tides generated near Hawaii. *Geophys. Res. Lett.*, 23, 2101–2104.
- Ray, R., Cartwright, D., 2001. Estimates of internal tide energy fluxes from Topex/Poseidon altimetry: Central North Pacific. *Geophys. Res. Lett.* 28, 1259-1262.
- Rosenfeld, L.K., Paduan, J.D., Petrucio, E.T., Goncalves, J.E., 1999. Numerical simulations and observations of the internal tide in a submarine canyon, *Dynamics of Oceanic Internal Gravity Waves, II* (Eds. P. Müller and D. Henderson), Proc. Aha Huliko'a Hawaiian Winter Workshop, pp. 63-72.
- Rosenfeld, L., Shulman, I., Cook, M., Paduan, J., Shulman, C., 2009. Methodology for a regional tidal model evaluation, with application to central California. *Deep Sea Res. Part II*, 56, 199-218.
- Rudnick, D.L., Boyd, T.J., Brainard, R.E., Carter, G.S., Egbert, G.D., Gregg, M.C., et al., 2003. From tides to mixing along the Hawaiian Ridge. *Science* 301, 355-357.
- Simmons, H., Hallberg, R., Arbic, B., 2004. Internal wave generation in a global baroclinic tide model. *Deep Sea Res. Part II*, 3043-3068.
- St. Laurent, L. and C. Garrett. 2002. The role of internal tides in mixing the deep ocean. *J. Phys. Oceanogr.* 32, 2882-2899.
- Wang, X., Chao, Y., Dong, C., Farrara, J., Li, Z., McWilliams, J.C., Paduan, J.D., Rosenfeld, L.K., 2009. Modeling tides in Monterey Bay, California. *Deep Sea Res. Part II*. 56, 219-231.
- Wunsch, 1975. Internal tides in the ocean. *Rev. Geophys.* 13, 167-182.
- Zhao, Z., Alford, M.H., MacKinnon, J.A., Pinkel, R., 2010. Long-Range propagation of the semidiurnal internal tide from the Hawaiian Ridge. *J. Phys. Oceanogr.* 40, 713-736.

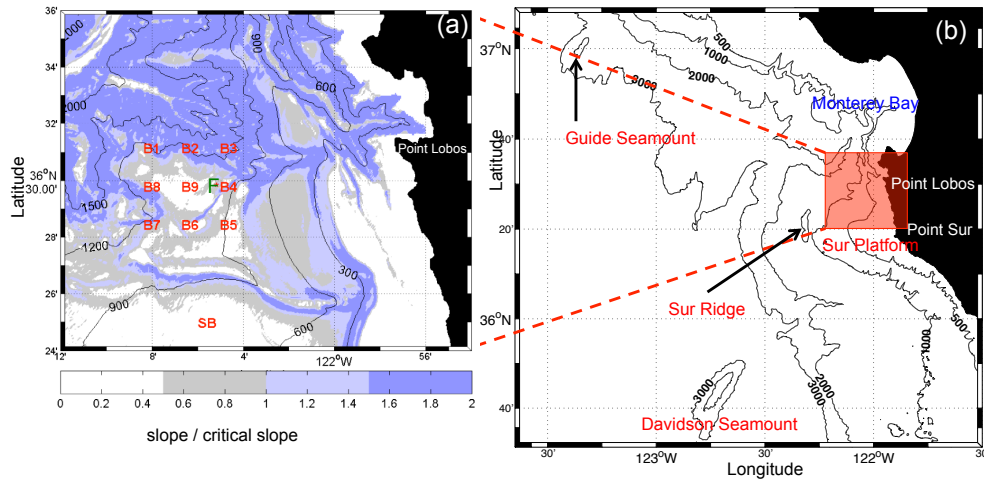


Figure 1. (a) Overview of experiment site and station locations. Station names, B1 – B9 (the survey box) and SB are centered on the position of each respective station. The *FLIP* location is denoted by a green F. Bathymetry at 300-m intervals is contoured with black lines and the bathymetric-to-critical slope ratio for the semidiurnal internal tide is indicated by the color shading (color bar). (b) A more extensive diagram of the region surrounding the survey-box (red square) including likely internal tide generation sites (red text). Bathymetry is contoured with black lines at 500-, 1000-, 2000- and 3000-m depths.

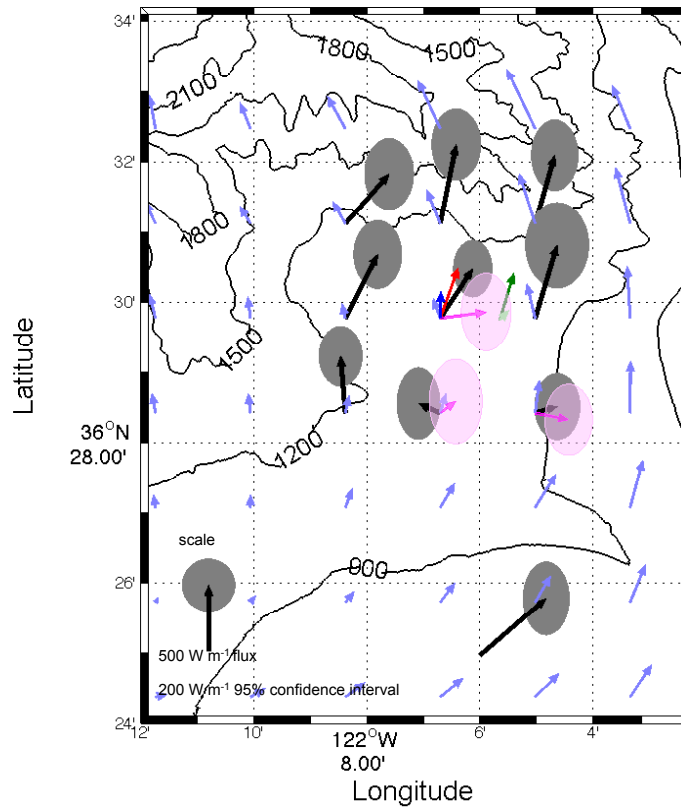


Figure 2. Depth-integrated semidiurnal energy-fluxes from (i) the box-survey stations using all available data (thick black arrows), (ii) box-survey-average (red), (iii) station B5, B6 and B9 using only four or five XCP profiles (no additional XCP timeseries, LADCP profiles or VMP nighttime profiles are included) [magenta] (iv) the SUNTANS M_2 -forced model (light blue), (v) the (spatial) mean from the model (dark blue), (vi) the maximum from *FLIP* (dark green) and (vii) the time-mean from *FLIP* (light green). Confidence intervals (95%) are shown as gray or light magenta ellipses around the tip of observed energy flux vectors. A reference flux arrow and uncertainty ellipse is plotted in the bottom left. Bathymetry is contoured in 300-m intervals.

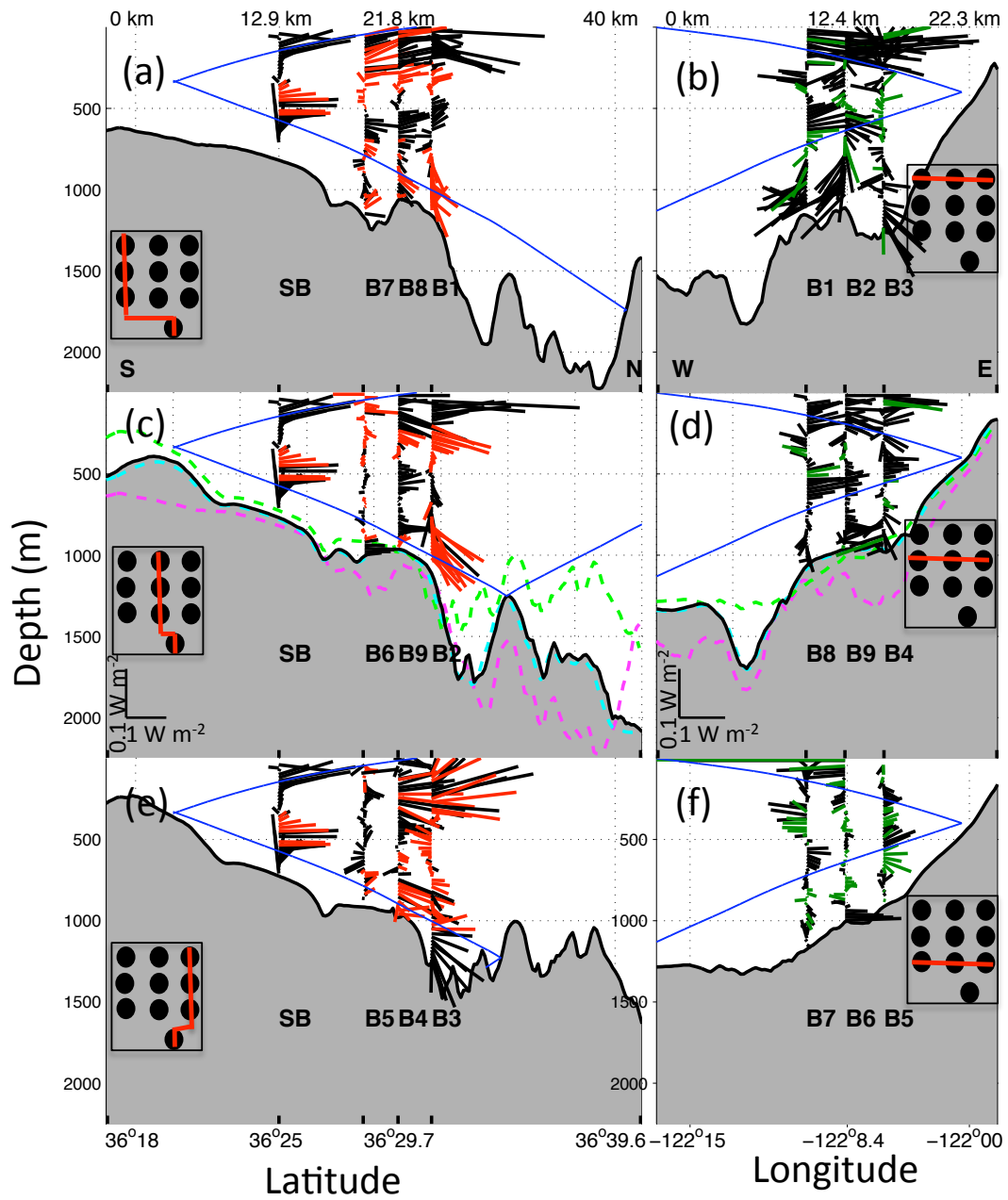


Figure 3. Meridional and zonal sections of semidiurnal energy flux. The magnitude and direction of the vectors are composed of the northward and vertical component of flux along the west (a), center (c) and east (e) transects of the survey box, while the color only reflects the direction but not magnitude of east (black) and west (red) components. Similarly, the magnitude and direction of eastward and vertical components of flux are

plotted along the north (b), center (d) and south (f) transects of the survey-box, while the color reflects the north (black) and south (green) components. Each panel contains an overhead view of the survey-box with the respective transect denoted by a red line. Semidiurnal ray paths are plotted in blue. Gray-shaded bathymetry is from MBARI 50-m high-resolution data from a multibeam survey and the light-blue dashed line in each of the center panels shows bathymetry used by the SUNTANS model (Jachec et al., 2006). The center panels also include bathymetry from the north-south transects on the west (dashed magenta) and east (dashed green) sides of the survey box, and the east-west transects on the north (magenta) and south (green) sides. Station numbers are below the corresponding profile. Distances from the southmost and westmost of the transect are shown on the top and latitude/longitude on the bottom.

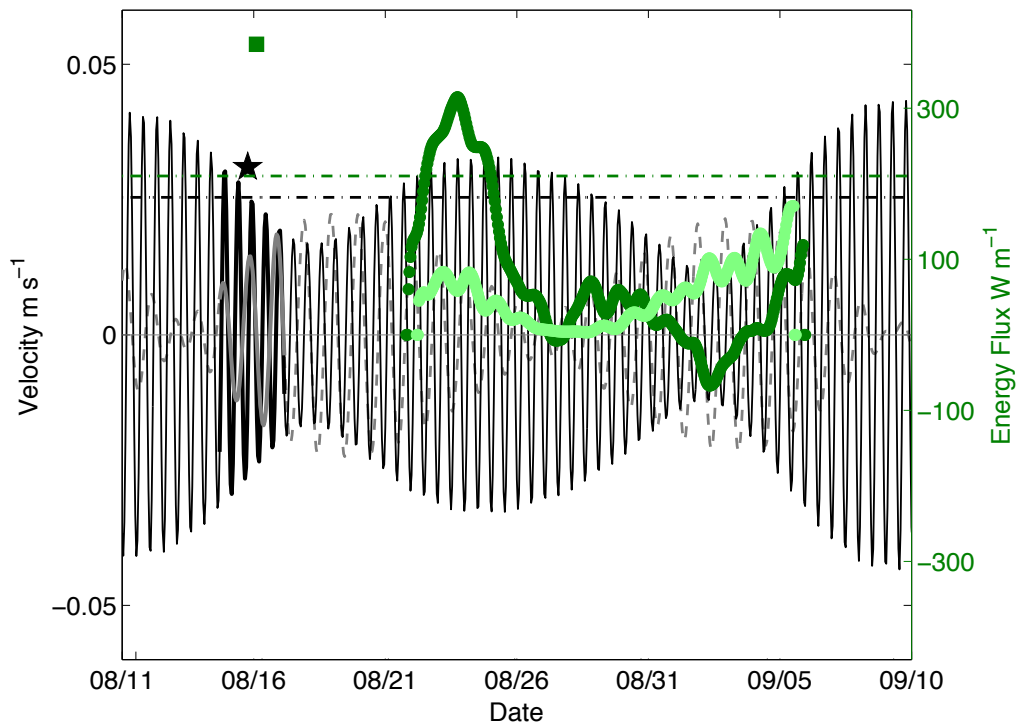


Figure 4. Barotropic velocities and depth-integrated energy fluxes are plotted. The left y-axis is velocity and corresponding quantities are plotted in shades of black. These include timeseries of north semidiurnal and diurnal barotropic velocities from TPXO (thin solid black and gray dashed respectively corresponding to left axis; thick solid during survey box sampling), average north barotropic velocity amplitude during the survey (black star) and the M_2 -only value from TPXO which is used to force the SUNTANS model (black dashed horizontal line). The right y-axis is depth-integrated energy flux and corresponding quantities are plotted in shades of green. These quantities include semidiurnal and diurnal depth-integrated energy fluxes from *FLIP* (green and light green filled dots respectively), the mean semidiurnal depth-integrated flux from the box survey (green square) and the mean (averaged over the area shown in Fig. 2) model flux (green dashed horizontal line). TPXO data is from the TPXO global model of ocean tides that

finds a best-fit solution to the Laplace tidal equations based on satellite altimetry data and tide gauge data (Egbert et al., 1994; Egbert and Erofeeva 2002). Note that the relative scaling of the velocity (black) and flux (green) axes has been chosen purely for ease of comparison.

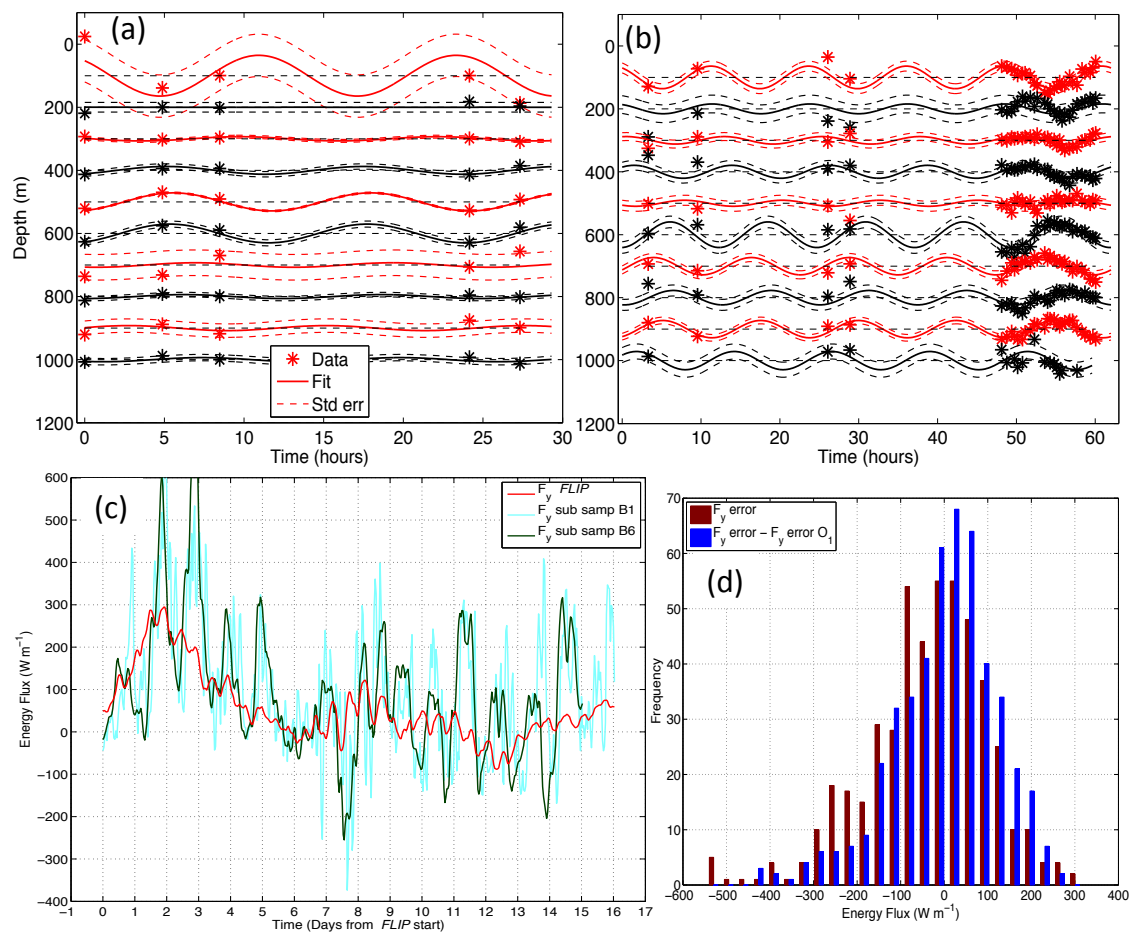


Figure 5. Error analysis for the box-survey energy-fluxes includes examination of harmonic fits(a, b), use of the subsampling method from Section 3.2.3 (c), and diurnal contamination of the semidiurnal signal (d). The goodness of the harmonic fits are shown for station B1 (a) and B6 (b) where measured baroclinic velocity (denoted *) [where 300-m in depth is $1 m s^{-1}$] is plotted at depth intervals of 100-m (alternating red and black)

along with the M_2 fit (solid) and its standard error (dashed). Sampling at most stations are similar to B1, with five profiles over 36 hours with a 12-hour gap. Station B6 is augmented with a 12-h XCP time-series sampled every half-hour. (c) Comparing un-sampled or “true” (red) and subsampled time-series (light blue is based on sampling at B1 and dark green on B6) of depth-integrated meridional semidiurnal energy flux ($F_y FLIP$) show errors (F_y error) caused by the temporal sampling. There is a diurnal component to F_y error (the difference between the red and either the light blue or dark green curves) at both B1 and B6. (d) Histograms of the error (shown for station B6 but similar for other stations) with (red) and without (blue) this diurnal component removed (blue and red respectively) illustrate that removing the diurnal component does little to reduce the variability.

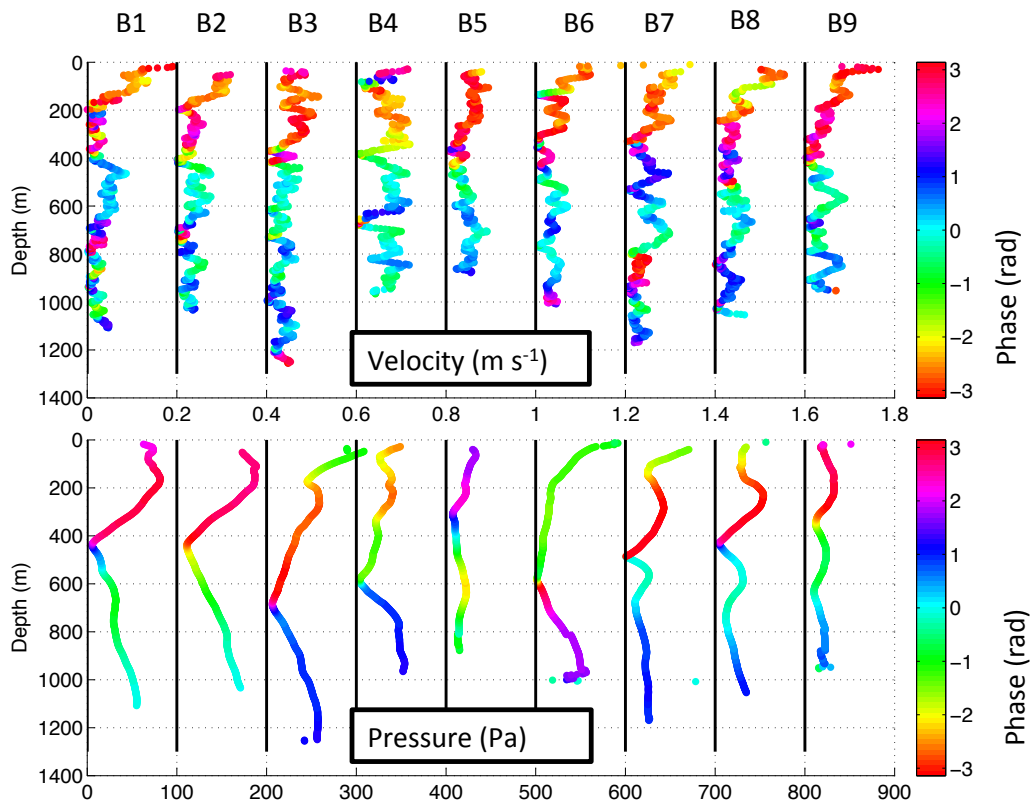


Figure 6. Amplitude and phase of north/south semidiurnal velocity (upper) and pressure (lower). Amplitudes are plotted with phase indicated by the colorbar. Each station has a black line at its zero, and stations are separated by 0.2 m s⁻¹ and 100 Pa. Station numbers are listed above the respective profiles. While velocity phase is uniform across the box-survey stations, pressure phase is anomalous at B5 and B6 at the southeast corner.

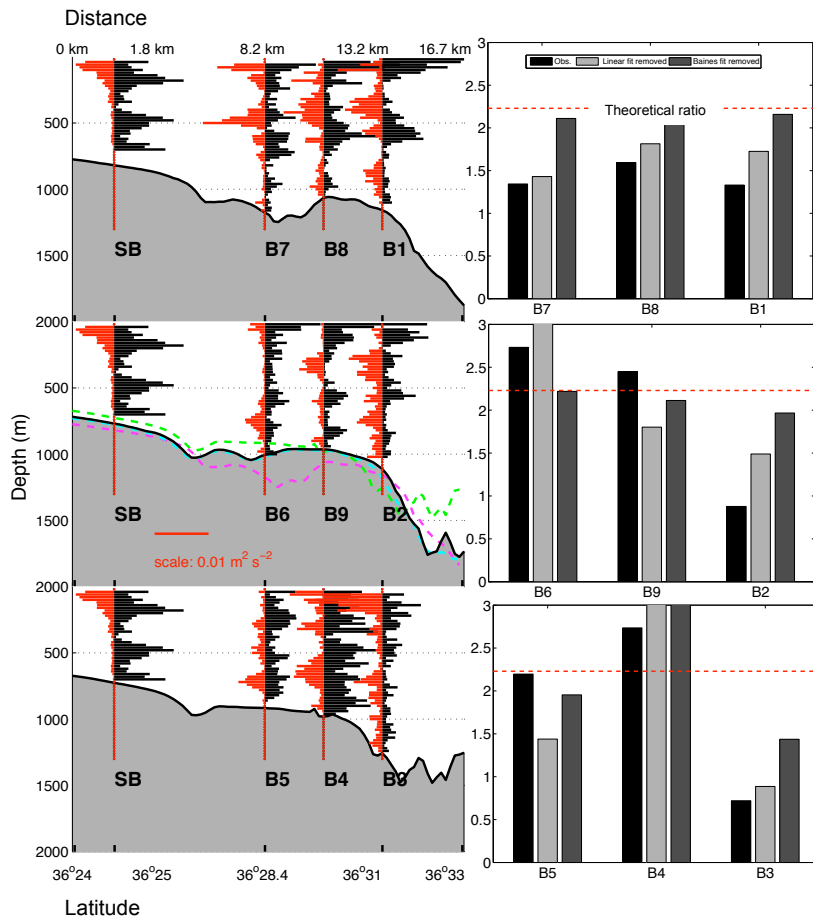


Figure 7. (left panels) HKE (black) and APE (red) profiles at each station along meridional transects, similar to Fig. 6. (right panels) Station-average energy ratios $\langle \text{HKE} \rangle / \langle \text{APE} \rangle$ ratio as observed (black), with a linear fit removed (light gray), and with x_{BT} removed (dark gray). The theoretical ratio is shown as the red horizontal dashed line. Except at B4 and B5, removing x_{BT} best reproduces the theoretical ratio.

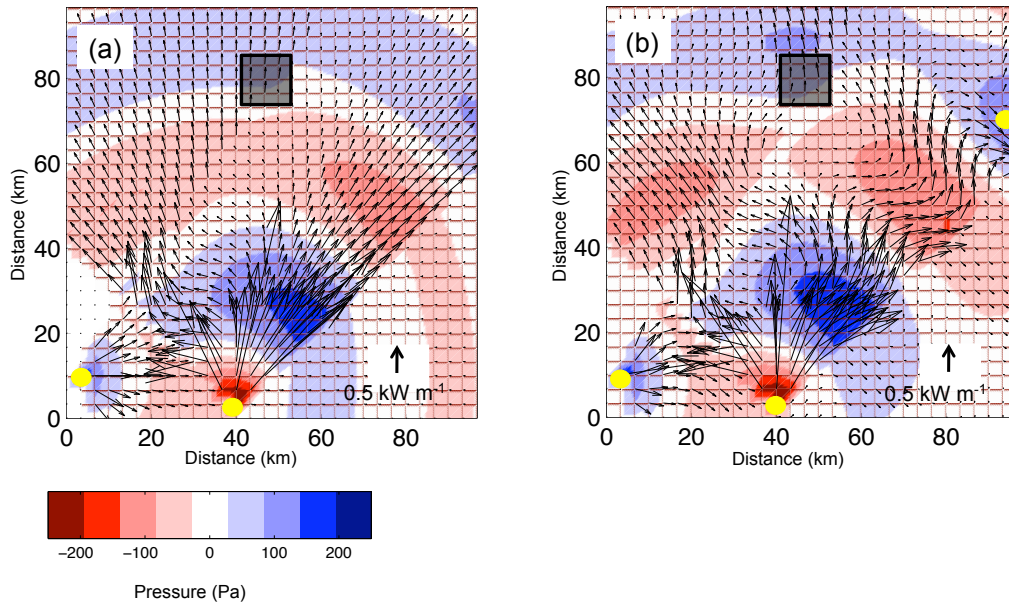


Figure 8. (a) Interference pattern created by two point sources 190° out of phase at Sur Platform (40 km, 0 km) and Sur Ridge (5 km, 10 km). A snapshot of the real part of the complex pressure field (colors), the depth-integrated mode-one energy flux (arrows), and the survey-box (rectangle) are shown. Azimuthal ranges of radiation are limited to simulate constraints of direction based on the shape and orientation of each feature. The amplitude of the sea surface height at Sur Platform is twice that at Sur Ridge to keep the forcing proportional to orthogonal barotropic velocities (relative to the feature). (b) The addition of a third source (100 km, 75 km, $\frac{1}{4}$ the amplitude at Sur Platform, and in phase with Sur Ridge) to supply offshore flux as observed further reduces lateral scales of variability in energy flux and results in more intricate flux patterns.

Chapter 4

Observations of the Internal Tide in Monterey Submarine Canyon

Abstract

Observations collected during August 2008 in Monterey Submarine Canyon reveal depth-integrated semidiurnal energy fluxes steered by canyon bathymetry. Fluxes are consistent with observations collected in August 1997 and a numerical model. Stations along the thalweg show depth-integrated fluxes decreasing from ~ 5 to ~ 3 kW m⁻¹ as the canyon axis shoals from 1500 to 900 m. Vertical profiles reveal predominantly along-canyon flux intensified in the bottom 500 m with beam-like features higher up in the water column. Nine cross-canyon sections and the model are used to create a rough one-dimensional along-canyon energy budget based on energy-flux divergence, dissipation rates and barotropic-to-baroclinic energy conversion rates. Good agreement between the model and observations allows for extrapolation of the observations and for synthesis of observation-based cross-canyon sections of depth-integrated flux used in the along-canyon budget. Cross-canyon structure of along-canyon flux is strongly correlated with the cross-canyon bathymetry. The peak in flux is within 1 km of the maximum depth of each section. Cross-canyon-integrated along-canyon flux decreases from 13 ± 3.4 MW at the deepest section (1500 m) to 5.6 ± 0.3 MW at the shallowest (900 m). The largest drop, ~ 7 MW, occurs as the flux navigates San Gregorio Meander and another drop of ~ 4 MW occurs as the flux navigates Monterey Meander. A one-dimensional flux budget is, on average, balanced; the mean of the residuals is smaller than the uncertainty estimates.

4.1 Introduction

Submarine canyons cover approximately 20% (*Hickey, 1995*) of continental shelves and play an important role in mixing, local tidal dynamics, and deep-sea - continental shelf exchange (*Carter and Gregg, 2002; Carter, 2010; Hall and Carter, 2011; McPhee-Shaw, 2006; Allen and Madron, 2009; Huussen, 2010*). These cross-shelf incisions act as a sink for internal tide energy and have been estimated to account for roughly 15% of the M_2 tidal dissipation (*Carter and Gregg, 2002; Kunze et al., 2012*) in the deep ocean (*Egbert and*

Ray, 2001). Globally, internal tidal dissipation is believed to contribute to thermohaline circulation (*Munk and Wunsch, 1998*). In order to maintain observed ocean stratification, the canonical value of average diapycnal diffusivity, K , based on an advection/diffusion balance with uniform upwelling over the entire abyssal basin is $K = 10^{-4} m^2 s^{-1}$ (*Munk, 1966*). However, weak interior diffusivity $O(10^{-5})$ has been found in the open ocean (*Ledwell et al., 1993; Kunze and Sanford, 1996; Polzin et al., 1997*). Mixing at isolated topographic features, such as submarine canyons, has been found to compensate for at least some of the weak interior diapycnal mixing (*Ledwell et al., 2000; Kunze et al., 2006; Simmons et al., 2004*). Identifying and quantifying sinks of internal tide energy will allow for improved predictive capabilities of numerical models which, though sensitive to where mixing occurs, cannot resolve the small scales associated with mixing and dissipation.

By focusing on the semidiurnal tide at one particular feature, Monterey Submarine Canyon, we can work towards understanding the role of canyon-specific processes. Ultimately, we would like to parametrize these processes for use in climate models though more of the physics must be understood before this is possible. Current turbulence parameterization schemes based on finescale shear and strain (*Polzin et al., 1995; Sun and E., 1999*) do not successfully estimate canyon dissipation rates (*Carter and Gregg, 2002; Kunze et al., 2002*). In addition to implications related to global dissipation, under-

standing the energy pathway of internal tides through submarine canyons has local consequences for forecasting of regional coastal tidal currents (*Petruncio et al.*, 2002), sediment transport processes (*Ribbe and Holloway*, 2001; *Puig et al.*, 2004; *Pomar et al.*, 2012) and biological processes (*Shea and Broenkow*, 1982; *Jan and Chen*, 2009).

Monterey Submarine Canyon, the largest submarine canyon on the west coast of the United States, has been the site of numerous observational and modeling studies, including the experiment discussed here. This canyon extends for over 100 km from the abyssal ocean to within 100 m of the California coast. With respect to the M_2 ray slope (Chapt. 2, page 18; $\alpha_{M_2} \approx 0.04$), the canyon walls are supercritical and the axis-slope near critical, creating an ideal situation for focusing and dissipation of the internal tide along the bottom (*Gordon and Marshall*, 1976; *Hotchkiss and Wunsch*, 1982).

The Monterey Bay region has a number of potential internal tide generation sites including Sur Platform, Sur Ridge, and Davidson Seamount. Though it is likely that all of these sources (as well as other remote topographic features) contribute to the internal tide in the canyon, the Sur Platform has been identified by numerical models as a dominant source (*Jachec et al.*, 2006; *Hall and Carter*, 2011; *Kang and Fringer*, 2011; *Johnston et al.*, 2011)[see Chapt. 3, Fig. 1]. Measurements north of Sur Platform confirm a northward flux (*Johnston et al.*, 2011; *Terker et al.*, 2012).

Observations from previous studies in Monterey Submarine Canyon are consistent with measurements in other submarine canyons, revealing large near-bottom internal tide velocities ($> 0.15 \text{ m s}^{-1}$) and energy fluxes following the canyon axis (*Shepard et al.*, 1974; *Petruncio et al.*, 1998; *Carter and Gregg*, 2002; *Kunze et al.*, 2002). Microstructure measurements have found temporally and spatially variable enhanced dissipation (and not predicted by finescale parameterizations) on the order of 10^{-3} W m^{-3} . These values correspond to diffusivities on the order of $K = 10^{-2} \text{ m}^2 \text{ s}^{-1}$ (*Lueck and Osborn*, 1985; *Carter and Gregg*, 2002; *Kunze et al.*, 2002, 2012). In addition to these consistent features, some differences among observations have been found and imply that tidal processes are time-variable in Monterey Submarine Canyon. For example, *Petruncio et al.* (1998) found evidence for a propagating wave during one experiment and a standing wave during another. They attribute this to changes in stratification. This importance of temporal variability and changes in stratification in terms of the baroclinic response has been corroborated by *Carter* (2010) and *Zhao et al.* (2012).

Tidally forced numerical models in the Monterey Bay region have generally been able to reproduce these findings (*Jachec et al.*, 2006; *Wang et al.*, 2009; *Carter*, 2010; *Hall and Carter*, 2011; *Kang and Fringer*, 2011) though the model domain must account for regionally remote sources to accurately predict the internal tides (*Hall and Carter*, 2011; *Terker et al.*, 2012). Simi-

lar results have been found in Gaoping Submarine Canyon located off southwestern Taiwan, a canyon similar in scale and shape to Monterey Submarine Canyon (*Lee et al.*, 2009; *Chiou et al.*, 2011). Furthermore, while the models are able to replicate the larger picture, some small-scale differences between models and observations have been found *Kunze et al.* (2012); *Terker et al.* (2012).

This chapter will present measurements of the internal tide in Monterey Submarine Canyon. Observations were collected at a number of stations along the thalweg as well as at some off-axis stations. These observations are compared with a modified Princeton Ocean Model run in the Monterey Bay region (*Hall and Carter*, 2011).

The goals of this chapter are to (i) test the model run in *Hall and Carter* (2011), (ii) describe the along- and cross-canyon fluxes and (iii) attempt to diagnose the one-dimensional along-canyon energy budget. The remainder of the paper is organized as follows: Section 4.2 presents the experiment design and analysis methods. Section 4.3 presents the results of this analysis focusing on profiles and depth-integrated energy flux along and across the canyon, model-observation comparisons, and creating an along-canyon budget with flux divergence, dissipation rates and barotropic-to-baroclinic convergence rates. Section 4.4 presents a summary of the results.

4.2 Data and methods

4.2.1 Data

Full-water-column profiles of baroclinic velocity, u', v' , and temperature, T , were collected in August, 2008 in Monterey Submarine Canyon from R/V *Point Sur* and R/V *John Martin* using eXpendable Current Profilers (XCPs) and a lowered ADCP (LADCP). As used in this paper, baroclinic, denoted by "' ", means that the depth-average has been removed while barotropic, denoted by and overbar "¯", implies a depth-averaged quantity. Forty-four XCP profiles were collected at eight stations (26, 27, 28, 32, 35, 36, 37, 38 in Fig. 1) over 12 hours between 14:30 20 August and 03:00 21, 2008 (UTC). Each station has at least four profiles spread as evenly as practicable over the semidiurnal tidal phase. There was a 20% XCP failure rate.

XCP's provide baroclinic velocity estimates by interpreting measurements of the electric field using the theory of motional induction (see Chapter 2.3, equations 8 and 9) with 2-m vertical resolution. Often, the upper 20-50 m is contaminated by the ship's electric and/or magnetic field causing loss of data; the first good values of u' and v' are extrapolated to the surface. Baroclinic pressure, P' , is not directly measured but arrived at by creating a density profile $\rho(z)$ from (i) $T(z)$, (ii) the temperature-salinity relationship and (iii) assuming a hydrostatic balance with $\bar{P}' = 0$. Profiles of baroclinic density,

$\rho'(z)$, are extrapolated by constraining the surface value to equal zero. Ten additional XCP stations collected during a previous experiment in the same location in August 1997, are also included [*Kunze et al.* (2002), noted as stations with a 'K' in Fig. 1].

Seventy LADCP profiles were collected at nine stations over two weeks. Each station was sampled for a complete 12-hour tidal cycle. A downward-looking RDI 300 kHz Workhorse Sentinel ADCP was attached to a rosette and lowered as close to the bottom as possible. This was difficult (for the VMP measurement as well as the LADCP) considering the proximity of the steep canyon walls and drifting of the ship during profiles which lasted for about an hour. Data were processed using software which separates ocean and instrument velocities, and translates data from a moving to a stationary frame of reference (*Thurnherr et al.*, 2008). This results in *rms* velocity errors of $<3 \text{ cm s}^{-1}$ (*Thurnherr*, 2010).

In addition to the XCP and LADCP data, dissipation rate estimates from microstructure measurements taken on the same cruise and presented in *Kunze et al.* (2012) are included in this analysis. Model output from a M_2 -forced modified Princeton Ocean Model with 250-m horizontal resolution run (*Hall and Carter*, 2011; *Carter*, 2010) is compared to observations and used as an interpolation/extrapolation tool to fill in spatial gaps as described below.

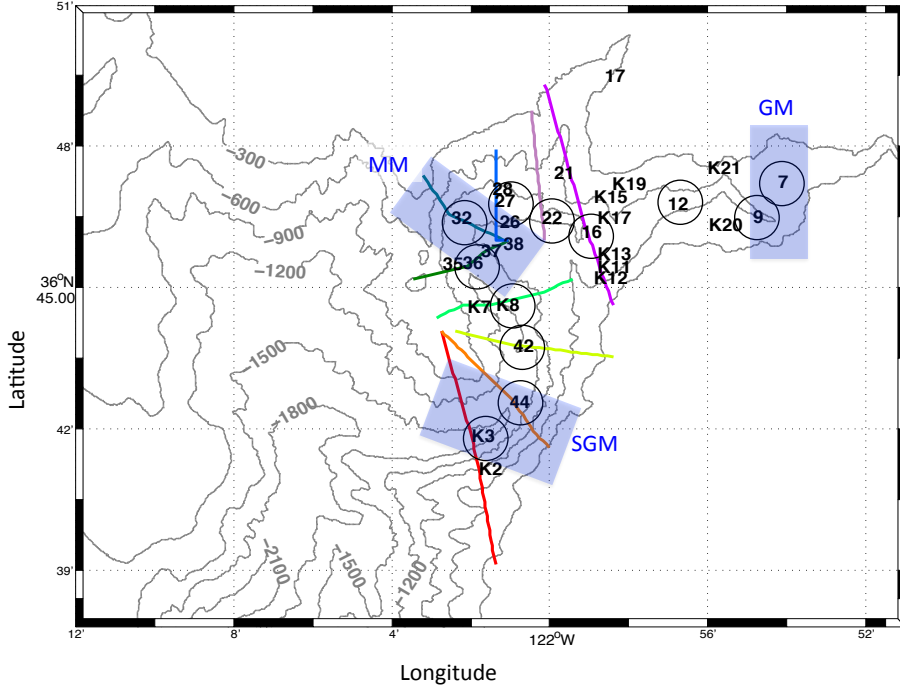


Figure 1: Station numbers (black) are centered on station locations. Stations from 1997 (*Kunze et al.*, 2002) have a 'K' in front of the number. Nine cross-sections (used in Fig. 6 and Fig. 8 later) are colored. Circled stations are used in the along-thalweg section. Bathymetry is contoured in gray at 300-m intervals. Sections are based on those in *Hall and Carter* (2011). San Gregorio Meander (SGM), Monterey Meander (MM) and Gooseneck Meander (GM) are highlighted in blue.

4.2.2 Methods: Energy-Flux Calculations and Budget

The along-canyon (AC), semidiurnal (SD) flux budget is a balance between energy-flux divergence ($\nabla F_{E,AC}^{SD}$), dissipation (D^{SD}) and barotropic-to-baroclinic conversion (C_{AC}^{SD}) as determined from

$$\frac{\partial}{\partial x} F_{E,AC}^{SD} = C_{AC}^{SD} - D^{SD} + R. \quad (1)$$

where R is the residual and includes errors for each of the terms as well as lateral escape or contributions from cross-canyon terms. Each of these terms will be explored below. Cross-canyon lateral escape across the 200-m isobath was examined in *Hall and Carter* (2011) and was found to account for less than 5% of the decrease in flux so is not included here.

Energy Flux: The semidiurnal tidal signal is extracted from u' , v' , and P' at each station by harmonic analysis (Chapt. 3, eq. 2) and used to calculate semidiurnal energy flux, \mathbf{F}_E^{SD} [Chapt. 3, eq. 1a, *Kunze et al.* (2002); *Nash et al.* (2005)]. Timeseries of u' , v' , P' and corresponding M_2 amplitudes and phases from station 26 are shown in Fig. 2. Energy-flux uncertainty is based on standard errors of the harmonic fits assuming residual variance characterizes noise and each profile is an independent sample. Ninety-five percent confidence intervals are constructed ($\mathbf{F}_{E,uncert}^{SD}$) at each station. Errors due to under-sampling (missing spatial variability or lower-frequency biasing) are not included.

Energy flux is rotated from east/west, north/south coordinates to along-canyon (positive along canyon is defined as up-canyon)/cross-canyon coordinates (90° counterclockwise from along-canyon). This rotation is illustrated in Fig. 3a for cross-canyon XCP-sections composed of stations 38, 26-28. Profiles of along- and cross-canyon energy fluxes are shown in Fig. 3b and

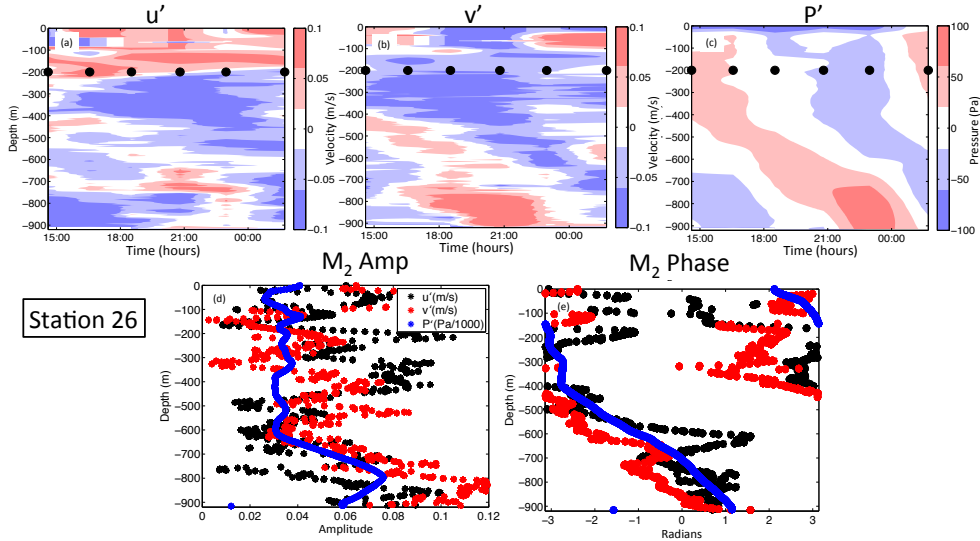


Figure 2: (a,b,c) Full-water column timeseries of u' , v' and P' , respectively, at Station 26. Black dots at 200 m depth indicate the times of profiles relative to 19 August 2008 20:13:00. M_2 amplitudes (d) and phases (e) for velocity and pressure based on the timeseries in a, b, and c as a function of depth.

c. As a consequence of sharp canyon curves, each station's along- and cross-canyon axes are oriented differently. To complement the cross-canyon views, an along-thalweg section is presented (Fig. 4) based on the circled stations in Fig. 1 and using profiles from 2008 XCPs and the LADCP, and 1997 XCPs.

In order to examine the canyon-averaged flux budget, it is necessary to interpolate and extrapolate measurements across the canyon. After extrapolation and interpolation, cross-sections of along-canyon flux based on observations are constructed resulting in along canyon (ac) flux as a function of cross-canyon distance $ccdist$, $F_{E,ac}^{SD}(ccdist)$. In addition to extrapolation and interpolation, we scale each of the model's (nine) cross-sections based on

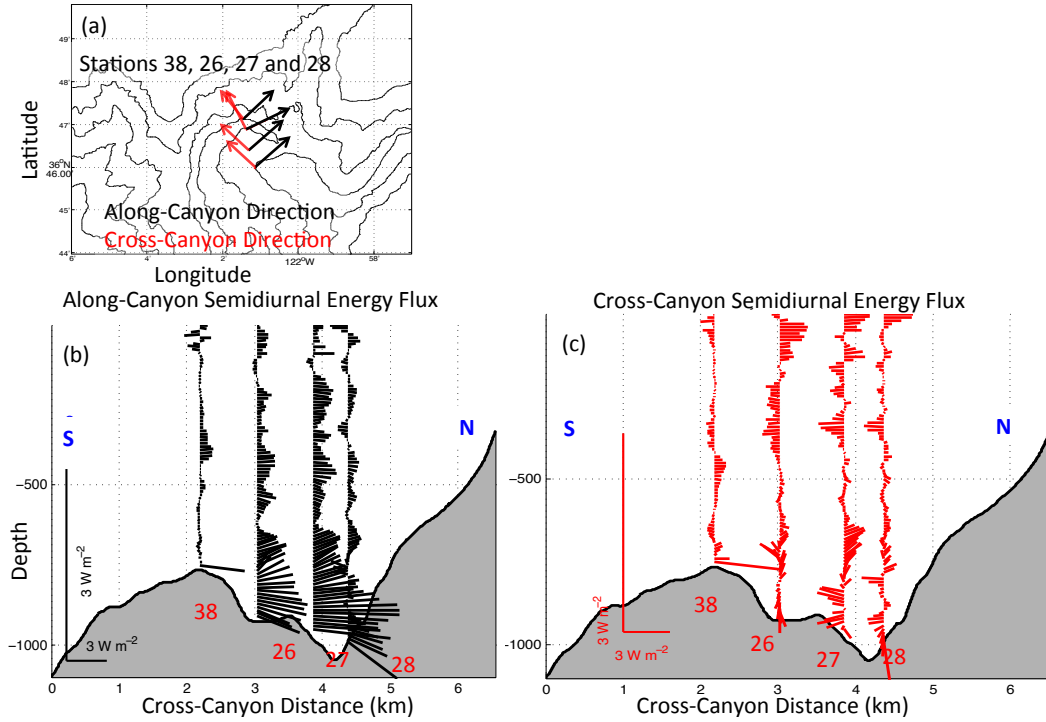


Figure 3: (a) Along- (black) and cross-canyon (red) axes are shown for a canyon cross-section consisting of XCP stations 38, 26, 27 and 28. (b) Along- and (c) cross-canyon profiles of horizontal and vertical semidiurnal energy flux for the stations (numbered in red) reveal bottom-intensified flux with beam-like features present throughout the water column. Angles of the along-canyon axis for stations 38, 26, 27 and 28 defined counter-clockwise from east are 33° , 46° , 31° , and 49° respectively. A scale for the energy flux is included in the bottom left of (c) in red.

a cosine-weighted average based on the magnitude of observed along-canyon fluxes. The cosine weighting is a function of cross-canyon distance, is centered on the canyon axis (cross-canyon distance = 0), and has a period of 2 km. A scatterplot of observed versus modeled fluxes (Fig. 5) shows that the scaling factor ranges from 1.8 (red, section one) to 0.4 (green, section five) with a mean scaling factor of 0.68. Since the scaling for section six was poorly con-

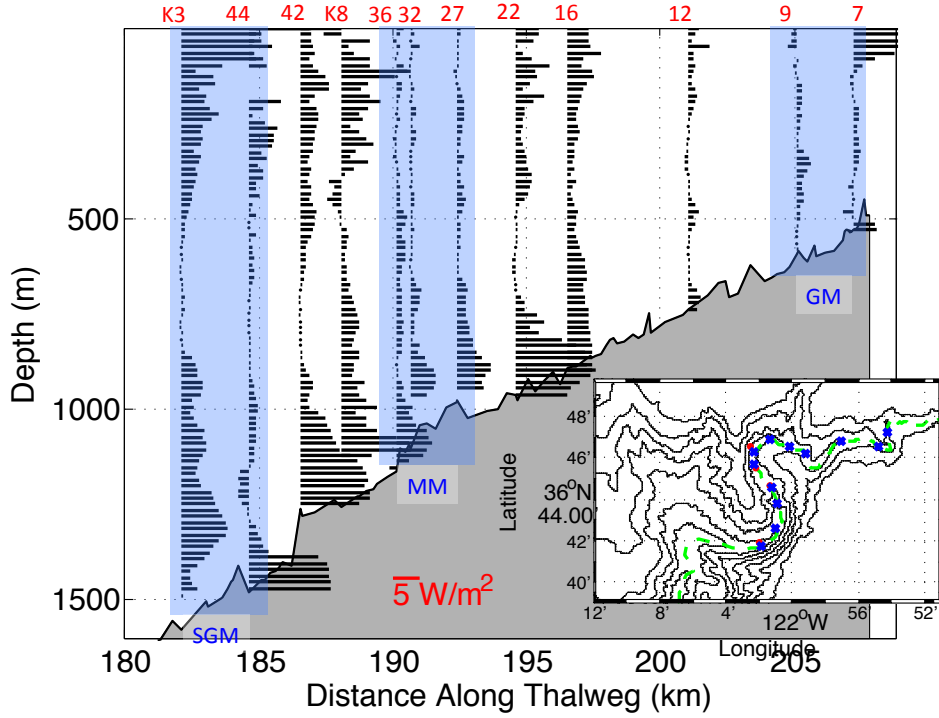


Figure 4: Profiles of semidiurnal along-canyon energy flux along the thalweg (circled stations in Fig.1). The along-canyon direction is chosen based on the direction of the depth-integrated energy-flux. Station numbers (red) are above the profiles and the inset provides an overhead view of the thalweg (green dashed) and the stations (blue 'x's'). A red 5 W/m^2 line is shown for scale above 190 km. Sections within San Gregorio Meander, Monterey Meander and Gooseneck Meander are highlighted in blue.

strained using only the two points off the canyon axis, this section was scaled using the mean scaling factor of sections five and seven. Section one was scaled using the smallest possible flux estimates because the smaller values were more consistent (though still larger) than all of the other fluxes. Using these cross-canyon structures (black hatched lines in Fig. 6) $F_{E,ac}^{SD}$ can be integrated across the canyon as $\left(F_{E,AC}^{SD} = \int_0^{cc_{length}} F_{E,ac}^{SD}(cc_{dist}) dcc_{dist} \right)$. Uncertainty for $F_{E,AC}^{SD}$ is based on differences in cross-canyon structure constructed

based on maximum and minimum flux magnitudes, $(F_{E,ac}^{SD} \pm F_{E,uncert}^{SD})$. No errors are included for differences in location of profiles comprising each station. XCP drops are, on average, about 50-m apart. Ship-drift during LADCP profiles causes larger spatial discrepancies in the profiles comprising each station.

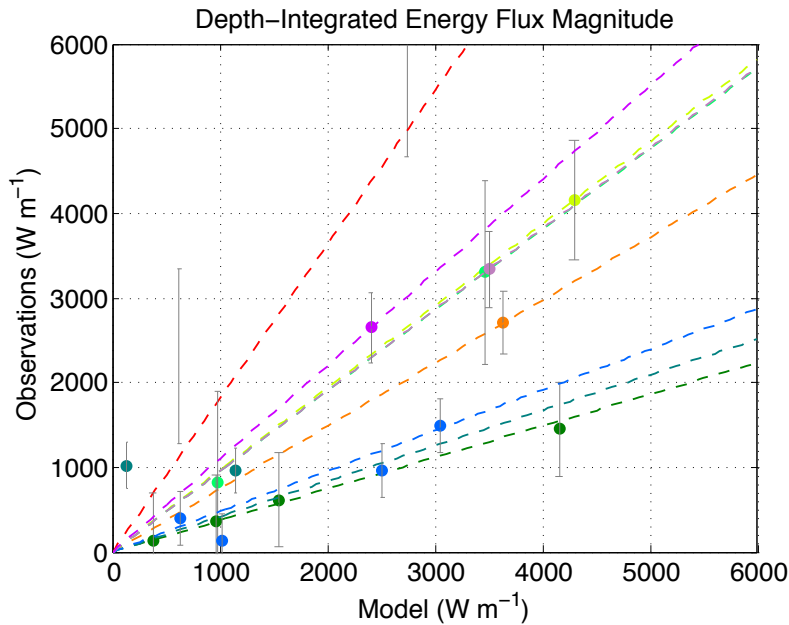


Figure 5: Scatterplot comparing semidiurnal depth-integrated energy-flux magnitude from the model (*Hall and Carter, 2011*) and observations (dots and 95 % confidence interval gray error bars) at observation locations. The scaling of the model (dashed lines) for each cross-section are used to adjust the models' cross-canyon structures to construct cross-canyon structures based on observations (shown in Fig. 6). Colors of dots and lines correspond to the colors of the sections in Fig.1.

Dissipation: Dissipation rate estimates (in $W kg^{-1}$), ϵ , are calculated as

$$\epsilon = 15 \nu u_z^2 / 2 \text{ where kinematic molecular viscosity } (\nu = 1.1 \times 10^{-6} m^2 s^{-1})$$

and u_z is measured microscale shear (*Kunze et al., 2012*). To convert ϵ into a quantity comparable to energy flux, ϵ is multiplied by ρ and integrated over the bottom 300-m (a triangular region bounded by the bottom and 300 meters above the thalweg depth) and along cross-canyon sections. Uncertainty in the dissipation estimates is a factor of 2.

Conversion: Barotropic-to-baroclinic conversion is a measure of the work done by the barotropic tide on the baroclinic tide. Conversion can be computed from observations based on the following information: bathymetry gradient, $(\nabla\mathbf{h})$, the amplitude and phase of the barotropic velocity $(\bar{\mathbf{u}}_o, \phi_{\bar{\mathbf{u}}_o})$ and the phase and amplitude of the baroclinic pressure at the bottom $(P'_o(z = -h), \phi_{P'_o}(z = -h))$ [*Zilberman et al., 2011; Kelly et al., 2012*] as follows

$$C^{SD} = -1 \langle (\nabla\mathbf{h} \cdot \bar{\mathbf{u}}) \times P'(z = -h) \rangle \quad (2)$$

$$= \frac{-1}{2} (\nabla\mathbf{h} \cdot \bar{\mathbf{u}}_o \times P'_o(z = -h)) (\cos(\phi_{\bar{\mathbf{u}}_o} - \phi_{P'_o}(z = -h))),$$

where $\langle \rangle$ equals a wave period average (12 h) alternatively noted as SD . Numerical models, such as the ones presented in *Carter et al. (2008); Carter (2010); Hall and Carter (2011); Kang and Fringer (2011)* solve barotropic and baroclinic energy equations at each time step. The conversion term is a sink in the barotropic energy equation and a source in the baroclinic one,

although it can be of either sign. Separate barotropic and baroclinic governing equations allow for conversion estimates and independent dissipation estimates, an improvement on models which equated conversion with baroclinic flux divergence such as those in *Merrifield and Holloway (2002)* and *Di Lorenzo et al. (2006)*. Conversion from both numerical models and observations is very sensitive to the resolution of the bathymetry. *Carter et al. (2008)* found that a 4-km grid produced approximately 20% less conversion than a 1-km grid around Hawaii. *Di Lorenzo et al. (2006)* found that inadequate bathymetric resolution at the Hawaiian Ridge led to conversion errors of 50%.

To calculate conversion based solely on observations, we need but don't have a measurement of the barotropic velocity. The shipboard ADCP was too noisy to make the relative XCP profiles absolute. To compensate for the lack of measurements, a hybrid model-observation conversion was synthesized using barotropic velocity from the model and bottom baroclinic pressure from observations. For simplicity, and because off-axis velocity and flux measurements are weak and therefore steep cross-canyon bathymetry would mainly cancel out on each side of the canyon, only the along-canyon component of velocity and bathymetric slope are used. A dx of 1 km and finite-differencing is used to get the along-canyon bathymetric slope. Conversion rates from (2) are multiplied by a cross-canyon distance to compare

to $F_{E,AC}^{SD}$ and cross-canyon integrated ϵ . Uncertainty estimates for conversion are based on the goodness of fit of P' at the bottom since the barotropic velocity is from the model and the along-canyon bathymetry gradient is fairly smooth.

4.3 Results

4.3.1 Model-Observation Comparison

Depth-integrated energy-flux vectors are comparable between the observations and model, and are strongly influenced by canyon bathymetry (Fig. 7 and Fig. 6). A beam of maximum flux, no wider than a few kilometers and slightly narrower than the bathymetry, closely follows the deepest path of the canyon until Gooseneck Meander where the beam shifts to the right of the thalweg. Barotropic velocity is also steered by the canyon (*Hall and Carter, 2011; Carter, 2010*).

One model-observation discrepancy is the smaller observed fluxes around Monterey Meander (sections five and seven in Fig. 6) *Kunze et al. (2002); Hall and Carter (2011)*. *Kunze et al. (2002)* also found a decrease around this bend (those fluxes are not included in this analysis). *Hall and Carter (2011)* attributed this observed decrease to under-sampling as *Kunze et al. (2002)* had only a single measurement (not included as one of the stations

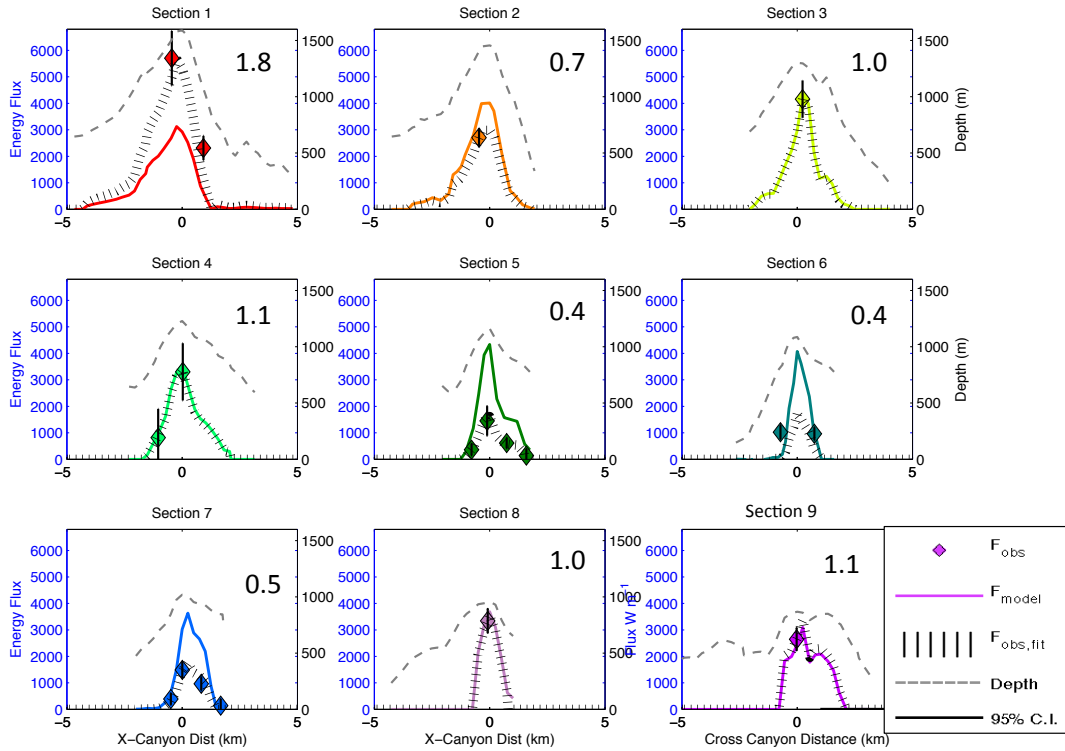


Figure 6: (left y-axis, all panels) Depth integrated semidiurnal energy flux from Hall and Carter (2011) [solid colored lines], observations (colored diamonds), and the extrapolated cross-canyon structure corresponding to observations (black hatched lines) [legend in bottom right]. Each subplot corresponds to the a (color-coded) cross-section in Fig. 1 and the scaling factor used to create the observation-based cross-section is included in the right-upper corner of each section plot. (right y-axis, all panels) Bathymetry of the cross-sections are plotted and correspond to right y-axis (gray dashed lines). The deepest point on the cross section is used at the reference point for cross-canyon distance.

in Fig. 1) at the apex of Monterey Meander. However, data collected with more complete cross-canyon coverage in 2008 (stations 26-28 in Fig. 1) also finds a decrease in energy flux. Furthermore, when the model's along canyon energy flux is computed in the same way as is done for observations (i.e.

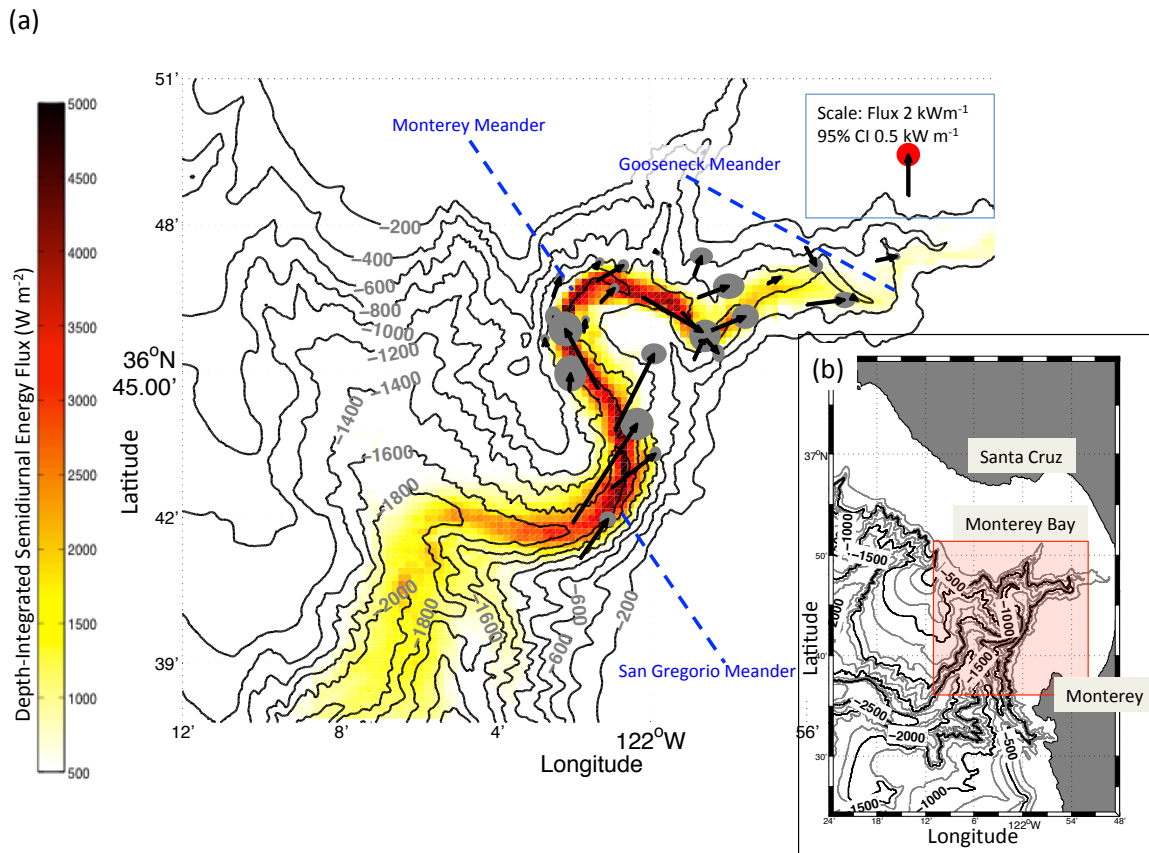


Figure 7: (a) Semidiurnal depth-integrated energy flux vectors (black arrows) and 95% level confidence intervals (gray ellipses, red ellipse on scale arrow) from observations in 1997 and 2008 and energy flux magnitude from a model run by *Hall and Carter* (2011) [colors] in Monterey Submarine Canyon. Bathymetry is contoured in 200-m intervals. The meanders highlighted in blue in Fig.1 are noted here. (b) An overview of the California Coast (gray) and Monterey Bay region with Santa Cruz, Monterey, and Monterey Bay shown for reference. The red box highlights the region shown in (a). Bathymetry is contoured at 500-m intervals (black lines) and 200-m intervals (gray lines).

using discrete cross-canyon sections rather than integrating over regions), the model also shows a small but robust decrease inside the meander. Another (less explainable) difference is that deepest station K3 (section one) has an

observed flux almost double the model prediction.

Despite magnitude differences, the cross-canyon structures are similar between the model and observations, based on sections that have more than one observation spanning the cross-section. For example, sections 5 and 7 exhibit a steep increase to the left of the maximum flux and a more gradual decrease in flux right of the peak. This similarity in structure justifies scaling the model to create observation-based cross-canyon structures (black hatched lines in Fig. 6). Cross-canyon profiles, which also exhibit a strong correlation with bathymetry (Fig. 6) are integrated to create an along-canyon energy budget (Section 4.3.3).

4.3.2 Energy Flux Profiles

Energy-flux profiles in Figs. 3 and 4 reveal almost exclusively up-canyon propagation and bottom-intensification 100-500 meters above the bottom. This intensification is predominantly seen in the along-canyon sections and is limited to within a few kilometers of the canyon axis. Above the bottom-intensification, there is evidence for beams at about 250 and 500-m depths (Fig. 3b). Beams, as opposed to a standing wave, are consistent with Fig. 2e where the P' , u' and v' phases all increase with depth (*Martini et al.*, 2007; *Petruncio et al.*, 1998). The cross-canyon fluxes [Fig. 3(c)] also exhibit beam-like features at a number of depths.

4.3.3 Energy Budget

A one-dimensional along-canyon energy budget is a balance between flux divergence, dissipation and barotropic-to-baroclinic conversion. The along-canyon flux [created by integrated the cross canyon sections in Fig. 6] reveals a net decrease in flux of 7 MW as the canyon shoals [Fig. 8(a), solid]. Sharp decreases around San Gregorio Meander (~ 7 MW) and Monterey Meander (~ 4 MW) account for the majority of the diminishing flux. The model has a smaller net decrease in flux of ~ 2 MW and exhibits no decrease (rather a small increase) around San Gregorio Meander [Fig. 8(a), dashed]. Apart from the large difference (~ 6 MW) at the deepest cross-section, the model and observations have an *rms* difference of 1.4 MW. Flux divergence [Fig. 8(b)] is the derivative of along canyon flux, and so (for observations) has large negative values around both meanders (the model only has a divergence around Monterey Meander). In order to have a closed budget, this flux divergence must be balanced by barotropic-to-baroclinic conversion and dissipation.

Barotropic-to-baroclinic conversion rates (Fig. 8c) show both positive and negative values implying both barotropic-to-baroclinic and baroclinic-to-barotropic energy exchange. Since the observed conversion is truly a model-observation hybrid quantity, dissimilarities must be caused by differences between modeled and observed baroclinic bottom pressure. Dissipation

rates from observations (Fig. 8d, solid) are greatest at the deepest sections and suggest stronger decay at along-thalweg distances of 186 km and steady but weaker decay from 192-197 km. Not all stations have microstructure measurements, so this term in the budget is undersampled relative to the other terms. Dissipation rate estimates only account for the 300 m above the deepest point and do not include any dissipation from the canyon sidewalls or the canyon rim *Wain et al. (2012)*, though it is unclear whether this is important or not. Model dissipation is the residual of flux divergence and conversion. The mean of the observed dissipation is 0.2 kW m^{-1} and the mean of model dissipation is 0.6 kW m^{-1} .

The observation-based budget [Fig. 8(e)] combines all the terms discussed above as well as a residual term which absorbs unaccounted errors in flux divergence, dissipation, and conversion (as well as any lateral escape). The average residual is 0.2 kW m^{-1} (assuming uniform spacing between observations), which is smaller but of the same magnitude as the uncertainty in the budget (0.6 kW m^{-1}). Uncertainty in the budget is the square root of the sums of the squares error terms for each term in the budget and assumes that these terms are independent with random errors. The largest residual (at along-thalweg distance 183 km) is a result of unbalanced negative flux divergence between the deepest two cross-sections. It is entirely possible that we are underestimating dissipation here; there are no microstructure mea-

measurements at the deepest two stations. The model budget looks similar to the observation budget [Fig. 8(f)] except for the deepest station. Both budgets show large negative flux divergences around Monterey Meander and this accounts for positive flux divergence and positive conversion at the shallower cross-sections (or a spike in dissipation in the model).

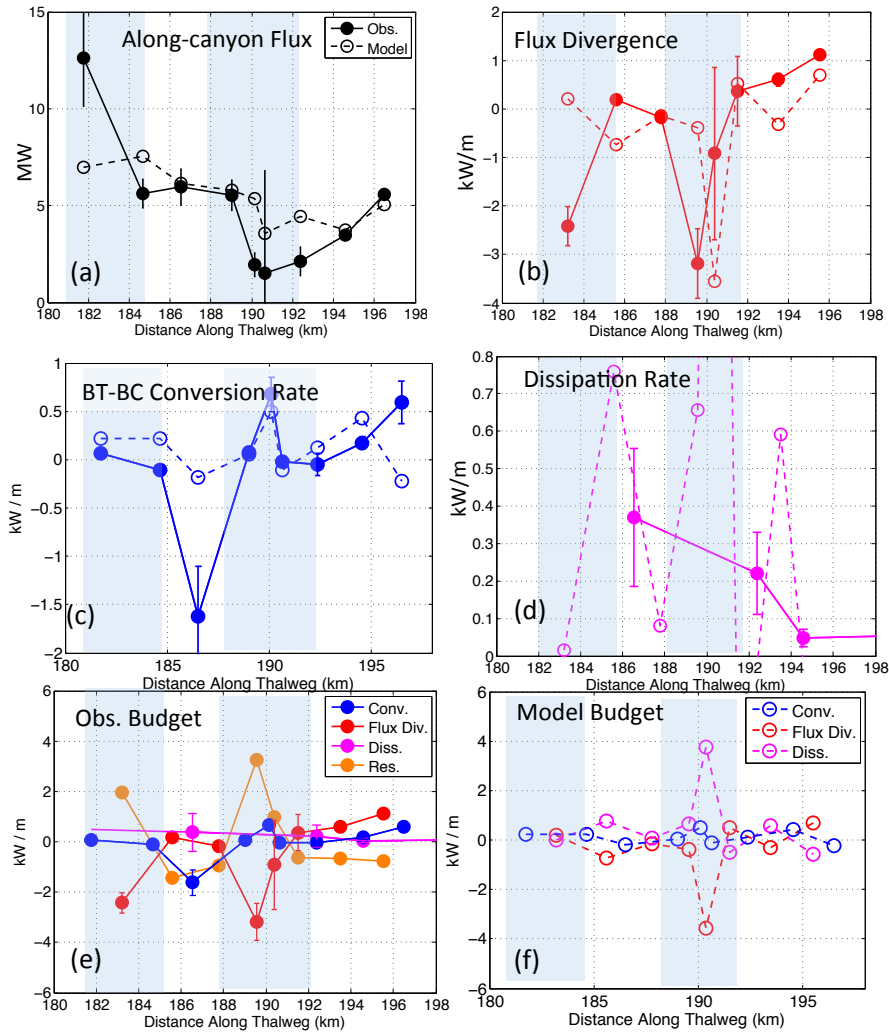


Figure 8: Flux budget: (a) Along-thalweg semidiurnal energy-flux based on cross-canyon integrals of along-canyon energy flux from observations [solid] and the model [open / dashed], (b) flux divergence, (c) convergence rates, (d) dissipation rates (*Kunze et al.*, 2012), (e) flux budget based on observations, and (f) flux budget based on the model. Sections within San Gregorio Meander and Monterey Meander are highlighted in blue.

4.4 Summary

Observations collected in Monterey Submarine Canyon reveal depth-integrated fluxes strongly steered by the canyon and decreasing as the canyon shoals.

The model run by *Hall and Carter* (2011) is able to reproduce the dominant features and patterns of the internal tide in Monterey Submarine Canyon. Observed fluxes decrease more than model fluxes around meanders but also increase more than model fluxes after the meanders. The decreases around the meanders are the largest decreases in flux. Cross-canyon sections in both the model and observations reveal that maximum fluxes are tightly coupled to the canyon axis (Fig. 6). Profiles of along-canyon energy flux show bottom intensification in the bottom 100-500 meters and smaller but substantial fluxes mid-water column (Fig. 3). Cross-canyon fluxes are small, but show evidence for mid-water column beams. Barotropic-to-baroclinic conversion is computed by combining model and observational data. Both positive and negative conversion is found along the canyon axis. The rough energy budget shows that, on average, dissipation and conversion balance energy-flux divergence, though point-to-point measurements do not balance. More observations would allow for better constraint on cross-canyon structures for both flux and dissipation, and would provide better along-canyon resolution both of which would allow for a more refined budget estimate.

4.5 Acknowledgments

The 2008 experiment was designed to examine the role of canyons in boundary mixing and exchange with the ocean interior was funded by the National Science Foundation and the PIs are James B. Girton, Erika McPhee-Shaw and Eric Kunze.

References

- Allen, S., and X. Madron (2009), A review of the role of submarine canyons in deep-ocean exchange with the shelf, *Ocean Sci.*, pp. 607–20.
- Carter, G. (2010), Barotropic and baroclinic M_2 tides in the Monterey Bay region, *J. Phys. Oceanogr.*, pp. 1766–83.
- Carter, G., and M. Gregg (2002), Intense, variable mixing near the head of Monterey Submarine Canyon, *J. Phys. Oceanogr.*, pp. 3145–65.
- Carter, G., M. Merrifield, J. Becker, K. Katsumata, M. Gregg, D. Luther, M. Levine, T. Boyd, and Y. Firing (2008), Energetics of M_2 barotropic-to-baroclinic tidal conversion at the Hawaiian Islands, *J. Phys. Oceanogr.*, pp. 2205–23.
- Chiou, M.-D., S. Jan, J. Wang, L. R.-C., and H. Chien (2011), Sources of baroclinic tidal energy in the Gaoping Submarine Canyon off southwestern Taiwan, *J. Geophys. Res.*, p. (116) C12016.
- Di Lorenzo, E., W. Young, and S. Llewellyn Smith (2006), Numerical and analytical estimates of M_2 tidal conversion at steep oceanic ridges, *J. Phys. Oceanogr.*, pp. 1072–84.
- Egbert, G., and R. Ray (2001), Estimates of M_2 tidal energy dissipation from TOPEX/Poseidon altimeter data, *J. Geophys. Res.*, pp. 22,475–502.
- Gordon, R., and N. Marshall (1976), Submarine canyons: Internal wave traps?, *Geophys. Res. Lett.*, pp. 622–24.
- Hall, R., and G. Carter (2011), Internal tides in Monterey Submarine Canyon, *J. Phys. Oceanogr.*, pp. 186–204.
- Hickey, B. (1995), Coastal submarine canyons, in *Proceedings of the University of Hawaii 'Aha Huliko'a Workshop on Flow Topography*, pp. 95–110.
- Hotchkiss, F., and C. Wunsch (1982), Internal waves in Hudson Canyon with possible geological implications, *Deep-Sea Res.*, pp. 414–42.
- Huussen, E. (2010), Is the Indian Ocean MOC driven by internal wave breaking?, Ph.D. thesis, University of Southampton, Southampton, UK.

- Jachec, S., O. Fringer, M. Gerritsen, and R. Street (2006), Numerical simulation of internal tides and the resulting energetics within Monterey Bay and the surrounding area, *Geophys. Res. Lett.*, p. (33) L12605.
- Jan, S., and C.-T. Chen (2009), Potential biogeochemical effects from vigorous internal tides generated in Luzon Strait: a case study at the southernmost coast of Taiwan, *J. Geophys. Res.*, p. C04021.
- Johnston, T., D. Rudnick, G. Carter, R. Todd, and S. Cole (2011), Internal tide beams and mixing near Monterey Bay, *J. Geophys. Res.*, p. C03017.
- Kang, D., and O. Fringer (2011), Energetics of barotropic and baroclinic tides in the Monterey Bay area, *J. Phys. Oceanogr.*, p. in press.
- Kelly, S., J. Nash, K. Martini, M. Alford, and E. Kunze (2012), The cascade of tidal energy from low to high modes on a continental slope, *J. Phys. Oceanogr.*, p. submitted.
- Kunze, E., and T. Sanford (1996), Abyssal mixing: Where it isn't, *J. Phys. Oceanogr.*, pp. 2286–96.
- Kunze, E., L. Rosenfeld, G. Carter, and M. Gregg (2002), Internal waves in Monterey Submarine Canyon, *J. Phys. Oceanogr.*, pp. 1890–1913.
- Kunze, E., E. Firing, J. Hummon, and T. Chereskin (2006), Global abyssal mixing inferred from lowered ADCP shear and CTD strain profiles, *J. Phys. Oceanogr.*, pp. 1553–76.
- Kunze, E., C. MacKay, E. McPhee-Shaw, K. Morrice, J. Girton, and S. Terker (2012), Turbulent Mixing and Exchange With Interior Waters on Sloping Boundaries, *J. Phys. Oceanogr.*, p. in press.
- Ledwell, J., A. Watson, and C. Law (1993), Evidence for slow mixing across the pycnocline from an open-ocean tracer-release experiment, *Nature*, pp. 701–703.
- Ledwell, J., J. Montgomery, K. Polzin, L. St. Laurent, R. Schmitt, and J. Toole (2000), Evidence for enhanced mixing over rough topography in the abyssal ocean, *Nature*, pp. 179–82.
- Lee, I., Y. Wang, J. Liu, W. Chuang, and J. Xu (2009), Internal tidal currents in the Gaoping (Kaoping) submarine canyon, *J. Marine Systems*, pp. 397–404.

- Lueck, R., and T. Osborn (1985), Turbulence measurements in a submarine canyon, *Continental Shelf Res.*, pp. 681–98.
- Martini, K., M. Alford, J. Nash, and E. Kunze (2007), Diagnosing a partly standing internal wave in Mamala Bay, Oahu, *Geophys. Res. Lett.*, p. L17604.
- McPhee-Shaw, E. (2006), Boundary-interior exchange: Reviewing the idea that internal-wave mixing enhances lateral dispersal near continental margins, *Deep-Sea Res. II*, pp. 42–59.
- Merrifield, M., and P. Holloway (2002), Model estimates of M_2 internal tide energetics at the Hawaiian Ridge, *J. Geophys. Res.*, p. (107) 3179.
- Munk, W. (1966), Abyssal recipes, *Deep-Sea Res.*, pp. 707–30.
- Munk, W., and C. Wunsch (1998), Abyssal recipes II: energetics of tidal and wind mixing, *Deep-Sea Res. I*, pp. 1977–2010.
- Nash, J., M. Alford, and E. Kunze (2005), Estimating internal wave energy fluxes in the ocean, *J. Atmos. Oceanic Technol.*, pp. 1551–70.
- Petruncio, E., L. Rosenfeld, and J. Paduan (1998), Observations of the internal tide in Monterey Canyon, *J. Phys. Oceanogr.*, pp. 1873–1903.
- Petruncio, E., J. Paduan, and L. Rosenfeld (2002), Numerical simulations of the internal tide in a submarine canyon, *Ocean Modelling*, pp. 221–48.
- Polzin, K., J. Toole, and R. Schmitt (1995), Finescale parameterizations of turbulent dissipation, *J. Phys. Oceanogr.*, pp. 306–28.
- Polzin, K., J. Toole, J. Ledwell, and R. Schmitt (1997), Spatial variability of turbulent mixing in the abyssal ocean, *Science*, pp. 93–6.
- Pomar, L., M. Morsilli, P. Hallock, and B. Badenas (2012), Internal waves, an under-explored source of turbulence events in the sedimentary record, *Earth-Science Rev.*, pp. 56–81.
- Puig, P., A. Palanques, J. Gullen, and M. El Khatab (2004), Role of internal waves in the generation of nepheloid layers on the northwestern Alboran slope: Implications for continental margin shaping, *J. Geophys. Res.*, p. (109) C09011.
- Ribbe, J., and P. Holloway (2001), A model of suspended sediment transport by internal tides, *Cont. Shelf Res.*, pp. 395–422.

- Shea, R. ., and W. Broenkow (1982), The role of internal tides in the nutrient enrichment of Monterey Bay, California, *Cont. Shelf Res.*, pp. 395–422.
- Shepard, F., N. Marshall, and P. McLoughlin (1974), "Internal waves" advancing along submarine canyons, *Science*, pp. 195–98.
- Simmons, H., R. Hallberg, and B. Arbic (2004), Internal wave generation in a global baroclinic tide model, *Deep-Sea Res. II*, pp. 3043–3068.
- Sun, H., and K. E. (1999), Internal wave-wave interaction. Part II: spectral energy transfer and turbulence production, *J. Phys. Oceanogr.*, pp. 2905–19.
- Terker, S., J. Girton, E. Kunze, J. Klymak, and R. Pinkel (2012), Observations of the internal tide on the California Continental Margin near Monterey Bay, *Submitted to Cont. Shelf Res.*
- Thurnherr, A. (2010), A practical assessment of the errors associated with full-depth LADCP profiles obtained using Teledyne RDI Workhorse acoustic Doppler current profilers, *J. Atmos. Oceanic Technol.*, pp. 1215–27.
- Thurnherr, A., M. Visbeck, E. Firing, B. King, G. Hummon, G. Krahman, and B. Huber (2008), *A manual for acquiring lowered Doppler current profiler data.*
- Wain, D., M. Gregg, M. Alford, R.-C. Lien, G. Carter, and R. Hall (2012), Propagation and dissipation of the internal tide in upper Monterey Canyon, *J. Geophys. Res.*, pp. submitted–.
- Wang, X., Y. Chio, C. Dong, J. Farrara, L. Zhijin, J. McWilliams, J. Paduan, and L. Rosenfeld (2009), Modeling tides in Monterey Bay, California, *Deep-Sea Res. II*, pp. 219–31.
- Zhao, Z., M. Alford, R.-C. Lien, M. Gregg, and G. Carter (2012), Internal tides and mixing in a submarine canyon with time-varying stratification, *J. Phys. Oceanogr.*, p. submitted.
- Zilberman, N., M. Merrifield, G. Carter, and D. Luther (2011), Incoherent nature of M_2 tides at the Hawaiian Ridge, *J. Phys. Oceanogr.*, pp. 2021–36.

Curriculum Vitae

Samantha (Brody) Terker

Education

- June 2007–March 2012 **Ph.D.**, *University of Washington*, Seattle, WA.
School of Oceanography.
Thesis: Observations and Analysis of the Internal Tide in the Monterey Bay Region.
- Sept. 2005– June 2007 **M.S.**, *University of Washington*, Seattle, WA. School of Oceanography.
Masters Project: The Refurbishment and Sea-trials of the EM-POGO. Upgraded, tested and evaluated a velocity profiler.
- Sept. 2001–June 2005 **B.S.**, *Swarthmore College*, Swarthmore, PA.
Engineering major, focus on electrical engineering, English literature minor. Four years of varsity soccer and softball.
Senior Design Project: Design and Construction of an Underwater Remotely Operated Vehicle.

Work Experience

- June 2005-present **Research Assistant**, *Applied Physics Lab, University of Washington*, Seattle, WA.
- Collected data on numerous research cruises using a variety of instruments.
 - Analyzed the data using MATLAB and timeseries analysis techniques including harmonic analysis, spectral analysis, complex analysis, regression and statistical methods.
 - Presented at conferences and seminars and published the results of the analysis.
- June 2007 **Scientist**, *Evans-Hamilton, Inc.*, Seattle, WA.
- Collected data off the Gulf Coast and compiled daily reports about eddies and ocean currents.
- Jan., June-Aug. 2004 **Guest Student**, *Woods Hole Oceanographic Institution*, Woods Hole, MA.
- Assisted with a variety of ocean engineering projects relating to ocean instrumentation.
- June–Aug. 2001-2003 **Dive Instructor**, *Broadreach, Inc.*, Caribbean.
- PADI dive instructor and wilderness first responder (2003) support staff (2002) and intern (2001) aboard sailing vessels.
 - Certified and supervised students, coordinated lesson plans.

Skills, Interests and Activities

- Extensive experience with Matlab, Windows, Linux, Latex and Microsoft office.
- Member of the organizing committee for a student conference (2011), the International Meeting for Students in Physical Oceanography (IMSPO).
- American Geophysical Union member (2006 - present).
- Teaching experience: Teachers assistant at the University of Washington, took a Centers for Ocean Sciences Education Excellence (COSEE) course which included teaching at an elementary school in Seattle, and taught scuba diving.
- Hobbies: trail running, yoga, reading, snowboarding, and mountain and road biking.

Please see the following pages for a list of papers, presentations and conference abstracts, references and research cruises.

Papers

Terker, S., Girton, J.B., Kunze, E., Klymak, J. and Pinkel, R. (2012). Observations of the internal tide on the California continental margin near Monterey Bay. Submitted to Continental Shelf Research.

Terker, S., Sanford, T.B., Dunlap, J.H., Girton, J.B. (2012). The EM-POGO: A Simple, Absolute Velocity Profiler. Submitted to Deep-Sea Research II.

Kunze E., MacKay, C., McPhee-Shaw, E., Morrice, K., Girton, J., **Terker, S.** (2012). On Turbulent Mixing and Exchange with Interior Waters on Sloping Boundaries. Submitted to Journal of Physical Oceanography.

Williams 3rd, A.J, Morrison III, A.T., **Brody, S.R.** (2005). Vertical cosine response of a faired ring acoustic current meter. Proceedings of the the IEEE/OES Eighth Working Conference on Current Measurement Technology,19-25.

Presentations and Conference Abstracts

- 2010 Center for Coastal Margin Observation & Prediction Workshop in Beaverton, OR. Presentation. **Terker, S.**, Sanford, T., Dunlap, J. Carlson, J., Lauffenburger, N. Remotely sensed salinity profiles from the sigma profiler.
- 2010 Ocean Sciences Conference in Portland, OR. Presentation. **Brody, S.**, Girton, J.B., Kunze, E. McPhee-Shaw, E. The internal tide and energy fluxes within and entering Monterey May Submarine Canyon.
- 2010 Ocean Sciences Conference in Portland, OR. Abstract. McPhee-Shaw, E. Kunze E., Morrice, K., Girton, J., **Brody, S.** Insights into Canyon Mixing and Interior-Boundary Exchange.
- 2010 Ocean Sciences Conference in Portland, OR. Abstract. Morrice, K.J., McPhee-Shaw, E.E., Girton, J.B., Kunze, E., **Brody, S.R.** Dynamics of Bottom Boundary Layer Thickness in Monterey Bay Canyon.
- 2009 International Association for the Physical Sciences of the Oceans Conference in Montreal, QC. Presentation. Kunze, E., Bartlett, K., MacKay, C., McPhee-Shaw, E., Morrice, K., **Brody, S.**, Girton, J. Turbulence along a Submarine Canyon Axis.
- 2008 Moss Landing Marine Laboratories, Moss Landing, CA. Presentation. **Brody, S.**, Girton, J.B., Kunze, E. The EM-POGO sea-trials and energy fluxes from a 2006 AESOP cruise.
- 2008 Ocean Sciences Conference in Orlando, FL. Abstract. **Brody, S.R.**, Girton, J.B., Kunze, E. Observations of the internal tide entering Monterey Canyon.
- 2007 Physical Oceanography Seminar at the University of Washington, Seattle, WA. Masters Presentation. The Reconditioning and Sea-Trials of the EM-POGO.

References

Dr. James Girton
206.543.8467
girton@apl.washington.edu
Applied Physics Laboratory
University of Washington
1013 NE 40th Street
Box 355640
Seattle, WA 98105-6698

Dr. Thomas Sanford
206.543.1365
sanford@apl.washington.edu
Applied Physics Laboratory
University of Washington
1013 NE 40th Street
Box 355640
Seattle, WA 98105-6698

Dr. Eric Kunze
206-221-2616
kunze@apl.washington.ed
Applied Physics Laboratory
University of Washington
1013 NE 40th Street
Box 355640
Seattle, WA 98105-6698

Research Cruises

- 2007 - 2011 R/V *Forerunner*, Multiple day cruises in the Columbia River. These cruises were part of the Center for Coastal Margin Observation & Prediction project and involved testing a new instrument, the sigma profiler, which measures conductivity of the water column. P.I. Thomas Sanford
- 2008 R/V *Pt. Sur*, 15 days in the Monterey Bay region. The cruise was designed to investigate the role of canyons in boundary mixing and exchange with the ocean interior. P.I.s James Girton, Eric Kunze and Erika McPhee-Shaw
- 2007 14 days, Gulf of Mexico. Monitored currents and eddies around operating oil rigs to ensure conditions were safe for drilling. Contracted for Evans Hamilton, Inc.
- 2006 R/V *Pt. Sur*, 14 days in the Monterey Bay region. The cruise was part of the Monterey Bay 2006 suite of experiments and was designed to assess the effectiveness of submesoscale ocean parameterizations. A high spatial resolution survey of the internal tide west of Pt. Sur was conducted and the EM-POGO sea-trials took place. P.I.s Thomas Sanford, James Girton and Eric Kunze
- 2004 R/V *Oceanus*, 11 days offshore of Casco and Penobscot Bays. The cruise was designed to conduct synoptic mapping of *A. fundyense*, hydrography, and velocity in the coastal current. P.I. Dennis Mcgillicuddy